

PREDICTION AND OPTIMAL EXPERIMENTAL  
DESIGN IN SYSTEMS BIOLOGY MODELS

A Dissertation

Presented to the Faculty of the Graduate School

of Cornell University

in Partial Fulfillment of the Requirements for the Degree of

Doctor of Philosophy

by

Fergal P. Casey

January 2007

© 2007 Fergal P. Casey

ALL RIGHTS RESERVED

PREDICTION AND OPTIMAL EXPERIMENTAL DESIGN IN SYSTEMS  
BIOLOGY MODELS

Fergal P. Casey, Ph.D.

Cornell University 2007

In this dissertation we propose some approaches in model-building and model analysis techniques that can be used for typical systems biology models.

In Chapter 2 we introduce a dynamical model for growth factor receptor signaling and down-regulation. We show how, by quantitatively fitting the model to experimental data, we can infer interactions that are needed to describe the dynamical behavior. We demonstrate that predictions need to be accompanied by uncertainty estimates for both model validation and hypothesis testing. We then introduce some of the techniques from the optimal experimental design literature to reduce the prediction uncertainty for dynamical variables of interest.

In Chapter 3 we analyze the convergence properties of some of the Markov Chain Monte Carlo (MCMC) algorithms that can be used to give more rigorous uncertainty estimates for both parameters and dynamical variables within a model. We lay out a straightforward procedure which gives approximate convergence rates as a function of the tunable parameters of the MCMC method. We show that the method gives good estimates of convergence rates for the one dimensional probability distributions we examine, and it suggests optimal choices for the tunable parameters. We discover that variants of the basic MCMC algorithms which claim to have accelerated convergence often completely fail to converge geometrically in

the tails of the probability distribution.

In Chapter 4 we consider a different problem — how to efficiently simulate stochastic dynamics within a biochemical network. We introduce a mixed dynamics simulation algorithm which describes the biochemical reactions where some of the species can be treated as continuous variables, but other species are naturally described as discrete stochastic variables. We then attempt to describe an approximation to the continuous dynamics in a situation where the discrete variables change on a much faster relative time scale, analogous to the quasi-equilibrium assumption made in fully deterministic systems. However our approximation method mostly fails to capture the true correction to the dynamics; we speculate as to the reasons for this.

## BIOGRAPHICAL SKETCH

Fergal Casey was born on the 17th November 1976 in Dublin, Ireland to Grainne and Michael. He spent most of his childhood and had most of his schooling in Dublin apart from a 4 year period 1980-1984 which was spent in Washington D.C. He studied at Trinity College Dublin, obtaining a B.A. in Physics in 1997 and then he studied for a B.A. in Mathematics, also at Trinity College Dublin. He started a Ph.D. in Applied Mathematics in Cornell in Fall 2001 and is returning homeward to University College Dublin to begin a postdoctoral position in November 2006.

## ACKNOWLEDGEMENTS

There are many people that I would like to acknowledge and I apologize in advance if I forget anyone.

First I would like to thank my committee members John Guckenheimer, Richard Rand for their constructive criticism which have kept me on the right track. Special thanks goes to Jim Sethna, my chair, for all the guidance, encouragement throughout these past few years (aswell as financial support), and for nudging me towards computational biology, despite some initial reluctance on my part. I would like to thank the other people who have been part of our research group. Chris Myers has been a source of interesting discussions and has always been helpful with coding/software questions. To the other graduate students in the group: Josh Waterfall and Ryan Gutenkunst, they were ideal colleagues whose enthusiasm for research and good humor made spending several years in our windowless computer lab much more enjoyable than it would have been! Thanks to Rick Cerione, his students Dan Baird and Qiyu Feng for their crucial research collaboration.

From CAM, I would like to first thank Dolores Pendell for always taking care of us in CAM, she is like our fairy godmother. Also my CAM friends who I have had a great time with: Richard Casey, Yannet Interian, Mercedes Franco, Joe Tien, Erik Sherwood, Paul Hurtado, Marcel Blais, Bill Dirks and Deena Schmidt.

My Irish compatriots in Cornell: Cormac Byrne, Colman Carroll, Gavin Hurley, Stephen Butler, Conor Foley and Roisin Owens for all those late nights at the pubs and fantastic skiing trips.

Special thanks to my preciosa, Emilia Huerta-Sanchez. Meeting her was the best part of being in graduate school and we will continue to share our lives together

long after I have forgotten what my dissertation was about.

Last but not least, my parents, Grainne and Michael, and my two brothers, Rowan and Michael.

# TABLE OF CONTENTS

Biographical Sketch . . . . .	iii
Acknowledgements . . . . .	iv
List of Figures . . . . .	viii
<b>1 Overview</b>	<b>1</b>
<b>2 Optimal experimental design in an EGFR signaling and down-regulation model</b>	<b>5</b>
2.1 Introduction . . . . .	6
2.2 Methods . . . . .	9
2.2.1 Mathematical model, parameter and prediction uncertainties	9
2.2.2 Optimal Experimental Design . . . . .	13
2.3 Results . . . . .	17
2.3.1 Model refinements . . . . .	17
2.3.2 Predictions . . . . .	20
2.4 Discussion . . . . .	28
<b>3 Variational method for estimating the rate of convergence of Markov Chain Monte Carlo algorithms</b>	<b>30</b>
3.1 Introduction . . . . .	31
3.2 Markov Chain Monte Carlo . . . . .	32
3.2.1 Metropolis-Hastings and smart Monte Carlo . . . . .	34
3.2.2 Variational method . . . . .	35
3.3 Examples . . . . .	37
3.3.1 Gaussian target density . . . . .	37
3.3.2 Quartic target density . . . . .	44
3.4 Multidimensional target densities . . . . .	48
3.5 Conclusion . . . . .	55
<b>4 Averaging for fast stochastic perturbations of differential equations</b>	<b>58</b>
4.1 Introduction . . . . .	58
4.2 Mixed dynamics simulation . . . . .	61
4.3 Auto-inhibitory gene dynamics . . . . .	62
4.4 Conclusion . . . . .	73
<b>A</b>	<b>77</b>
A.1 Supplementary information for Chapter 2 . . . . .	77
A.1.1 Experimental data . . . . .	77
A.1.2 Model details . . . . .	80
A.1.3 Parameter sensitivities . . . . .	80
A.1.4 Posterior parameter distribution . . . . .	83

A.1.5	Parameter information and prediction uncertainty . . . . .	87
<b>B</b>		<b>88</b>
B.1	Parameter and residual sensitivity matrices . . . . .	88
B.1.1	Residual response with respect to parameters . . . . .	89
B.1.2	Parameter response with respect to residuals . . . . .	89
B.1.3	Residual response with respect to residuals . . . . .	90
B.1.4	Parameter response with respect to parameters . . . . .	91
B.1.5	Response matrices for the EGFR model . . . . .	92
B.2	Optimization and data fitting . . . . .	97
B.2.1	Large range of scales . . . . .	97
B.2.2	Ill-conditioned curvature matrices . . . . .	102
B.2.3	Linearly dependent search directions . . . . .	103
B.2.4	Fake data . . . . .	106
<b>Bibliography</b>		<b>107</b>

## LIST OF FIGURES

2.1	Schematic diagram showing the set of interactions in the model of EGFR signaling, endocytosis and down-regulation (see also [22]). Phosphatases are not shown. . . . .	8
2.2	Example of experimental fit and uncertainties around the best fit trajectory (dotted lines) for total surface receptor (experiment 1 in Appendix A.1). . . . .	17
2.3	Total surface receptor numbers after EGF stimulation in stably expressing v- <i>Src</i> cells. Endogenous levels of Cool-1 (dashed curve) or overexpressed Cool-1 (solid curve). The dotted lines show the uncertainties in each of the best fit predictions . . . . .	21
2.4	Predictions with uncertainty on the time course of the triple complex consisting of active Cool-1, Cbl and active Cdc42. The quantity plotted is the percentage of total Cbl that is bound in the triple complex. . . . .	22
2.5	(a) Trajectory of total active Cdc42 (solid line) with single sequential design measurement (marked with a dot) and approximate continuous design weights (dotted line) to reduce the average variance of the prediction on the Cool-1, Cbl, Cdc42 complex. The weights are optimized over 160 uniformly spaced hypothetical measurements placed between 0 and 80 minutes on Cdc42. (b) Shows the reduction in the original uncertainty bounds resulting from the single measurement (dotted line) and the approximate continuous design measurement (dashed line) in (a). Compare with Fig. 2.4 before the addition of new measurements. . . . .	24
2.6	(a) Eigenvalues of the approximate parameter covariance matrix, $M^{-1}$ , with (light squares) and without (dark circles) the optimally designed data to reduce the uncertainty of the triple complex trajectory. (b) Individual parameter standard deviations, sorted from smallest to biggest with (light squares) and without (dark circles) the optimally designed data. Note that the cutoff in the spectrum of eigenvalues is due to the prior information assumed on parameters ranges. Even with prior information, 40 of the 60 parameters have uncertainties corresponding to a greater than 20-fold increase or decrease in their non-logarithmic values. . . . .	25
2.7	(a) Without refitting to the new total active Cdc42 data, our prediction matches the data using only a single multiplicative factor. a.u. = arbitrary units. (b) Reduced uncertainty on the time course of the active Cool, Cbl, and active Cdc42 complex for the optimal set of design points (dashed line) (same as Fig. 2.5 (b) ) and for the real data (dotted line). . . . .	27

3.1	Variational estimate on the second eigenvalue for the one dimensional Gaussian problem using the standard MH method, with $k = 1.0$ . The variational estimate is the solid line and the empirically determined values are marked with stars. Some of the empirical convergence rates seem to be less than the lower bound, but this is due to inaccuracies in their estimation . . . . .	38
3.2	Regions in $xy$ plane where acceptance probability $\alpha(x, y) < 1$ or $\alpha(x, y) = 1$ , when (a) $b(1, h, l) \geq 0$ and (b) $b(1, h, l) < 0$ . The equation for the boundary is shown in (c), see Eqn. 3.9 with $k = 1.0$ . (The standard MH algorithm will only have regions described by (a).) . . . . .	40
3.3	Estimate of second eigenvalue for the symmetrized smart Monte Carlo operator. (a) $k = 1$ is fixed and $h, l$ are allowed to vary. ( $h = 1.0, l = 1.0$ is the optimal scaling for deterministic and random parts of the step.) (b) We take a slice through this surface at $l = 1.5$ and empirically determine the second eigenvalue at points along this curve (stars). The error bars are too small to be seen. Dashed lines are discontinuities. . . . .	41
3.4	Forty iterates of the smart Monte Carlo algorithm (solid lines), Eqn. 3.8, when the initial distribution is normal with standard deviation five times the Gaussian target density (dashed line). Parameters are chosen to be in the region of no convergence ( $h = 2.0, l = 1.5$ ), see Fig. 3.3 (a). We see that the tails of the initial distribution are essentially unchanging after many iterates and have failed to converge to the target density . . . . .	43
3.5	Second eigenvalue estimate from the variational method (solid line) and data points (stars), for the quartic target density ( $k = 1$ ) using the standard MH method, Eqn. 3.7. The numerical values for $\lambda^*$ are now estimated by taking the ratio of the discrepancy from the target density in subsequent iterates and finding a single multiplicative factor which describes the decay. This is done rather than using functional forms analogous to Hermite polynomials to fit the decay, because it appears that there may be more significant contributions from higher order terms. This also explains why the lower bound shown differs more than in Fig. 3.1 and Fig. 3.3 (b). The data point shown at $1/\sqrt{2} \approx .71$ (see text) does not appear to be optimal. . . . .	46
3.6	Forty iterates of the smart Monte Carlo algorithm (solid lines), Eqn. 3.8, when the target density is quartic (dashed line). The initial distribution of points is normal with standard deviation about five times that of target density (dashed line). Parameters are arbitrarily chosen as ( $h = 1.0, l = 1.0$ ), and we see that the tails of the initial distribution are unchanged for every iterate of the algorithm. Other parameter sets tested lead to the same behaviour. . . . .	47

3.7	Contour used to evaluate Eqn. 3.19 when $\Delta E < 0$ . $r_1$ is a branch point and $r_{1,0}$ is a pole of order $(n - 1)/2$ . The contour is the same for $\Delta E < 0$ except restricted to the negative imaginary plane. . . .	55
3.8	Lower bound on second eigenvalue for the multivariate Gaussian problem, Eqn. 3.11, with $n = 11$ . Step scale = $\sqrt{1/l_n}$ . $k_n = 1$ sets the scale of the target density in the last direction. The test function is chosen as the negative of the target density perturbed by a delta function (solid line) or as the target density itself in all directions but the last (dashed line). The estimate for the lower bound is a maximum of the two curves. . . . .	56
4.1	Auto-inhibitory one gene network. When the operator site P is cleared mRNA transcripts can be made at a rate $k_t$ and translation occurs at a rate $k_t r$ to make protein A. However A binds to its own operator site and represses transcription. The mRNA is degraded at rate $k_d m$ and the protein is degraded at rate $k_d$ . . . . .	63
4.2	The stochastic trajectories for the mRNA level (solid line) and protein level (dotted line). The telegraph noise, $P$ , alternates between 1 (gray filled) and 0 (white). Parameters are $\alpha = 20.0$ , $\beta = 2.0$ , $k_b = .5$ and $k_u = 2.5$ (the $k_b$ , $k_u$ , values do not correspond to the fast noise regime, but are chosen to show the stochastic transitions).	65
4.3	Phase portraits for the $P = 0$ system (pink curves) and the $P = 1$ system (light blue curves) for the same parameters as in Fig. 4.2. Stable fixed point for each system shown by the black dot. A sample trajectory including the stochastic transitions is shown by the black curve—alternating along trajectories of both vector fields. . . . .	66
4.4	The sample paths for the perturbed telegraph noise (solid line) and the unperturbed telegraph noise (dotted line). The perturbation occurs at a time $r$ in the past and we evaluate its effect at time $t$ . The difference path is how we interpret the functional derivative of the telegraph signal with respect to its transition rate to the lower state. (The upper state has value $1 - \langle P \rangle$ and the lower state has value $-\langle P \rangle$ for $\tilde{P}$ .) . . . . .	69
4.5	(a) Mean protein trajectory when $k_b = 2.5$ , $k_u = 50$ , $\alpha = 20$ , $\beta = 2.0$ . Averaged over 800000 sample paths. Error bars are too small to be seen. (b) Relative differences for the asymptotic and corrected equations. Relative differences are defined as numerical mean trajectory minus theoretical mean trajectory (asymptotic (light circles) or with correction (dark triangles)) divided by the error bars for the numerical mean trajectory. . . . .	74

4.6	(a) Mean protein trajectory when $k_b = 5.0$ , $k_u = 5.0$ , $\alpha = 20$ , $\beta = .1$ . The mean times in the up and down states are approximately .2. Averaged over 850000 sample paths. Error bars are too small to be seen. (b) Relative differences for the asymptotic and corrected equations. Relative differences are defined as numerical mean trajectory minus theoretical mean trajectory (asymptotic (light circles) or with correction (dark triangles)) divided by the error bars for the numerical mean trajectory. . . . .	75
A.1	Experimental data and fits for all the experiments described in the text. Experiment 4: surface EGF (light triangles), internal EGF (gray squares), degraded EGF (dark circles). Experiment 5: Cdc42(F28L) overexpression (light triangles), Cdc42(F28L/DL8) (gray squares), control (black circles). Experiment 8: Cdc42 siRNA (light triangles), control (black circles). Experiment 9: Cool-1 siRNA (gray squares), control (light triangles). All other experiments measure a single species for a single experimental condition described in text. . . . .	81
A.2	Components of the first three eigenvectors of the FIM evaluated at the best fit for the EGFR model . . . . .	82
A.3	Components of the first three eigenvectors of the FIM evaluated at the best fit for the EGFR model with simulated data on all species at 2 minute intervals . . . . .	83
A.4	The last three principal component axes, in reverse order, (most tightly constrained directions) for a sample of approximately 5000 parameter sets sampled from the posterior distribution. . . . .	84
A.5	The total surface receptor numbers after EGF stimulation in stably transfected v- <i>Src</i> cells. The two experimental conditions are endogenous levels of Cool-1 (dashed curve) or overexpressed Cool-1 (solid curve). (a) The total surface receptor trajectory is a median of all the trajectories in the posterior distribution. The uncertainties are the boundaries of the 68% credible regions (dotted lines) to correspond with the one standard deviation errors shown in the main text. (b) The linearized estimates, shown for comparison. . .	85
A.6	The level of the triple complex in wild type cells with endogenous EGFR. (a) Median trajectory (solid curve) and the uncertainties given by the boundaries of the 68% credible region (dotted lines). (b) The linearized estimates, shown for comparison. Note that the best fit trajectory in (b) is noticeably different from the median trajectory shown in (a) . . . . .	86
A.7	The uncertainties on the prediction of the triple complex with no formation/dissociation rate constant information (dashed line) and assuming the relevant rate constants are known to within 5% (dotted line). . . . .	87

B.1	(a) The $J$ matrix, showing residual sensitivities to parameters. (b) Residuals of the total Cool-1 active measurements and dominant parameters . . . . .	92
B.2	(a) The $\partial\theta/\partial r$ matrix, showing parameter sensitivities to residuals. (b) Residuals of the total EGFR measurements and dominant parameters . . . . .	93
B.3	(a) The $\partial\theta/\partial r$ matrix, showing parameter sensitivities to residuals. (b) Residuals of the total EGFR measurements and dominant parameters . . . . .	94
B.4	(a) The correlation matrix. (b) Binding and unbinding constant correlations for Cbl binding to ubiquitinated receptor. . . . .	95
B.5	(a) Eigenvalues for the FIM and (b) Sorted diagonal elements, giving the (approximate) second derivative of the cost with respect to each parameter. The values are plotted assuming a prior distribution on parameters (dark circles), or assuming no prior distribution (light triangles). We impose the same prior distribution on parameters as in Chapter 2, which constrains the fluctuations to within a 1000-fold increase or decrease in the non-logarithmic parameters. The prior is responsible for the “flattening off” of the eigenvalue spectrum and of the sorted diagonal elements. Note that the largest eigenvalues correspond to an allowed fluctuation of less than 1% in the non-logarithmic parameters, the lowest eigenvalues with priors give the 1000-fold fluctuations, but <i>without priors</i> the lowest eigenvalues correspond to fluctuations with fold changes of $\exp(\pm 3^6)$ , which are clearly unphysical. . . . .	99
B.6	Bar chart showing the average percentage of failures for 3 badly scaled test functions in the test suite [49] over 100 randomized initial conditions. Each test function is 16 dimensional and failure is defined as a cost greater than 1 after the maximum number of iterations has been exceeded (the minimum possible cost is zero). LM std. and CG std. are the non-scale invariant Levenberg-Marquardt (LM) and conjugate gradient (CG) methods. LM scale1 is the Numerical Recipes scale invariant method [53]. LM scale2 and CG scale are our scale invariant methods discussed in text. . . . .	101

# Chapter 1

## Overview

Systems biology is a relatively new field which aims for an integrated understanding of biological processes on the cellular, organismal or even ecological level. It is broadly divided into two categories: mathematical modeling of complex biological processes, and the collection/analysis of large genomic, proteomic or metabolomic data sets. The mathematical modeling approach presumes the existence of a “wiring” diagram or network picture which already provides the basic set of interactions underlying the experimental observations. The task of mathematical modeling is to refine the set of interactions within the network picture and to allow specific biological hypotheses to be tested as they relate to behavior of the system. Large data set collection and analysis has the murkier objective of uncovering basic interactions between biological units (genes, RNA, proteins, metabolites etc.), the connections between genotype and phenotype, and in some cases of reconstructing the network diagram. The two sides are of course complementary; analyzing large data sets is facilitated by knowing something about the underlying processes which produce the experimental outcomes.

In this thesis, we focus on the first objective: we build a model, based on current

biological knowledge, of certain cellular biochemical pathways that are specifically probed by molecular biology experiments. We then discuss some methods that can be used to analyze the model, to make useful predictions, and to determine the relative importance of components within the biological network.

Chapter 2 introduces a biological model of the processes which control the response of cultured cells to a growth hormone stimulus. The system is probed by a number of molecular biology experiments which measure the activity or relative amounts of the signaling proteins within the network over time. Given these measurements, we first optimize the free parameters of the model in order to reproduce the observed behavior. This difficult process leads to a number of refinements within the model—incorporating new reactions or changing the relative strength of existing interactions. Some of the difficulties of the optimization process are discussed in Appendix B.2. Next, we validate the model by making a prediction which matches qualitative experimental behavior. Fundamental for making predictions is the assessment of uncertainties; if the confidence interval on a prediction is too large, the prediction cannot be used for model validation. Finally, we introduce the optimal experimental design methodology which provides a means for testing biological hypotheses with good precision, by suggesting a minimal number of extra measurements that need to be made. A further analysis of this model is done in Appendix A.1 and in Appendix B.1. There we look at various measures of the sensitivity of parameters or parameter combinations to subsets of the experimental data. This type of analysis allows us to pick out crucial interactions in the network which appear to control the dynamical behavior.

Chapter 3 analyzes some of the algorithms which are used to make uncertainty estimates (on both parameters and on predictions). These algorithms are com-

monplace in Bayesian statistics applications, the goal being to generate a sample from the posterior parameter distribution that is consistent with the experimental data. These methods are attractive as they offer a way to automatically sample all of parameter space and provide an exhaustive collection of models, each of which reproduces the experimental observations. Thus, rigorous testing of an hypothesis (about parameter values or the dynamics of the model, for example) requires evaluation on all of the posterior sample. In practice, the algorithms which generate the posterior sample are imperfect and can have very slow convergence rates. This is especially true for the class of models that we call “sloppy”: the model behavior is much less sensitive to parameter moves in some directions than in others. Therefore in Chapter 3 we suggest a straightforward method that can be used to bound the convergence rate of these algorithms. We explicitly show that when the distribution one wishes to sample from has a discrepancy in scales that is characteristic of sloppy models, the convergence properties deteriorate. We also discovered that “smart” variants of the basic algorithms which claim to sample parameter space more efficiently often completely fail to converge.

In Chapter 4, a completely different approach to modeling cellular processes is introduced; one that involves simulating reaction events stochastically. At a molecular level, this is the required description, but often the assumption is made in biomolecular reaction networks that all the species involved are present in high enough molecule number that stochastic effects can be ignored. We examine, with a toy model, a modification of the fully stochastic description: some species are in large enough number such that they can be modeled deterministically and as continuous variables, but the deterministic equations themselves change stochastically due to the presence of other species that only exist in small numbers and

take on discrete values. We present an algorithm for the solution of this problem, and also explore the application of an averaging method which should provide an effective set of deterministic equations for the expected trajectory of the continuous variables, in the limit that the reactions for the discrete variables are fast. The averaging method, however, fails to capture the correction to the dynamics for most of the parameter regimes we have examined. Despite being overly simplified, the toy model includes the effect of the inherent stochasticity of DNA-protein binding interactions, which should be accounted for in larger models also.

## Chapter 2

# Optimal experimental design in an EGFR signaling and down-regulation model<sup>1</sup>

We apply the methods of optimal experimental design to a differential equation model for epidermal growth factor receptor (EGFR) signaling, trafficking, and down-regulation. The model incorporates the role of a recently discovered protein complex made up of the E3 ubiquitin ligase, Cbl, the guanine exchange factor (GEF), Cool-1 ( $\beta$ -Pix), and the Rho family G protein Cdc42. The complex has been suggested to be important in disrupting receptor down-regulation [73, 22]. We demonstrate that the model interactions can accurately reproduce the experimental observations, that they can be used to make predictions with accompanying uncertainties, and that we can apply ideas of optimal experimental design to sug-

---

<sup>1</sup>As of this writing, this chapter is under review by *IEE Proceedings Systems Biology* with the same title and authors F.P. Casey, D. Baird, Q. Feng, J.J. Waterfall, R.N. Gutenkunst, C.R. Myers, K.S. Brown, R.A. Cerione and J.P. Sethna

gest new experiments that reduce the uncertainty on unmeasurable components of the system.

## 2.1 Introduction

The epidermal growth factor receptor (EGFR) is a transmembrane tyrosine kinase receptor which becomes activated upon binding of its ligand, epidermal growth factor (EGF), and signals via phosphorylation of various effectors [12]. Besides sending signals to downstream effectors, the activated EGFR also will initialize endocytosis which is followed by either degradation or recycling of the receptor. These are the normal receptor down-regulation processes. Persistence of activated receptor on the cell surface can lead to aberrant signaling and transformation of cells [71]. In addition, a variety of tumor cells exhibit overexpressed or hyperactivated EGF receptor [33, 15], indicative of the failure of normal receptor down-regulation.

We concern ourselves with building a mathematical model of the receptor endocytosis, recycling, degradation and signaling processes that can reproduce experimental data and incorporates the effects of regulating proteins that themselves become active after EGF stimulation. The schematic for the model is shown in Fig. 2.1. In particular, we examine the roles of the GEF, Cool-1, and the GTPase, Cdc42 that have recently been discovered to be important for EGFR homeostasis [22, 73] through their interaction with the E3 ubiquitin ligase, Cbl. There is evidence for two interaction mechanisms which disrupt the normal receptor down-regulation.

The first mechanism involves the formation of a complex between active Cool-1,

active Cdc42 and Cbl. After activation of the receptor, Cool-1 becomes phosphorylated through a Src - FAK phosphorylation cascade. Phosphorylated Cool-1 has GEF activity and in turn activates Cdc42 by catalyzing the exchange of GDP for GTP. Unlike other GEFs however, activated Cool-1 can remain bound to its target, Cdc42, [73] and can then form a complex with Cbl (mediated through Cool-1 binding), effectively sequestering Cbl from the receptor. Therefore the internalization and degradation of the receptor is inhibited and its growth signal is maintained. (We use the ERK pathway as a readout on the receptor mitogenic signal.) The second mechanism is based on the findings of [22] that activated Cool-1 can directly bind to Cbl on the receptor and block endocytosis in a manner we hypothesize be analogous to the action of Sprouty2 [72].

To maintain normal receptor signaling, we postulate it is crucial that deactivation of Cool-1 and subsequent dissociation of the Cbl, Cool-1 and Cdc42 complex occur. Then Cbl can induce receptor internalization and ubiquitin tag it for degradation in the lysosome. Internalized receptor lacking ubiquitin moieties can be returned to the cell surface from the early endosome via the recycling pathway.

The role of Cbl in the degradation mechanism for the receptor has been understood for some time [45, 20, 27]. However, its function in mediating endocytosis still remains controversial (e.g. [35, 38, 51, 16, 66]) as the receptor can be internalized through more than one endocytic pathway. We do not address that issue here but rather we assume in our model that Cbl association and activation is necessary for endocytosis, whether through a CIN85-endophilin interaction [68] or through ubiquitination of the receptor [66] and therefore we do not include a separate Cbl-independent endocytosis pathway. The overall set of these protein-protein interactions is summarized in Fig. 2.1 (we also incorporate phosphatases

in the model to act on the various phosphorylated species, but this is not shown in the network figure). There is a significant overlap between our model and previous models of EGF receptor signaling and/or trafficking, [62, 41, 55, 5]. Since we wish to focus on the role of the Cool-1/Cdc42 proteins within the network and to demonstrate the utility of optimal experimental design, we leave out some of the known intermediate reactions involved in the MAPK and EGFR-Src activation pathways, preferring a “lumped” description which is more computationally manageable.

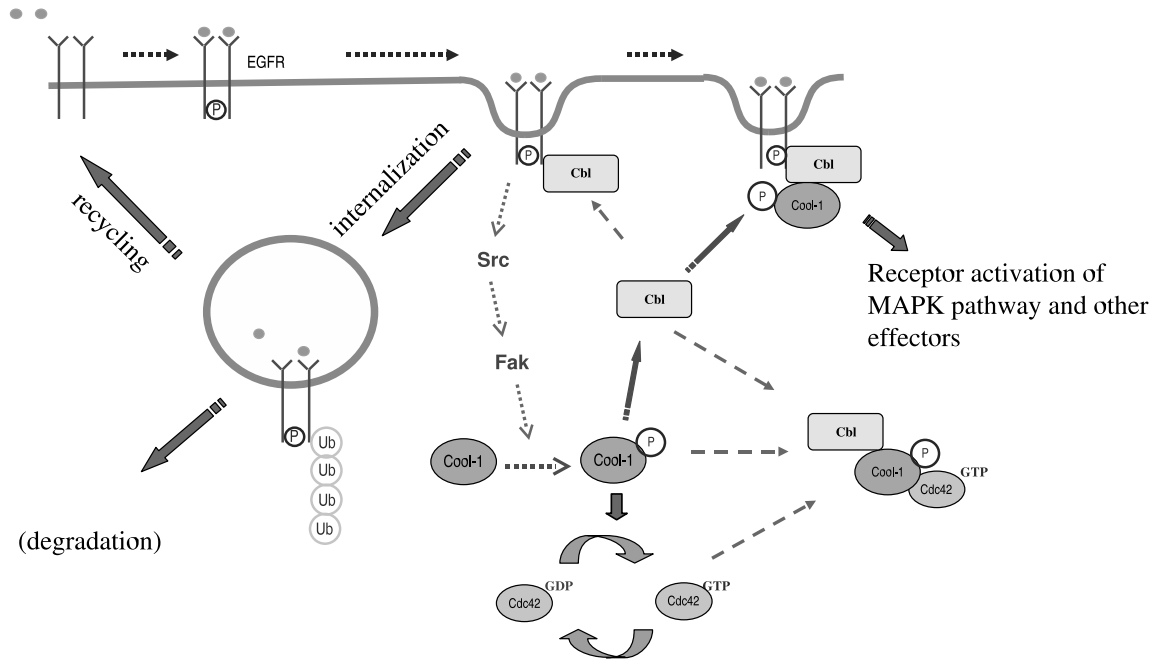


Figure 2.1: Schematic diagram showing the set of interactions in the model of EGFR signaling, endocytosis and down-regulation (see also [22]). Phosphatases are not shown.

The goals of this manuscript are to demonstrate how a modeling approach can be used to

- (a) refine the necessary set of interactions in the biological network,

- (b) make predictions on unmeasured components of the system with good precision and
- (c) reduce the prediction uncertainty on components that are difficult to measure directly, by using the methods of optimal experimental design.

## 2.2 Methods

### 2.2.1 Mathematical model, parameter and prediction uncertainties

Before we introduce the algorithms needed to address the design question, we define the model and data in more detail. Our differential equation model for EGFR signaling and down-regulation contains 56 unknown biochemical constants: 53 unknown rate and Michaelis Menten constants (where they can be found, initial estimates were drawn from the literature), and 3 unknown initial conditions which we found useful to vary. The dynamical variables are comprised of 41 separate chemical species, including complexes. The data consist entirely of time series in the form of Western blots. (The data both come from the lab of the co-authors and from the literature, see Appendix A.1 for details.) We have been careful to select data only on NIH-3T3 cells, and in experimental conditions where the cell has been serum-starved prior to EGF stimulation, to prevent activation events not related to the EGFR ligand binding. Most of the time series data are over a period less than a few hours which allows us to ignore transcriptional processes.

Since we have no information on most of the biochemical constants, we must infer them from the data. Therefore we optimize a cost function which measures

the discrepancy of simulated data from the real data,

$$C(\theta) = \sum_{\alpha=1}^D \sum_{i=1}^{m_{\alpha}} \left( \frac{y_{\alpha}(t_{\alpha i}, \theta) - d_{\alpha i}}{\sigma_{\alpha i}} \right)^2 = \sum_{i=1}^{m_{\alpha}} r_{\alpha i}^2(\theta) \quad (2.1)$$

where  $\alpha$  is an index on the  $D$  measured species,  $m_{\alpha}$  is the number of time points on species  $\alpha$ ,  $y$  is the trajectory of the differential equation model,  $\theta$  is a vector of the logarithm of the biochemical constants,  $d_{\alpha i}$  is the measured value at time  $t_{\alpha i}$  for species  $\alpha$  and  $\sigma_{\alpha i}$  is the error on the measured value. We use the notation  $r_{\alpha i}(\theta) = (y_{\alpha}(t_{\alpha i}, \theta) - d_{\alpha i})/\sigma_{\alpha i}$  to denote the residuals. In other words, we have a standard weighted least squares problem to reduce the discrepancy of the model output to the data by varying  $\theta$ . (We use the logarithm of the biochemical constants as it allows us to apply an unconstrained optimization method while maintaining the positivity constraint and it removes the discrepancies between biochemical values that have naturally different scales in the problem). As absolute numbers of proteins in the network cannot be accurately measured, data sets measuring activities of proteins are fit up to an arbitrary multiplicative scale factor, which adds parameters to the model not of direct inferential interest (*nuisance parameters*). Where the relative quantity of a species can be measured (normalized by the level before EGF stimulation for example), the output of the differential equations are similarly scaled by an appropriate common factor.

After the model has been successfully fit to the experimental data, we have a parameter estimate  $\hat{\theta}$  which in general will have large covariances, approximated by the inverse of the *Fisher information matrix* (FIM). The FIM is defined as

$$M = \mathbf{E}[\partial^2 C / \partial \theta^2]$$

where the expectation is over the distribution of errors in the data, which are

assumed to be Gaussian. Using Eqn. 2.1 this can be written as

$$M = \sum_{\alpha=1}^D \sum_{i=1}^{m_{\alpha}} \frac{1}{\sigma_{\alpha i}} \frac{\partial y_{\alpha}(t_{\alpha i}, \theta)^t}{\partial \theta} \Big|_{\hat{\theta}} \frac{1}{\sigma_{\alpha i}} \frac{\partial y_{\alpha}(t_{\alpha i}, \theta)}{\partial \theta} \Big|_{\hat{\theta}} + \frac{\mathbf{E}[r_{\alpha i}]}{\sigma_{\alpha i}} \frac{\partial^2 y_{\alpha}(t_{\alpha i}, \theta)}{\partial \theta^2} \Big|_{\hat{\theta}} \quad (2.2)$$

$$= \sum_{\alpha=1}^D \sum_{i=1}^{m_{\alpha}} \frac{1}{\sigma_{\alpha i}} \frac{\partial y_{\alpha}(t_{\alpha i}, \theta)^t}{\partial \theta} \Big|_{\hat{\theta}} \frac{1}{\sigma_{\alpha i}} \frac{\partial y_{\alpha}(t_{\alpha i}, \theta)}{\partial \theta} \Big|_{\hat{\theta}} = J^t J \quad . \quad (2.3)$$

where, in the last step, we assume that the model fits perfectly, i.e. at the best fit, the expectation of the residuals is zero,  $\mathbf{E}[y_{\alpha}(t_{\alpha i}) - d_i] = 0$ . The  $i^{\text{th}}$  parameter uncertainty is given by the square root of the  $i^{\text{th}}$  diagonal element of the inverse FIM.  $J = (1/\sigma_{\alpha i}) \partial y_{\alpha}(t_{\alpha i}, \theta) / \partial \theta \Big|_{\hat{\theta}}$  is the sensitivity matrix of residuals with respect to parameters at the best fit and is the analog to the *design matrix* in a linear regression setting. The *design space* is the range of species  $\alpha$  and of time points  $t_{\alpha i}$  for which measurements could be taken. ( $\alpha i$  is the row index of  $J$ .) Note that the FIM is simply a positive definite approximation to the quadratic approximation of the cost function,  $C(\theta)$ , about the minimum,  $\hat{\theta}$ .

Alternatively, we can regard the inverse FIM as a variance estimate for the parameters, assuming a linearized model about the best fit. Minimizing the cost function is equivalent to finding the solution, in a least squares sense, to the non-linear set of equations  $r(\theta) = 0$ . ( $r(\theta)$  is the vector of residuals over all indices,  $\alpha$  and  $i$ .) Assuming a linearized model for the residual function,  $r(\theta)$ , about the best fit parameters,  $\hat{\theta}$  we have the linearized least squares problem

$$r(\hat{\theta}) + J \Delta \theta = 0$$

Note that because we have scaled the residuals with respect to the measurement errors  $r(\hat{\theta})$  is a multivariate Gaussian random variable with a mean vector of zeros (the model fits perfectly) and a covariance matrix which is the identity.  $J = (1/\sigma) \partial y / \partial \theta$  is the sensitivity of the model outputs,  $y$ , with respect to parameters

as before. The solution to the *normal equations*, giving the minimum of  $\|r(\hat{\theta}) + J\Delta\theta\|^2$  with respect to  $\Delta\theta$ , for this linear system are

$$\Delta\theta = (J^t J)^{-1} J^t r(\hat{\theta})$$

This gives a least squares estimate for  $\Delta\theta$  of 0, since  $J^t r(\hat{\theta}) = \nabla C(\hat{\theta}) = 0$ . However, we are looking for the variance estimate about the minimum. To compute this, note that for any random vector  $X$ , in  $\mathbf{R}^N$  and for any nonrandom  $M$  by  $N$  matrix,  $A$ :

$$\text{Cov}(AX) = ACov(X)A^t \quad (2.4)$$

where Cov means covariance. Using this fact and that  $\text{Cov}(r) = I$ , we see that  $\text{Cov}(\Delta\theta) = (J^t J)^{-1}$ , which is the same formula as in Eqn. 2.3.

We can also make predictions on components of the trajectory (measured or unmeasured),  $\hat{y}_\beta(t) = y_\beta(t, \hat{\theta})$ . The variances on these quantities are given by

$$\text{Var}(\hat{y}_\beta(t)) \approx \frac{\partial y_\beta(t, \theta)^t}{\partial \theta} \Big|_{\hat{\theta}} M^{-1} \frac{\partial y_\beta(t, \theta)}{\partial \theta} \Big|_{\hat{\theta}} \quad (2.5)$$

The form of Eqn. 2.5 can be thought of as a combination of the underlying parameter uncertainty, quantified by  $M^{-1}$ , and the linear response of the system to the parameter uncertainty, quantified by the sensitivities.<sup>2</sup> Note that  $M$  is also computed using the sensitivities of the trajectory of the differential equations, which we obtain by implementing the forward sensitivity equations [63]. In practice,  $M$  is close to singular if we do not include some prior information on parameter ranges. Therefore we assume a Gaussian prior on the parameters centered on the best fit values and with a standard deviation of  $\log(1000)$ . (This corresponds to

---

<sup>2</sup>The formula is simply derived by noting that the linearized changes in  $y_\beta(t)$  are described by  $\Delta y_\beta(t) = (\partial y_\beta(t, \theta) / \partial \theta)^t \Big|_{\hat{\theta}} \Delta\theta$  and then applying Eqn. 2.4, recalling that  $\text{Cov}(\Delta\theta) = (J^t J)^{-1}$ .

an approximately 1000-fold increase or decrease in the non-logarithmic best fit biochemical values.)

We recognize there can be other sources of uncertainty in predictions, for example if the dynamics of the system are modeled stochastically or if there is model uncertainty that needs to be taken into account. The former is not relevant here as the measurements we fit are not on the single cell level, but rather the average of large populations of cells. The latter is certainly of interest but we choose an approach where model errors are corrected during the fitting and validation process, rather than included *a priori* in the model definition.

Given the approximate nature of variance estimates derived from the Fisher information matrix and the linearized model response, we supplemented these calculations with a computationally intensive Bayesian Markov Chain Monte Carlo (MCMC) method to compute credible intervals for the predictions we make on the model (see Appendix A.1). The estimates from the Bayesian MCMC approach are in sufficient agreement with the linearized error analysis results that we believe the optimal experimental design algorithms introduced below are justifiably aimed at reducing the approximate uncertainties of Eqn. 2.5. Using MCMC for error estimates within the framework of the optimal design algorithms would be computationally infeasible.

### 2.2.2 Optimal Experimental Design

Optimal experimental design is a technique for deciding what data should be collected from a given experimental system such that quantities we wish to infer from the data can be done so with maximum precision. Typically the network as shown in Fig. 2.1 has components that can be measured (e.g. *total* levels of active

Cdc42, *total* levels of surface receptor etc.) and components that are not directly measurable (e.g. levels of the triple complex comprising Cool-1, Cdc42 and Cbl). Therefore we can pose the question of how to minimize the average prediction uncertainty on some unmeasurable component of interest by collecting data on measurable components of the system (we will use the term *unmeasurable* loosely for the remainder to describe species that are between difficult and impossible to measure by standard methods). This is just one possible *design criterion*, called V-optimality in the literature; other criteria involve minimizing the total parameter uncertainty in the system (D-optimality), minimizing the uncertainty in the least constrained direction in parameter space (E-optimality) or minimizing the maximum uncertainty in a prediction (G-optimality) [2]. Other authors [21, 59, 43] have focused on reducing parameter uncertainty but we believe that complex biological models, even with large amounts of precise time series data, have intrinsically large parameter uncertainty [8, 28, 70]. On the other hand, even with no extra data collection, the uncertainty on unmeasured time trajectories in these biological systems can be surprisingly small despite the large parameter uncertainty [28].

By altering the form of the matrix  $J$  in Eqn. 2.3, by measuring different species at different times, we have the possibility of reducing the average variance of  $\hat{y}_\beta$ , which is an integral over time of the quantity defined in Eqn. 2.5. We discuss the types of design and algorithms that can be used to achieve this.

A distinction must be made between *starting designs* and *sequential designs*. A starting design is one in which no data has been collected and the experimenter would like to know what design is best to minimize a given criterion function. Within this category are two subcategories: *exact designs* and *continuous designs*. Exact designs refer to the optimal placement of a finite number of design points.

As the design points need to be assigned amongst all the measurable species in the system the optimization problem is of a combinatorial nature. There have been specific algorithms developed for this situation [2] which involve choosing some initial design with the required number of points and then randomly modifying it by doing exchanges, additions and deletions. More general global optimization algorithms have been applied to the problem of finding exact designs in differential equation and regression models [39, 6].

Continuous designs refer to the selection of a *design measure*,  $\eta$ , which is equivalent to a probability density over the design space. The advantage of assuming a continuous design is that the criterion function can then be differentiated with respect to the design measure and tests for optimality can be derived. Asymptotically, for a large number of design points the continuous and exact designs should coincide. For a *linear* model described by  $y = f(t)^t\theta + \epsilon$  where  $f(t) \in \mathbf{R}^N$  and  $\epsilon$  is an error term, the FIM is

$$M(\eta) = \int_{\tau} f(t)f(t)^t\eta(x) dt$$

by definition of the design measure,  $\eta$ . However,  $M$  is a symmetric  $N \times N$  matrix made up of a convex combination of the rank one symmetric matrices,  $f(t)f(t)^t$ . Therefore it can be represented by a convex combination of at most  $N(N + 1)/2$  design points (from Caratheodory's Theorem)  $x_1, \dots, x_{N(N+1)/2}$ , i.e. as a convex combination of delta function probability measures on those points. In other words even continuous optimal designs for linear models have only a finite number of design support points [67]. In one of the approaches that follows, we will attempt to find a continuous design by approximating the design measure by a number of finely spaced measurement points with weights associated with each one, and we will see that a near optimal design is in fact only supported on a small subset of

those points.

Sequential designs are more relevant to the situation we consider here: experimental data have already been collected and the model has already been fit. Therefore we can get an initial estimate for the parameters in the system and we can evaluate the FIM. Suppose that the current design already has  $n$  points and the current FIM is  $M_n = J_n^t J_n$ . The effect of adding the  $(n + 1)^{th}$  design point (e.g.  $y_\alpha$  at time point  $t_{\alpha i}$ ) merely adds a single row to  $J_n$ . Therefore the new FIM is the old FIM plus a rank one update:

$$M_{n+1} = J_{n+1}^t J_{n+1} = J_n^t J_n + \frac{1}{\sigma_{\alpha i}^2} \frac{\partial y_\alpha(t_{\alpha i})}{\partial \theta} \Big|_{\hat{\theta}} \frac{\partial y_\alpha(t_{\alpha i})}{\partial \theta} \Big|_{\hat{\theta}}^t .$$

The new inverse FIM is also a sum of terms (by applying the Sherman-Woodbury-Morrison formula [26]): one involving the inverse of the old FIM and the other involving the sensitivity vector at the new point,  $\partial y_\alpha(t_{\alpha i})/\partial \theta|_{\hat{\theta}}$ , so evaluating Eqn. 2.5 for a large number of proposed measurements is computationally inexpensive.

We take an approach which is a combination of continuous design and sequential design: assume that some initial experiments have already been carried out and we have an FIM for the system. We will then define a cost function  $K(\alpha, t_{\alpha i})$  based on the integral of Eqn. 2.5 and minimize it with respect to  $\alpha$  and  $t_{\alpha i}$ . Initially the minimization looks for the best single data point to reduce the uncertainty (a sequential design method). Once we know for which species the data needs to be collected, we can then place many potential measurements on that species with associated weights and minimize over the weights (to mimic continuous design methods where the set of weights is the approximate design measure).

## 2.3 Results

### 2.3.1 Model refinements

The model was fit to 11 data sets, all Western blot data that describe various signaling, internalization and degradation events that are triggered after receptor activation by ligand, see Appendix A.1 for the full set of fitted time series and description of experiments. As an example of a experimental fit with uncertainties, we show in Fig. 2.2 the best fit time course and standard deviation for total surface receptor from one of the experiments for which data was included in the model (experiment 1 in Appendix A.1).

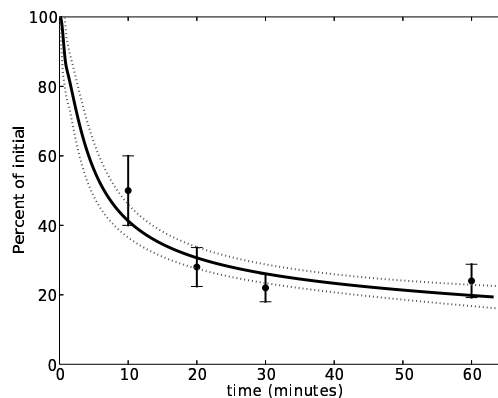


Figure 2.2: Example of experimental fit and uncertainties around the best fit trajectory (dotted lines) for total surface receptor (experiment 1 in Appendix A.1).

During the iterative process of fitting and model refinement we discovered certain interactions and model parameters had to be adjusted to be consistent with the experimentally observed behavior. These can be viewed as predictions of putative interactions, that emerge from the modeling process. We briefly summarize these adjustments below.

(1) It appears necessary to incorporate an interaction to allow the triple complex to be dissociated by a dephosphorylation reaction. In particular a reaction was needed whereby Cool-1 within the complex could be inactivated by its own dedicated phosphatase (a possible candidate already present in the system is SHP-2, which has been shown to dephosphorylate the related Sprouty protein [29]). Without this effect, we would not observe the complete deactivation of Cool-1 as it would be “protected” within the triple complex. Additionally, a sensitivity analysis to determine dominant reactions in the model identified phosphatase reactions as important (see Appendix A.1).

(2) Interestingly, there is an important balance between the level of receptor and Cool-1 in the system to maintain the correct dynamics: if the level of receptor greatly exceeds the Cool-1 level, then the activated receptor will lead indirectly to phosphorylation of Cool-1 which in turn sustains the level of signaling receptor before significant amounts can be endocytosed. It is also essential that the protein level of Cdc42 in the system be sufficiently high, approximately balanced with the Cbl levels as they both come together in the triple complex. If this was not so, the greatly reduced Erk pathway signaling we see in the data set for the Cdc42 knockdown would not be possible to reproduce (Appendix A.1 experiment 8). Of course, Cdc42 is involved in many other cellular processes, so what is actually important here is the amount available to participate in interactions with Cbl.

(3) The F28L fast cycling (hyperactive) mutant of Cdc42 has the ability to delay endogenous receptor down-regulation for many hours beyond wild type cells (see experiment 5 in the Appendix A.1). This is only possible if the binding affinity of active Cdc42 to the Cool-1-Cbl complex is strong enough to deplete the levels of the latter and force the forward binding reaction of Cbl to activated Cool-1.

This provides a mechanism to sequester more of the Cbl protein (in both the triple complex and the Cool-1-Cbl complex) than would otherwise be possible.

In addition to the above adjustments, we made the following observations relating to the network dynamics and structure.

We find that given these experimental data sets, a single endocytosis mechanism which is Cbl dependent and solely acts on activated receptors is sufficient to describe the available data on EGFR trafficking in NIH-3T3 cells. We acknowledge that there is much controversy in the literature as to the dominant endocytosis mechanisms and required regulators, in general. However, given only a Cbl independent endocytosis mechanism, the model would be unable to account for the apparent saturation of the internalization rates for overexpressed receptors (experiments 1-3 in Appendix A.1) compared to endogenous receptors (experiment 5 in Appendix A.1). Therefore having a Cbl dependent pathway is convenient in explaining those experimental observations, although any number of proteins, not in the model, could cause saturation in the endocytic pathway.

Despite the apparently earlier activation of Cdc42 than its putative GEF, active Cool-1, (see experiments 10 and 11 in Appendix A.1) the data still supports a mechanism whereby Cdc42 activation only occurs through Cool-1. The explanation of this effect is that the level of Cool-1 is significantly higher than Cdc42. Then, while only a fraction of Cool-1 is being activated at early times, it is still sufficient to induce substantial activation of Cdc42. This is an example of an apparently contradictory experimental result which only after quantitative modeling is shown still to be consistent with the proposed mechanism. In particular, we found there was no need to invoke another parallel activation mechanism for Cdc42 (through Vav for example) as initially might have been assumed.

### 2.3.2 Predictions

Once we have a model which reproduces the experimental observations, we would like to make predictions on unmeasured or unmeasurable components of the system. The motivation is twofold. Firstly, if we make a prediction on a currently unmeasured component of the system which is subsequently measured, we have an opportunity to test the validity of our model. Secondly, if we are confident in the model, we may want to test a hypothesis about the role of an unmeasurable component in the system. If that unmeasurable component has large uncertainties, we then need to apply the methods of experimental design to improve the situation. We will discuss these issues in what follows.

#### Model validation

To first give an example of model validation, consider the qualitative observation in [22] that in stably expressing v-Src cells, in conditions where Cool-1 is overexpressed, ligand-induced receptor internalization is blocked compared to an endogenous Cool-1 control, for at least 60 minutes. The model is adjusted to simulate the conditions of these v-Src cells by making all Src in its active form, switching off Src inactivation and increasing the initial amounts 10-fold to mimic the stable transfection. We then predict the total surface receptor number under the two conditions and assign uncertainties using Eqn. 2.5. The results are shown in Fig. 2.3. The qualitative observation of strong inhibition of internalization under conditions of overexpressed Cool-1 is verified by the model. Note that in this case the uncertainties are small enough that we can confidently predict a large difference in the fraction of receptors on the cell surface after 60 minutes under the two conditions. Interestingly, the model also predicts this inhibition is much

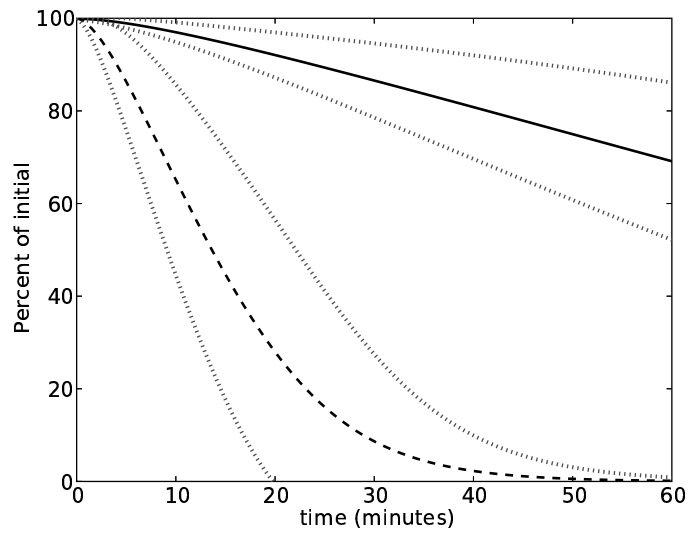


Figure 2.3: Total surface receptor numbers after EGF stimulation in stably expressing v-Src cells. Endogenous levels of Cool-1 (dashed curve) or overexpressed Cool-1 (solid curve). The dotted lines show the uncertainties in each of the best fit predictions

weaker in cells that are not stably expressing v-Src, essentially because the Cool-1 is not “pre-activated” and endocytosis of significant numbers of receptors can occur before the pool of Cool-1 can become phosphorylated.

### Optimal design for the triple complex

Another question of interest is whether the triple complex, which appears to be responsible for sequestering Cbl and blocks receptor down-regulation when Cdc42(F28L) is expressed, also forms in appreciable amounts in wild type cells. We would assume the answer is affirmative, as we observe a reduced downstream mitogenic signal from the receptor under conditions of knockdown of Cool-1 or Cdc42. Since the triple complex is an example of a species that is very difficult to obtain an accurate set of measurements for, we can test a hypothesis about its formation in wild type cells by looking at its predicted time course, Fig. 2.4. The relative amount of the triple complex is shown in Fig. 2.4, where the number

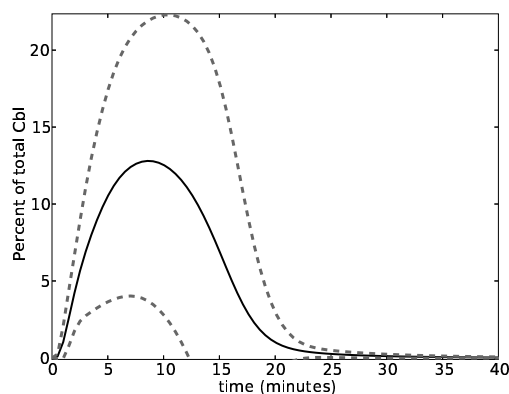


Figure 2.4: Predictions with uncertainty on the time course of the triple complex consisting of active Cool-1, Cbl and active Cdc42. The quantity plotted is the percentage of total Cbl that is bound in the triple complex.

of molecules of the triple complex has been scaled relative to the total level of Cbl. *Relative* levels of complexes and the times of formation/dissociation are more meaningful quantities than absolute numbers of molecules, which are merely rough estimates used to initialize the simulations. The best fit trajectory for the triple complex suggests that at a maximum over 12% of Cbl is sequestered in the complex which represents a significant proportion. However the uncertainty bounds are too large to make this assertion; at the level of the lower bound, less than 4% of Cbl is sequestered at a maximum, and the triple complex dissociates within 15 minutes. This motivates the need for an optimal design approach. We define a criterion which is the average uncertainty in the prediction on the triple complex. We then optimize this quantity using a sequential design approach (therefore we need to perform only line minimizations in the time coordinate for each of the 11 measurable species in the system) and follow up by finding an approximate optimal continuous design on that species. The results of such an analysis are shown in Fig. 2.5.

The most striking features of the optimal design results are that

1. a *single* measurement on total active Cdc42 can significantly reduce the variance we see in the prediction on the triple complex, as in Fig. 2.5 (b)
2. even though the approximate continuous design allows for 160 hypothetical measurements on the activity of Cdc42, the optimal design weights are concentrated to just a dozen early time points. That is, by just taking a few measurements we can get a design very close to the optimal continuous design for measuring total active Cdc42.

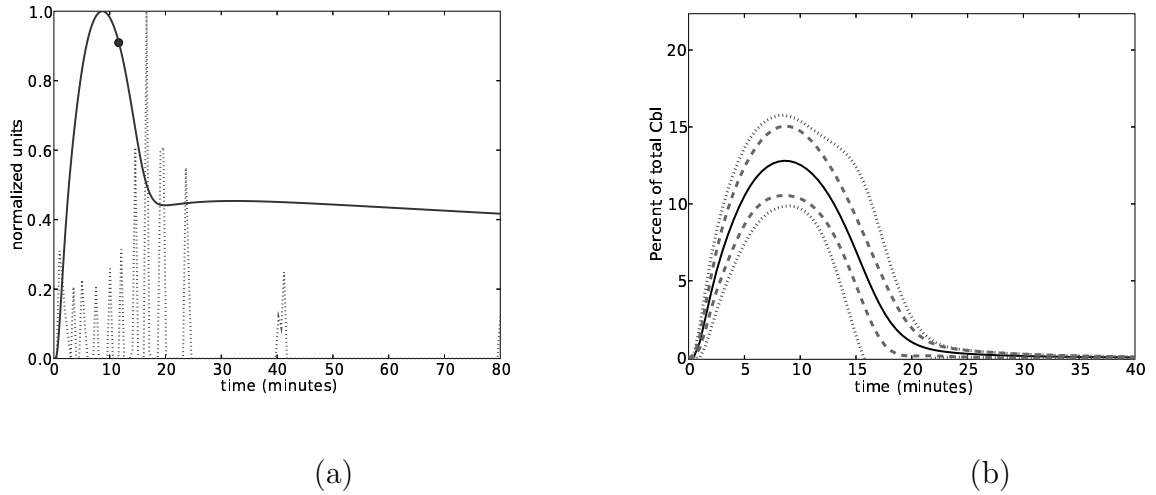


Figure 2.5: (a) Trajectory of total active Cdc42 (solid line) with single sequential design measurement (marked with a dot) and approximate continuous design weights (dotted line) to reduce the average variance of the prediction on the Cool-1, Cbl, Cdc42 complex. The weights are optimized over 160 uniformly spaced hypothetical measurements placed between 0 and 80 minutes on Cdc42. (b) Shows the reduction in the original uncertainty bounds resulting from the single measurement (dotted line) and the approximate continuous design measurement (dashed line) in (a). Compare with Fig. 2.4 before the addition of new measurements.

It is worth noting here that these extra measurements have little effect on the parameter uncertainty. In Fig. 2.6 on the left, we show the eigenvalues of the approximate covariance matrix  $M^{-1}$  both before and after the addition of the new data points. On the right is the square root of the diagonal elements of  $M^{-1}$ , giving the standard deviation in each parameter. As can be seen, the large parameter uncertainties are changed little after the addition of the optimal data points. In a sense, the underlying parameter uncertainty defined by  $M^{-1}$  in Eqn.

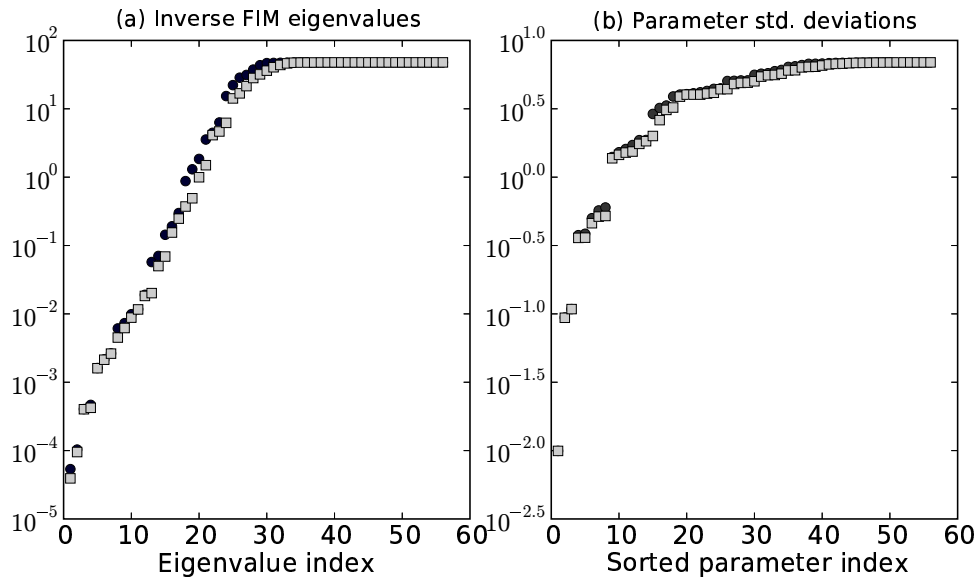
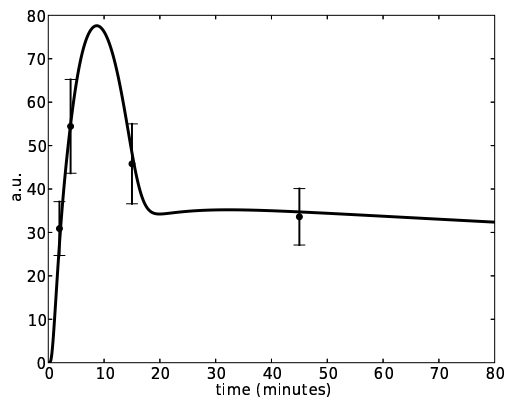


Figure 2.6: (a) Eigenvalues of the approximate parameter covariance matrix,  $M^{-1}$ , with (light squares) and without (dark circles) the optimally designed data to reduce the uncertainty of the triple complex trajectory. (b) Individual parameter standard deviations, sorted from smallest to biggest with (light squares) and without (dark circles) the optimally designed data. Note that the cutoff in the spectrum of eigenvalues is due to the prior information assumed on parameters ranges. Even with prior information, 40 of the 60 parameters have uncertainties corresponding to a greater than 20-fold increase or decrease in their non-logarithmic values.

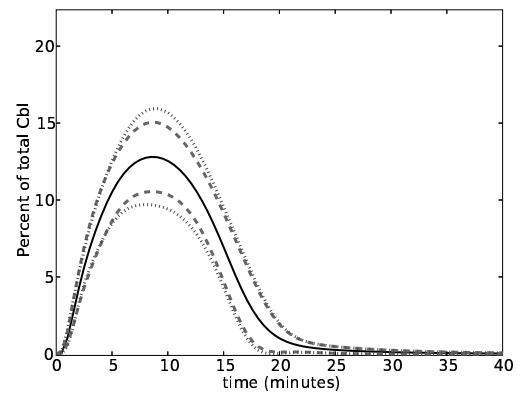
2.5, although large in some directions, is mostly aligned with directions where the model sensitivity is small. Conversely, if we include hypothetical measurements on the binding and unbinding constants involved in forming the triple complex, we find only a negligibly small decrease in the uncertainty in the prediction of the triple complex (see Appendix A.1). This is not so surprising when we understand that the uncertainty arises from the uncertainties in components of the system upstream of the triple complex; using parameter measurements alone, almost every rate constant in the system would have to be measured accurately to constrain the prediction [28].

### **New measurements on total active Cdc42**

Further measurements were made on total activated Cdc42 in the lab by Western blotting and with no refitting, our model was able to match the new data using a scale factor alone, see Fig. 2.7. (However, we cannot consider this as a validation of our model, since prior to the inclusion of the new data, the uncertainties on total activated Cdc42 were very large. Any experimental observations within the uncertainty bounds would be consistent with the model.) The uncertainties of the triple complex time course, given the real data and the optimally weighted data, is shown in Fig. 2.7 (b). Importantly, given that the measured activities of total Cdc42 were consistent with the trajectory for the optimized set of parameters, the reduction in uncertainty of the triple complex for the real data is comparable to that for the optimally selected data and we can make a firm conclusion that the triple complex does sequester significant amounts of the Cbl protein even in wild type cells after EGF stimulation. Therefore it appears that the complex plays a part under normal conditions in the EGFR homeostasis. (Note that if the new data



(a)



(b)

Figure 2.7: (a) Without refitting to the new total active Cdc42 data, our prediction matches the data using only a single multiplicative factor. a.u. = arbitrary units. (b) Reduced uncertainty on the time course of the active Cool, Cbl, and active Cdc42 complex for the optimal set of design points (dashed line) (same as Fig. 2.5 (b) ) and for the real data (dotted line).

collected showed a very different time course than in Fig. 2.7, an additional re-optimization step would need to be performed before we could assess the prediction and uncertainties for the triple complex.)

## 2.4 Discussion

We have demonstrated that by quantitatively modeling the dynamics of EGFR signaling and down-regulation in a mammalian cell line, we are led to incorporate interactions and modify existing reactions in order to reproduce the experimental observations. Note that these interactions are not directly tested by experiments, but we can infer them from the existing data. This refinement of an existing model of interactions and parameters is one important aspect of the modeling effort and gives insight into the underlying dynamics. Of course, we recognize that the model as it stands will only explain the behaviors observed in the data sets we have chosen. The addition of new experiments that test for receptor signaling from early endosomes [9], alternative endocytic mechanisms [66], autocrine signaling [64, 65] or the interactions between members of the erb-B family [32], for example, will require appropriate extensions of the mathematical model.

The second part of the process is to make predictions on the unmeasured or unmeasurable species of the system, assuming that the model has been suitably refined. We suggest that for testable predictions to be made, uncertainty estimates need to be attached to them [8]. In some cases the prediction uncertainties are rather small, despite large parameter uncertainty. On the other hand, if some predictions show large uncertainty, and involve species that are not directly measurable, we may then define a suitable design criterion and suggest new experimental

measurements that need to be taken to reduce that uncertainty. The results of such an analysis are promising, in that we find a rather small number of measurements (realistic to perform with standard molecular biology techniques) need be taken to begin to make predictions with good precision. Given such measurements on the EGFR system, we see that the triple complex of active Cocl-1, Cbl and active Cdc42 does indeed form in appreciable quantities in wild type cells and we also get an estimate for the time of formation and dissociation.

More generally, we believe that experimental design for reducing prediction uncertainties can play an important role in the iterative process of model refinement and validation and can be used in the testing of biological hypotheses.

## Chapter 3

# Variational method for estimating the rate of convergence of Markov Chain Monte Carlo algorithms<sup>1</sup>

We demonstrate the use of a variational method to determine a quantitative lower bound on the rate of convergence of Markov Chain Monte Carlo (MCMC) algorithms as a function of the target density and proposal density. The bound relies on approximating the second largest eigenvalue in the spectrum of the MCMC operator using a variational principle and the approach is applicable to problems with continuous state spaces. We apply the method to one dimensional examples with Gaussian and quartic target densities, and we contrast the performance of the basic Metropolis-Hastings algorithms with a “smart” variant that incorporates gradient information into the trial moves. We find that the variational method agrees quite

---

<sup>1</sup>As of this writing, this chapter is under review by *SIAM Journal of Scientific Computing* with the same title and authors F.P. Casey, J.J. Waterfall, R.N. Gutenkunst, C.R. Myers and J.P. Sethna

closely with numerical simulations. We also see that the smart MCMC algorithm often fails to converge geometrically in the tails of the target density except in the simplest case we examine, and even then care must be taken to choose the appropriate scaling of the deterministic and random parts of the proposed moves. We apply the same method to approximate the rate of convergence in multidimensional Gaussian problems with and without importance sampling. Thus we demonstrate the necessity of importance sampling for target densities which depend on variables with a wide range of scales.

### 3.1 Introduction

Markov Chain Monte Carlo (MCMC) methods are important tools in parametric modeling [25, 50] where the goal is to determine a posterior distribution of parameters given a particular dataset. With respect to the nonlinear biological model we discussed in Chap. 2, we may like to obtain uncertainty estimates for parameters or predictions that go beyond using the Fisher Information Matrix, which assumes linearization of the model about the best fit (shown in Chap. 2). The MCMC methods are used to produce a random sample of parameter sets that are weighted according to their costs, which measures the fit to the experimental data. Given this random sample, the covariance matrix for the parameters can be evaluated, and predictions on unmeasured species within the network can be made over all the parameter sets in the sample.

Since these algorithms tend to be computationally intensive, the challenge is to produce algorithms that have better convergence rates and are therefore more efficient [1, 3]. Of particular concern are situations where there is a large range of

scales associated with the target density, which we find is widespread in models from many different fields [8, 7, 23, 70, 28].

There are a number of techniques to either determine exactly or bound the convergence rate for MCMC algorithms on discrete state spaces [4], but there has been little discussion on finding quantitative eigenvalue bounds for continuous state spaces. Where work has been done in that area [60, 40], upper bounds on the convergence rate can be derived but the techniques are rather involved and the bounds may not be very useful. Therefore, in this work, we show that a conceptually straightforward variational method can provide convergence rate estimates for continuous state space applications. Even though we provide only lower bounds on the convergence rate we show these bounds can be remarkably tight. Furthermore, lower bounds allow us to discover conditions for which the MCMC method fails to converge.

We have been able to obtain explicit formulas for one dimensional example problems but the method may be more generally applicable, when applied in an approximate way, as we demonstrate for a multidimensional problem.

## 3.2 Markov Chain Monte Carlo

Typically, one wishes to obtain a sample  $x_1, x_2, \dots$  from a probability distribution  $\pi(x)$  which is sometimes called the *target* distribution. An MCMC algorithm works by creating a Markov chain that has  $\pi(x)$  as its stationary distribution, i.e. after many steps of the chain any initial distribution converges to  $\pi(x)$ . A sufficient condition to establish  $\pi(x)$  as the stationary distribution is that the chain be

ergodic and that the *transition density*,  $t(x, y)$ , of the chain satisfy detailed balance:

$$\pi(x)t(x, y) = \pi(y)t(y, x).$$

Given a *proposal density*  $q(x, y)$  for generating moves, one way to construct the required transition density [56, 48] is to define  $t(x, y) = \alpha(x, y)q(x, y)$  where

$$\alpha(x, y) = \min \left( \frac{q(y, x)\pi(y)}{q(x, y)\pi(x)}, 1 \right) \quad (3.1)$$

is the *acceptance probability* of the step  $x \rightarrow y$ . Obtaining the sample from the stationary distribution then involves letting the chain run past the transient (*burn-in*) time and taking uncorrelated samples from the late time trajectory. How long it takes to reach the stationary distribution determines the efficiency of the algorithm and for a given target distribution, clearly it depends on the choice of the proposal density. We can write down the one-step evolution of a probability density  $p(x)$  as a linear operator:

$$\begin{aligned} (\mathcal{L}p)(y) &= \int t(x, y)p(x) dx + \left( 1 - \int t(y, x) dx \right) p(y) \\ &= \int (t(x, y)p(x) - t(y, x)p(y)) dx + p(y) \end{aligned}$$

where  $dx = dx_1 \dots dx_n$ ,  $dy = dy_1 \dots dy_n$ ,  $n$  is the dimension of the state space and all integrals are from  $-\infty$  to  $\infty$  here and elsewhere in this manuscript. The second form makes it explicit that  $p(y) = \pi(y)$  is the stationary distribution by the detailed balance relation.

Now, if the linear operator has a discrete set of eigenfunctions and eigenvalues, it holds that the asymptotic convergence rate is determined by the second largest eigenvalue in absolute value (the largest being one) [44, 57]. We will write this eigenvalue as  $\lambda^*$ , and will refer to it as the *second eigenvalue* meaning the second largest in *absolute* value. Assuming geometric convergence of the chain [58], the

discrepancy between the density at the  $m^{\text{th}}$  iterate of the chain and the target density decreases as  $(\lambda^*)^m$  for large  $m$ . Therefore we would like  $\lambda^*$  to be as small as possible.

The variational calculation allows us to obtain an estimate for  $\lambda^*$ , but before we can do this we need to convert our operator into a self-adjoint form which ensures that the eigenfunctions are orthogonal. This is easily accomplished by a standard technique [4] of defining a new transition density by  $s(x, y) = t(x, y) \sqrt{\pi(x)}/\sqrt{\pi(y)}$  and our self-adjoint operator is then given by

$$(\mathcal{S}p)(y) = \int s(x, y)p(x) dx + \left(1 - \int t(y, x) dx\right) p(y) \quad (3.2)$$

$$= \int (s(x, y)p(x) - t(y, x)p(y)) dx + p(y) \quad (3.3)$$

where the “diagonal” part of the old operator (multiplying  $p(y)$ ) need not be transformed using  $s(x, y)$ . It is easy to show that defined as above,  $\mathcal{S}$  is self-adjoint. Note that if  $u(x)$  is an eigenfunction of the operator  $\mathcal{S}$ , then  $\sqrt{\pi(x)}u(x)$  is an eigenfunction of the original operator  $\mathcal{L}$  with the *same* eigenvalue.

### 3.2.1 Metropolis-Hastings and smart Monte Carlo

MCMC algorithms essentially differ only in the choice of proposal density and acceptance probability that is used in selecting steps. We will refer to the standard *Metropolis-Hastings* (MH) algorithm as that which uses a symmetric proposal density to determine the next move; for example, a Gaussian centred at the current point:

$q(x, y) = \sqrt{|L|/(2\pi)} \exp(-(y-x)^T L(y-x)/2)$  where  $L$  is an inverse covariance matrix that needs to be chosen appropriately for the given problem (*importance sampling*). In other words, the proposed move from  $x$  to  $y$  is given by  $y = x + R$

where  $R \sim \mathbf{N}(0, L^{-1})$  is a normal random variable, mean 0 and covariance  $L^{-1}$ . Thus the update on the current state is purely random. We will see that when the target density is not spherically symmetric, a naive implementation of the Metropolis-Hastings algorithm where the step scales are all chosen to be equal leads to very poor performance of the algorithm. As would be expected the convergence deteriorates as a function of the ratio of the true scales of the target density to the scale chosen for the proposal density.

One variant used to accelerate the standard algorithm is a *smart* Monte Carlo method [61] that uses the gradient of the negative of the log target density at every step,  $G(x) = -\nabla \log(\pi(x))$  to give

$$q(x, y) = \frac{\sqrt{|L|}}{\sqrt{2\pi}} \exp\left(-\frac{1}{2}(y - (x - H^{-1}G(x)))^T L (y - (x - H^{-1}G(x)))\right) \quad (3.4)$$

and  $H$  can be considered either as a constant scaling of the gradient part of the step or, if it is the Hessian of  $-\log(\pi(x))$ , as producing a Newton step. The move to  $y$  is generated as  $y = x - H^{-1}G(x) + R$ , so now we have a *random* component  $R \sim \mathbf{N}(0, L^{-1})$  and a *deterministic* component  $-H^{-1}G(x)$ . Viewed like this, moves can be considered to be steps in an optimization algorithm (moving to maximize the probability of the target density) with random noise added. We will see that with an optimal choice of  $H$  and for Gaussian target densities, the smart Monte Carlo method can converge in one step to the stationary distribution. We will also see that for a one dimensional non-Gaussian distribution it actually fails to converge geometrically, independent of the values of the scaling parameters.

### 3.2.2 Variational method

Once we have the self-adjoint operator for the chain,  $\mathcal{S}$  from Eqn. 3.3, and we know the eigenfunction with eigenvalue  $\lambda_1 = 1$ ,  $\sqrt{\pi(x)}$ , we can look for a candidate

second eigenfunction in the function space orthogonal to the first eigenfunction where the inner product is defined by  $(p_1, p_2) = \int p_1(x)p_2(x) dx$ . Given a family of normalized candidate functions in this space,  $v_a(x)$ , with variational parameter  $a$ , the variational principle [19, 44] states

$$\max_a |(v_a, \mathcal{S}v_a)| \leq \lambda^* \leq 1 \quad (3.5)$$

and depending on how accurately our family of candidate functions captures the true second eigenfunction, this can give quite a close approximation to the second dominant eigenvalue. In the problems we examine in the following sections the target densities have an even symmetry which makes it straightforward to select a variational trial function: any function with odd symmetry will naturally lie in the orthogonal space. For more complicated problems with known symmetries this general principle may be useful in selecting variational families for the purposes of algorithm comparison.

Writing out explicitly for  $\mathcal{S}$  in  $(v_a, \mathcal{S}v_a)$  we have

$$(v_a, \mathcal{S}v_a) = \int \int v_a(x)s(x, y)v_a(y) dx dy - \int \int t(y, x) (v_a(y))^2 dx dy + 1 \quad (3.6)$$

As we will see in the following section, the lower bound in Eqn. 3.5 can be arbitrarily close to 1 and therefore equality holds. In these situations we see the chain does not converge geometrically. We will also see that there can be eigenvalues in the spectrum that are close to  $-1$  which determine the asymptotic convergence rate, i.e.  $\lambda^* = |\lambda_n|$  where  $\lambda_n < 0$ . Interestingly, for this situation there is oscillatory behaviour of the Markov chain state space density.

## 3.3 Examples

### 3.3.1 Gaussian target density

Consider the simplest case of a one dimensional Gaussian target distribution  $\pi(x) = \sqrt{k/(2\pi)} \exp(-kx^2/2)$  with variance  $1/k$ . In a statistical mechanics description, this is the Boltzmann probability of a particle under a quadratic potential energy. Under the standard MH algorithm, the proposal density is

$$q(x, y) = \sqrt{\frac{l}{2\pi}} \exp\left(-\frac{1}{2}l(y-x)^2\right). \quad (3.7)$$

The issue is to determine  $l$  optimally; a first guess would be that  $l = k$  is the best choice. We will see that this is not actually correct.

To begin, define a variational function  $v_a(x) \propto x \exp(-ax^2/2)$ , orthogonal to the target density and normalized such that  $\int v_a^2 dx = 1$ . We can motivate this choice by recognizing that any initial distribution that is asymmetric will most likely have a component of this test function, and a convergence rate estimate based on it roughly corresponds to how fast probability “equilibrates” between the tails. (More commonly, variational calculations will use linear combinations of many basis functions with the coefficients as variational parameters. We find here that including higher order terms in the test function is unnecessary as we obtain tight enough bounds just retaining the lowest order term.)

We proceed by evaluating Eqn. 3.6 noting that because of the form of the acceptance probability, Eqn. 3.1, there are two functional forms for the kernels  $t(x, y)$  and  $s(x, y)$  delineated by the equation  $y^2 = x^2$ , i.e. whether the “energy” change,  $\Delta E(x, y) = -\log(\pi(y)) + \log(\pi(x)) = k(y^2 - x^2)/2$ , is positive or negative. (It is then convenient to define the coordinate change  $y = rx, x = x$  or  $x = ry, y = y$  where  $-1 \leq r \leq 1$  and  $-\infty \leq x, y \leq \infty$  to evaluate the integrals.) An explicit

expression for  $(v_a, \mathcal{S}v_a)$  can be obtained for this case of a Gaussian target density.

Next, we use a numerical optimization method to maximize the bound defined by Eqn. 3.5 with respect to  $a$ . The result of this analysis is shown in Fig. 3.1 along with an empirically determined convergence rate for comparison. (To obtain the rate empirically, we run the MCMC algorithm for many iterates on an initial distribution and observe the long time differences from the target distribution. These differences are either fit using Hermite polynomial functions or by looking for the multiplicative factor by which the density changes from one iterate to the next.) The variational bound tightly matches the asymptotic convergence rates in

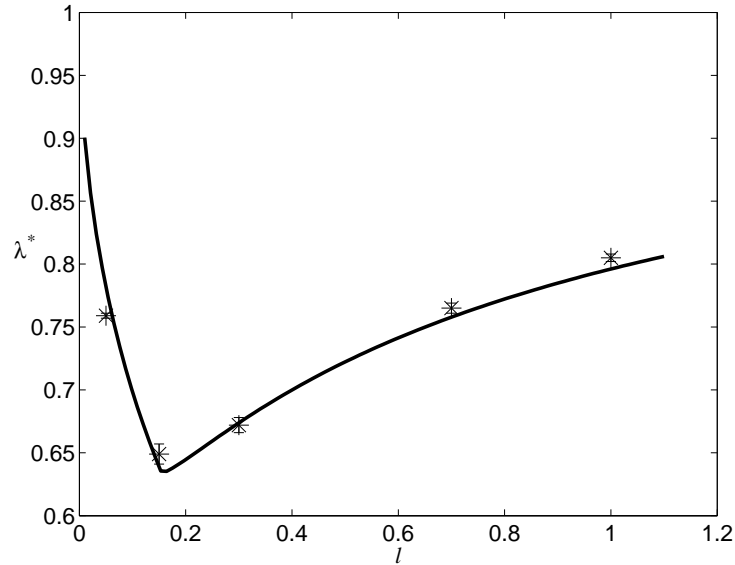


Figure 3.1: Variational estimate on the second eigenvalue for the one dimensional Gaussian problem using the standard MH method, with  $k = 1.0$ . The variational estimate is the solid line and the empirically determined values are marked with stars. Some of the empirical convergence rates seem to be less than the lower bound, but this is due to inaccuracies in their estimation

this case, and an optimum step size  $l$  can be ascertained. Clearly our  $l = 1$  initial

guess for the best scaling is far from optimal.

Moving to the one dimensional smart Monte Carlo, we have a Gaussian proposal density of the form :

$$q(x, y) = \sqrt{\frac{l}{2\pi}} \exp\left(-\frac{1}{2}l\left(y - \left(x - \frac{k}{h}x\right)\right)^2\right) \quad (3.8)$$

where  $1/l$  is the variance of the random part of the step and  $1/h$  is the scale of the deterministic part. (Letting  $h \rightarrow \infty$  we recover the standard MH algorithm of Eqn. 3.7.)

Taking  $h = k$  corresponds to performing a Newton step at every iterate of the algorithm. Thus, since the log of the target density is purely quadratic, the current point will always be returned to the extremum at 0 by the deterministic component of the smart Monte Carlo step and the random component will give a combined move drawn from  $q(x, y) = q(y) = \sqrt{l/(2\pi)} \exp(-ly^2/2)$ , which has the form of an *independence sampler* [56]. If we then also choose  $l = k$ , we see immediately that we are generating moves from the target distribution from the beginning, i.e. we have convergence in one step starting from *any* initial distribution.

In real problems, however,  $-\log(\pi(x))$  will not be quadratic. We may obtain an estimate for  $l$  and  $h$  by considering its quadratic approximation or curvature but in many cases those estimates will have to be adjusted. If the curvature is very small (or in multidimensional problems if the quadratic approximations are close to singular), the parameters will have to be increased to provide a step size control to prevent wildly unconstrained moves (analogous to the application of a trust region in optimization methods [14]). If the curvature is large but we believe that the target density is multimodal, we need to decrease the parameters to allow larger steps to escape the local extrema. Therefore we examine in the following the dependence of the convergence rate as we vary both of the parameters  $l$  and

$h$ .

The acceptance probability Eqn. 3.1 has two functional forms separated by a boundary in the  $(x, y)$  plane given by

$$\left(k + l \frac{k}{h} \left(-2 + \frac{k}{h}\right)\right) (y^2 - x^2) = b(k, h, l)(y^2 - x^2) = 0 . \quad (3.9)$$

In particular, the acceptance probability is

$$\alpha(x, y) = \min \left( \exp \left( -\frac{1}{2} b(k, h, l)(y^2 - x^2) \right), 1 \right) . \quad (3.10)$$

Now we have a complication over the standard MH method because depending on the sign of the coefficient function  $b(k, h, l)$  in Eqn. 3.9, we find that either  $\alpha(x, y) < 1$  on  $|y| \geq |x|$ ,  $\alpha(x, y) = 1$  on  $|y| < |x|$  or vice versa. This is shown in Fig. 3.2.

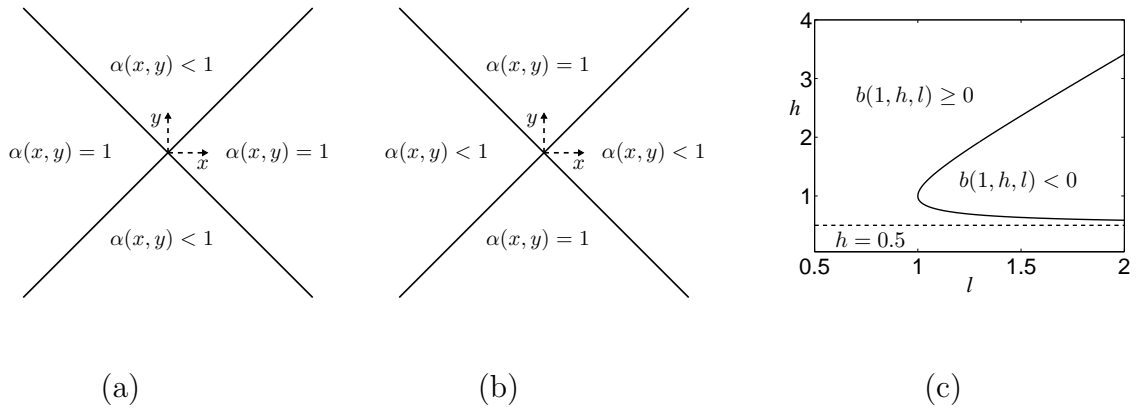


Figure 3.2: Regions in  $xy$  plane where acceptance probability  $\alpha(x, y) < 1$  or  $\alpha(x, y) = 1$ , when (a)  $b(1, h, l) \geq 0$  and (b)  $b(1, h, l) < 0$ . The equation for the boundary is shown in (c), see Eqn. 3.9 with  $k = 1.0$ . (The standard MH algorithm will only have regions described by (a). )

As before, for a given value of  $h$  and  $l$ , we need to break up the double integrals of the scalar product  $(v_a, \mathcal{S}v_a)$ , Eqn. 3.6, into the appropriate regions. Our choice

of variational function is the same as before (since the target density is the same) and we again can get an explicit (but complicated) expression for Eqn. 3.6 which we maximize with respect to  $a$ . The results of this analysis are shown in Fig. 3.3 (a), where we fix  $k = 1.0$  and vary  $h, l$ . We have confirmed that these lower bounds are quite accurate as shown in Fig. 3.3 (b).

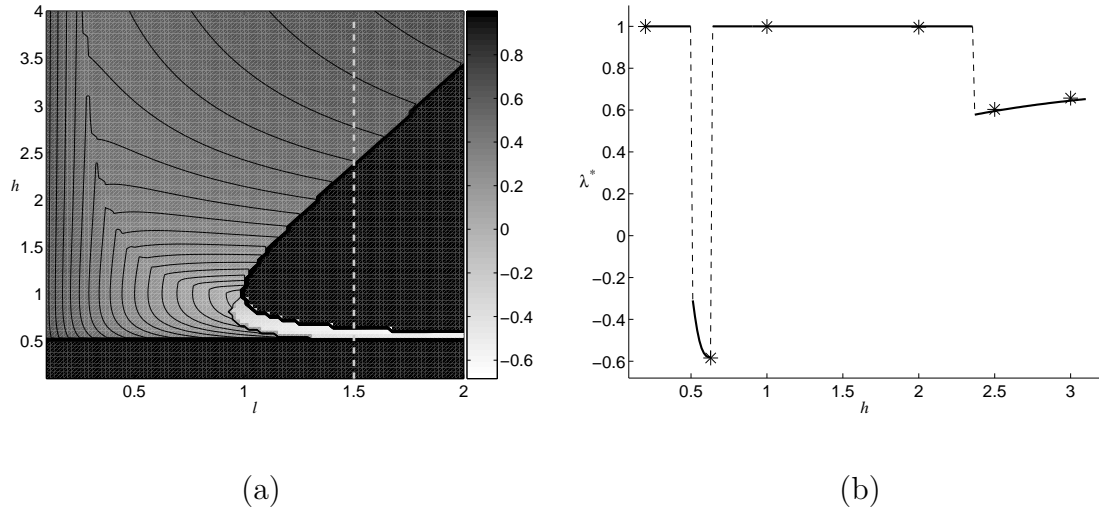


Figure 3.3: Estimate of second eigenvalue for the symmetrized smart Monte Carlo operator. (a)  $k = 1$  is fixed and  $h, l$  are allowed to vary. ( $h = 1.0, l = 1.0$  is the optimal scaling for deterministic and random parts of the step.) (b) We take a slice through this surface at  $l = 1.5$  and empirically determine the second eigenvalue at points along this curve (stars). The error bars are too small to be seen. Dashed lines are discontinuities.

The remarkable feature of these results is that even for this simple Gaussian problem, the selection of step scale parameters  $h, l$  is critical to achieve convergence. As already mentioned, there is a trivial choice of optimum with  $h = l = k = 1$  that gives one step convergence from any initial distribution (and therefore  $\lambda^* = 0$ ). However, if we change parameters infinitesimally such that

$l = 1 + \epsilon, h = 1$  ( $\epsilon > 0$ ) we go through a discontinuous transition where we see no convergence from *any* initial distribution. This can be understood by recognizing that after one step we will have a proposal density (before accept/reject)  $\propto \exp(-(1 + \epsilon)x^2/2)$  which has a factor  $\exp(-\epsilon x^2/2)$  less probability in its tails than the target density. Suppose there is an initial distribution or point mass concentrated at  $x = 20/\sqrt{\epsilon}$ . The proposed step of the smart Monte Carlo algorithm, starting at  $x$ , will revisit  $x$  too infrequently by a factor  $\exp(-100)$ . Thus detailed balance will force the transition  $x \rightarrow 0$  to be accepted with a probability of only  $\exp(-100)$ , and thus the initial distribution will take an exponentially long time to converge to the target density.

In fact this is one of the two disconnected regions where no geometric convergence is observed in Fig. 3.3. The largest of the two (with  $h > 1/2$ ) is defined exactly by the equation  $b(1, h, l) < 0$  (compare Fig. 3.2 (c) with Fig. 3.3 (a)). In this region the bound on the second eigenvalue approaches 1 as the variational parameter,  $a \rightarrow 0$ . This corresponds to a perturbation on the target density of  $x\sqrt{\pi(x)}$  for the unsymmetrized MCMC operator  $\mathcal{L}$ . In other words, we have a test distribution that has exponentially more probability in its tails than the target density. For initial states  $x$  arbitrarily far away from the origin, the acceptance probability  $\alpha(x, y)$  in the region  $|y| < |x|$  is arbitrarily small. To see this, note that Eqn. 3.10 is an exponentially decaying function of  $y^2 - x^2$  in this region, and given the form of the proposal density Eqn. 3.8, we see that the expected value of  $y^2 - x^2$  is arbitrarily large and negative. Thus states far out will never be “allowed back” and the fat tails of  $\sqrt{\pi(x)}$  will never shrink back down those of  $\pi(x)$ . Furthermore, moves  $x \rightarrow y$  where  $|y| \geq |x|$  are always accepted (because  $\alpha(x, y) = 1$  on  $|y| > |x|$ ) which simultaneously prevents convergence. The situation is analogous

to that described for  $l = 1 + \epsilon$  and  $h = k = 1$ , except now there is a cutoff both on the deterministic step and the random step. A typical example of this is shown in Fig. 3.4. Once we cross to the  $b(1, h, l) \geq 0$  region, moves  $x \rightarrow y$  where  $|y| < |x|$  are always accepted by Eqn. 3.10 (Fig. 3.2 (a)). Therefore excess probability in the tails is allowed to flow back into the central part of the distribution and the convergence is not blocked.

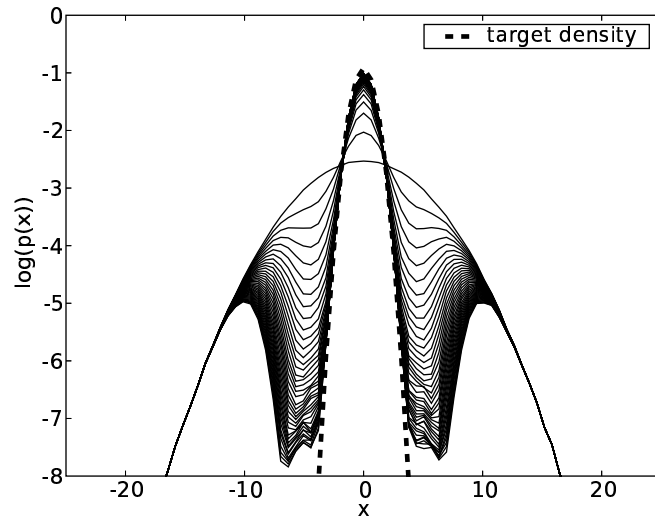


Figure 3.4: Forty iterates of the smart Monte Carlo algorithm (solid lines), Eqn. 3.8, when the initial distribution is normal with standard deviation five times the Gaussian target density (dashed line). Parameters are chosen to be in the region of no convergence ( $h = 2.0$ ,  $l = 1.5$ ), see Fig. 3.3 (a). We see that the tails of the initial distribution are essentially unchanging after many iterates and have failed to converge to the target density

In the second region where no convergence is observed, ( $h < 1/2$  in Fig. 3.3), we have a situation where the deterministic step alone (taking  $l \rightarrow \infty$ ) leads to the proposed moves being generated by an unstable mapping, from the  $(n-1)^{th}$  to  $n^{th}$

iterate:  $x^{(n)} = x^{(n-1)} - \beta x^{(n-1)}$  where  $\beta > 2$ . The trial variational function for this situation also maximizes the bound as  $a \rightarrow 0$ , again implying that the tails are not decaying to the stationary distribution. The reason is that, even when  $l < \infty$ , we have a situation in which the *expected* or mean position of a state  $x$  after one step is  $y$  where  $|y| \geq |x|$ . Thus excessive probability in the tails cannot be shifted inward to match the target density.

The  $h = 1/2$  “trough” is a special case where we have oscillatory behaviour. That is, the second eigenvalue is negative but greater than  $-1$  and in fact convergence does occur. Interestingly setting  $h = k/2$  means that  $b(k, h, l) = k$  and the acceptance probability of Eqn. 3.10 looks again like that of the standard MH algorithm, but the convergence is actually faster. In a sense, given that the deterministic part of the step moves  $x \rightarrow -x$  and the target distribution is symmetric, the oscillatory behavior allows the chain to sample the distribution twice as fast.

### 3.3.2 Quartic target density

In scientific or statistical applications where MCMC is used, the log of the target density will ordinarily have higher order terms beyond the quadratic order we studied in the previous section. For example, in a Bayesian inference problem the posterior distribution will rarely have a simple Gaussian form. Both finding the maximum *a posteriori* parameter estimates and sampling from the posterior are made more difficult in the presence of these higher order terms.

Therefore, we wish to extend the previous example by studying a target distribution of the form  $\pi(x) = 2^{(3/4)}k^{(1/4)}/\Gamma(1/4) \exp(-kx^4/2)$  Here, the log of the target density is quartic (so this describes the Boltzmann probability of a particle in a quartic potential) and the proposal density (Gaussian) no longer has the same

form as the target density. We would like to understand the performance of the Monte Carlo algorithms in this circumstance. (The test distribution is taken to be  $\propto x \exp(-ax^4/2)$ , i.e. in the orthogonal space to the stationary distribution).

The goal is to estimate the optimal value of  $l$ , as before. We can argue approximately that the step scale should be such that  $kx^4/2 \approx 1$  for a typically move  $x$ , i.e. the change in energy is about 1 and the acceptance probability is therefore  $\exp(-1)$ . This gives a typical value for  $x^2 = \sqrt{2}/\sqrt{k}$ . Since the proposal density is Gaussian with variance  $1/l$ , we therefore would naively predict  $l = \sqrt{k}/\sqrt{2}$ . Applying the variational method, we were unable to find a closed form solution to Eqn. 3.6 so we had to resort to numerical integrals in determining the bound in Eqn. 3.5. The results are shown in Fig. 3.5 for the standard MH method; it suggests an optimal choice for the step size parameter,  $l$ , which is an improvement over our initial guess of  $1/\sqrt{2}$  (when  $k = 1$ ).

Turning to the smart Monte Carlo algorithm, if we wish to make the deterministic part of the proposed move a Newton step using the Hessian of  $-\log(\pi(x))$  at  $x = 0$  we are left with a singular Hessian and an infinite deterministic step, reinforcing the need for the step length control parameter,  $h$ .

Surprisingly, we find that, *independent* of the value of  $h$  and  $l$ , ( $k$  fixed at 1), the scalar product  $(v_a, \mathcal{S}v_a) \rightarrow 1$  as  $a \rightarrow 0$ . Thus there are no choices of scaling parameters which will lead to convergence. This is borne out by numerical simulation, see Fig. 3.6 for the changes in an initial density under many iterates of the algorithm with an arbitrary choice for  $s$ ,  $h$ .

The failure of the smart Monte Carlo method for the quartic problem is clearly due to non-convergence of the tails of the distribution, and can be seen by analyzing the integrals defining the operator, Eqn. 3.6, and noting that they all tend to zero

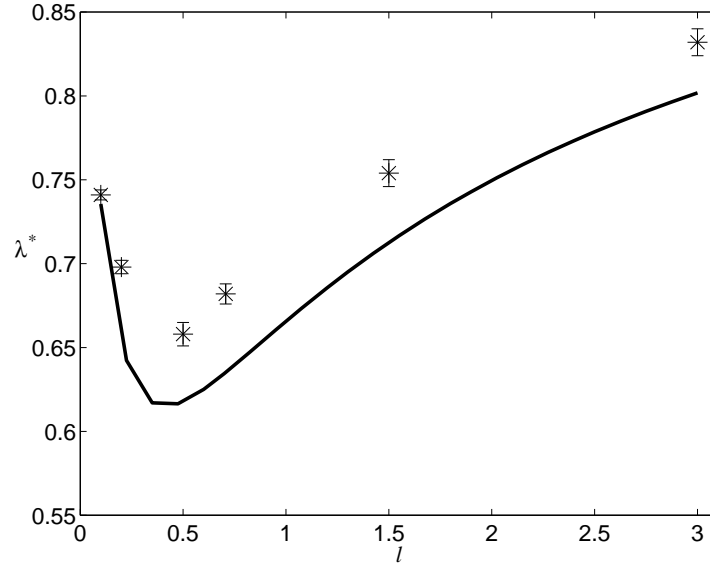


Figure 3.5: Second eigenvalue estimate from the variational method (solid line) and data points (stars), for the quartic target density ( $k = 1$ ) using the standard MH method, Eqn. 3.7. The numerical values for  $\lambda^*$  are now estimated by taking the ratio of the discrepancy from the target density in subsequent iterates and finding a single multiplicative factor which describes the decay. This is done rather than using functional forms analogous to Hermite polynomials to fit the decay, because it appears that there may be more significant contributions from higher order terms. This also explains why the lower bound shown differs more than in Fig. 3.1 and Fig. 3.3 (b). The data point shown at  $1/\sqrt{2} \approx .71$  (see text) does not appear to be optimal.

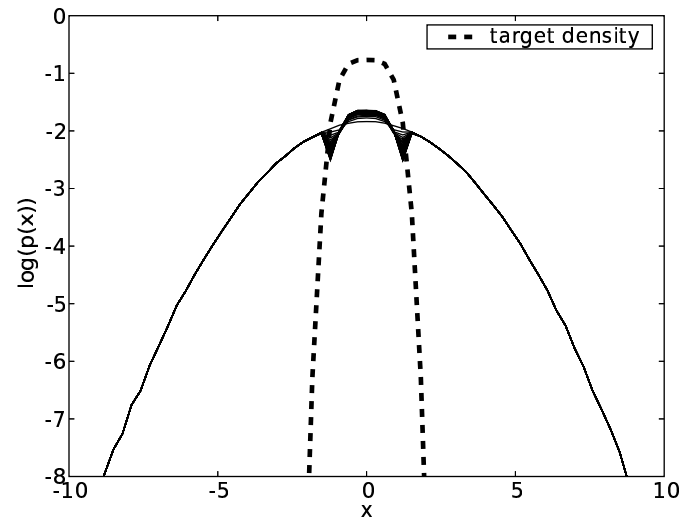


Figure 3.6: Forty iterates of the smart Monte Carlo algorithm (solid lines), Eqn. 3.8, when the target density is quartic (dashed line). The initial distribution of points is normal with standard deviation about five times that of target density (dashed line). Parameters are arbitrarily chosen as  $(h = 1.0, l = 1.0)$ , and we see that the tails of the initial distribution are unchanged for every iterate of the algorithm. Other parameter sets tested lead to the same behaviour.

as the variational parameter tends to zero, independent of the choice for  $k$ ,  $h$  and  $l$ .

The quartic problem is a representative example containing higher order terms beyond quadratic in the log of the target density. Almost all real world applications [34, 42, 37, 52] will involve higher order nonlinearities and users of smart Monte Carlo should be warned that their algorithm may not provide accurate sampling in a reasonable time-scale in the tails of the distribution. (While the algorithm can be shown to converge to the equilibrium distribution, this formal convergence is useless if the convergence is not geometrical but logarithmic.) In applications where the convergence of the smart Monte Carlo method has been tested the convergence criteria have perhaps been insensitive to convergence in the tails of the distribution.

### 3.4 Multidimensional target densities

For multidimensional problems, it is quite common that there is a large range of scales associated with the target density [8, 28, 70]. That is, the curvature of the probability density along some directions in the parameter space is much larger than in other directions. Clearly, if an MCMC method is not designed to take these different scales into account through importance sampling, the algorithm will perform very poorly. If the curvature is very high in a particular direction and we try to take a moderately sized step, it will almost certainly be rejected but if we take small steps in directions that are essentially flat the MCMC algorithm will be very slow to equilibrate. We would like to show explicitly here what happens to the convergence rate when the scale of the problem has been underestimated or

overestimated.

The variational calculations for the one dimensional examples of the previous section either yielded explicit formulas or gave integrals that were relatively fast to compute numerically. However as we go to multiple dimensions neither of these features are present, in general. Typically the integrals describing  $(v_a, \mathcal{S}v_a)$  will *not* factor into one dimensional integrals. For Gaussian target densities the full space is broken into regions analogous to those in Fig. 3.2, described by an equation like  $y^t A y \geq x^t A x$  where  $A$  is a symmetric  $n$  by  $n$  matrix which is not necessarily positive definite. For the standard MH algorithm applied to a multivariate Gaussian target density with inverse covariance matrix  $K$ , we have  $A = K$ , and therefore all the dimensions are coupled through the energy change,  $\Delta E = y^t K y - x^t K x$ . We would still like to be able to get a lower bound on  $\lambda^*$ , and to this end note that *any* test function orthogonal to the target density will work in Eqn. 3.5; we do not explicitly need to introduce a variational parameter. It is still necessary to make choices that are both tractable in computing  $(v, \mathcal{S}v)$  and are “difficult” functions for the given algorithm to converge from.

As an example, take the multivariate Gaussian distribution of the form

$$\pi(x) = \frac{\sqrt{|K|}}{(2\pi)^{\frac{n}{2}}} \exp\left(-\frac{1}{2}x^t K x\right) \quad (3.11)$$

with  $x = (x_1, \dots, x_n)$ , and consider using the MH algorithm with importance sampling, i.e.

$$q(x, y) = \frac{\sqrt{|L|}}{(2\pi)^{\frac{n}{2}}} \exp\left(-\frac{1}{2}(y - x)^t L (y - x)\right)$$

where again  $L$  is the inverse covariance matrix/step size control term and to simplify we assume that both  $K$  and  $L$  are diagonal. Without any analysis we might guess that the optimum choice for  $L$  is  $K$ .

First we construct a test function that will provide a useful bound when the proposed steps are too large for the natural scale of the problem. For simplicity, consider putting a delta function distribution at the origin. If we take large steps the acceptance probability should be low and there will be a large overlap between the initial state and the final state. In the limit that the proposed steps have infinite length, the initial state will not be changed at all and the bound on the second eigenvalue will approach one. To do this more carefully we define a test function which is a Gaussian whose variance will ultimately be taken to zero to represent the delta function. However, we also need to add another term to ensure the test function is orthogonal to the target density, in order to apply the variational bound. Therefore, for the unsymmetric operator we write the test function as :  $u_\sigma(x) = -A\pi(x) + Bw_\sigma(x)$  where  $w_\sigma(x)$  is the probability density for a multivariate Gaussian with covariance matrix  $\sigma^2 I$  and  $A$  and  $B$  are constants. For the symmetrized operator the trial function is transformed to  $v_\sigma(x) = -A\sqrt{\pi(x)} + Bw_\sigma(x)/\sqrt{\pi(x)}$ .  $A$  and  $B$  are constrained to satisfy the orthogonality relation  $(v_\sigma, \pi) = 0$  and a normalization  $(v_\sigma, v_\sigma) = 1$ . These lead to the conditions

$$A = B \quad \text{and} \quad B^2 \int \left( \frac{w_\sigma(x)}{\sqrt{\pi(x)}} \right)^2 dx = 1 + B^2 .$$

Then it can be seen that

$$(v_\sigma, \mathcal{S}v_\sigma) = -B^2 + B^2 \left( \mathcal{S} \frac{w_\sigma(x)}{\sqrt{\pi(x)}}, \frac{w_\sigma(x)}{\sqrt{\pi(x)}} \right)$$

where we have used the orthogonality condition, the fact that  $w_\sigma(x)$  integrates to

1 and that  $\mathcal{S}$  is self-adjoint. Writing out the operator  $\mathcal{S}$  explicitly we get

$$\begin{aligned} \left( \mathcal{S} \frac{w_\sigma(x)}{\sqrt{\pi(x)}}, \frac{w_\sigma(x)}{\sqrt{\pi(x)}} \right) &= \int \int \frac{w_\sigma(x)}{\sqrt{\pi(x)}} s(x, y) \frac{w_\sigma(y)}{\sqrt{\pi(y)}} dx dy - \\ &\int \int t(x, y) \left( \frac{w_\sigma(x)}{\sqrt{\pi(x)}} \right)^2 dx dy + \int \left( \frac{w_\sigma(x)}{\sqrt{\pi(x)}} \right)^2 dx . \end{aligned}$$

The last term on the right hand side is  $(1+B^2)/B^2$ , making use of the normalization condition, so we are left with

$$(v_\sigma, \mathcal{S}v_\sigma) = B^2 \int \int \frac{w_\sigma(x)}{\sqrt{\pi(x)}} s(x, y) \frac{w_\sigma(y)}{\sqrt{\pi(y)}} dx dy - B^2 \int \int t(x, y) \left( \frac{w_\sigma(x)}{\sqrt{\pi(x)}} \right)^2 dx dy + 1 .$$

Since we are ultimately taking a limit as  $\sigma \rightarrow 0$  ( $w_\sigma \rightarrow$  a delta function) we can make approximations to these integrals as follows :

$$\int \int \frac{w_\sigma(x)}{\sqrt{\pi(x)}} s(x, y) \frac{w_\sigma(y)}{\sqrt{\pi(y)}} dx dy \approx s(0, 0) \int \int \frac{w_\sigma(x)}{\sqrt{\pi(x)}} \frac{w_\sigma(y)}{\sqrt{\pi(y)}} dx dy$$

and

$$\int \int t(x, y) \left( \frac{w_\sigma(x)}{\sqrt{\pi(x)}} \right)^2 dx dy \approx \int t(0, y) dy \int \left( \frac{w_\sigma(x)}{\sqrt{\pi(x)}} \right)^2 dx .$$

Finally by taking  $\sigma \rightarrow 0$  we have the expression

$$(\mathcal{S}v_0, v_0) = 1 - \int t(0, y) dy .$$

As already mentioned, for the multidimensional problem we expect different functional forms for the kernels  $s(x, y)$  and  $t(x, y)$  depending on the initial and final state  $(x, y)$  and this is what makes decoupling the integrals difficult. However for this choice of test function the equation for the boundary (with  $x = 0$ ) is given by  $y^t K y = 0$  and since  $K$  is positive semidefinite we always stay on one side of the boundary (the energy never decreases from the initial distribution placed at  $x = 0$ ). Then

$$(\mathcal{S}v_0, v_0) = 1 - \frac{\sqrt{|L|}}{(2\pi)^{\frac{n}{2}}} \int \exp\left(-\frac{1}{2}y^t(K+L)y\right) dy \quad (3.12)$$

$$= 1 - \prod_{i=1}^n \sqrt{\frac{l_i}{l_i + k_i}} . \quad (3.13)$$

where  $l_i$  and  $k_i$  are the diagonal elements of the diagonal matrices  $L$  and  $K$ , respectively. With no importance sampling we would have  $L = kI$  where  $k$  would be chosen to make sufficiently large steps to enable it to sample  $\pi(x)$ . A rough argument as follows can give some insight into the form of Eqn. 3.13 :  $1/\sqrt{l_i}$  is a measure of the scale in the  $i^{\text{th}}$  coordinate direction of the proposal density,  $1/\sqrt{k_i}$  is the scale in the  $i^{\text{th}}$  coordinate direction of the target density. Suppose that  $l_i \ll k_i$  for each  $i$ , that is the scales of the proposal density are too large in all directions. Then the ratio of the mean volume of moves generated by  $q(0, y)$  to the volume occupied by  $\pi(y)$  is exactly  $\prod_{i=1}^n \sqrt{l_i}/\sqrt{k_i}$ . Intuitively, this ratio is proportional to the acceptance probability, and in the regime  $l_i \ll k_i$  the acceptance probability determines the convergence properties.

We want to use Eqn. 3.13 to show how choosing step sizes *too large* even in one direction will result in a very inefficient algorithm. Suppose that for all but one of the directions we make  $l_i = k_i, i = 1, \dots, n - 1$  which would be roughly the correct scaling in those directions. Then the bound on the second eigenvalue is

$$(\mathcal{S}v_0, v_0) = 1 - \sqrt{\left(\frac{1}{2}\right)^{n-1} \sqrt{\frac{1}{1 + k_n/l_n}}} . \quad (3.14)$$

From this we can see that as we go to larger and larger step sizes relative to the scale in the last direction ( $k_n/l_n \rightarrow \infty$ ), the bound on  $\lambda^*$  increases to 1. Conversely we can argue that if one of the directions of the target density has a scale that is considerably smaller than the step scales being used in the proposal density, we will get very few acceptances and the convergence rate will be close to 0. Hence we see explicitly the need for importance sampling to accelerate convergence.

We would also like to address what happens in the other limit as the step size becomes excessively small compared to the natural scale of the problem. (In fact Eqn. 3.13 gives a lower bound of zero in that case which is not surprising as it is

based essentially on the term in the operator equation which gives the probability of *staying* at the current state. If we take infinitesimally small steps, the acceptance probability will be one and we will never stay at the current state). When the step scales are infinitesimally small we expect intuitively that the bound on the second eigenvalue will also approach one; even though the acceptance ratio is close to one, very small steps will never be able to “explore” the target distribution sufficiently. To compute this limit, we propose a test function which has components of the target density in all directions except the last, where it has an antisymmetric form to make sure it is orthogonal to the target density. With respect to the symmetrized operator  $\mathcal{S}$  this means

$$v(x) \propto x_n \prod_{i=1}^n \sqrt{\pi_i(x_i)} . \quad (3.15)$$

Here  $\sqrt{\pi_i(x_i)}$  is the one dimensional Gaussian density which is the  $i^{\text{th}}$  factor in a diagonalized multivariate Gaussian density. We still have the problem of decoupling the  $n$ -dimensional multivariate problem into  $n$  one dimensional problems. To manage this we use a device to re-express the operator equation, Eqn. 3.6, explicitly in terms of the change  $\frac{1}{2}(y^t K y - x^t K x)$ . (i.e.  $-\log \frac{\pi(y)}{\pi(x)}$ ), which we denote by  $\Delta E$ . That is

$$\begin{aligned} (v, \mathcal{S}v) &= \int \int v(x) s(x, y) v(y) dx dy - \int \int t(x, y) (v(x))^2 dx dy + 1 \\ &= \int \int x_n \pi(x) q(x, y) \left( \int \min(e^{-\Delta E}, 1) \delta \left( \Delta E - \frac{1}{2} \sum_{i=1}^n k_i (y_i^2 - x_i^2) \right) d\Delta E \right) - \\ &\quad x_n^2 \pi(x) q(x, y) \left( \int \min(e^{-\Delta E}, 1) \delta \left( \Delta E - \frac{1}{2} \sum_{i=1}^n k_i (y_i^2 - x_i^2) \right) d\Delta E \right) dx dy \end{aligned}$$

Then we use the integral representation of the delta function

$$\delta(x) = \frac{1}{2\pi} \int \exp(-iwx) dw, \text{ factor } q(x, y) = \prod_{i=1}^n q_i(x_i, y_i), \text{ and rearrange the order}$$

of integration to give :

$$(v, \mathcal{S}v) = \frac{1}{2\pi} \int \min(e^{-\Delta E}, 1) \left( \int A(w) e^{-iw\Delta E} dw \right) d\Delta E \quad (3.16)$$

where  $A(w)$  contains the integration over the now decoupled  $(x, y)$  coordinates :

$$A(w) = \left( \prod_{i=1}^{n-1} \int \int \pi_i(x_i) q_i(x_i, y_i) e^{\frac{1}{2}iwk_i(y_i^2 - x_i^2)} dx_i dy_i \right) \times \quad (3.17)$$

$$\int \int (x_n y_n - x_n^2) \pi_n(x_n) q_n(x_n, y_n) e^{\frac{1}{2}iwk_n(y_n^2 - x_n^2)} dx_n dy_n \quad (3.18)$$

$$= \prod_{i=1}^{n-1} \frac{1}{\left(1 + \frac{k_i}{l_i} w(-i + w)\right)^{\frac{1}{2}}} \frac{i \frac{k_n}{l_n} w}{\left(1 + \frac{k_n}{l_n} w(-i + w)\right)^{\frac{3}{2}}} \quad (3.19)$$

Note that the complex integral with respect to  $dw$  has a branch point at the roots of  $\left(1 + \frac{k_n}{l_n} w(-i + w)\right)^{\frac{3}{2}}$  which lie on the imaginary axis at  $r_1$  and  $r_2$ . It simplifies the analysis to consider the situation  $k_i = l_i$  for  $i = 1, \dots, (n-1)$  and assume that  $n-1$  is even. This way, the roots of  $\left(1 + w(-i + w)\right)^{\frac{n-1}{2}}$ ,  $r_{1,0}$  and  $r_{2,0}$ , are  $(n-1)/2$  order poles and not branch points, also on the imaginary axis. If we now also assume that  $k_n < s_n$ , then we can take a contour as shown in Fig. 3.7 when  $\Delta E < 0$  and a similar one in the lower imaginary plane when  $\Delta E > 0$ . Thus Eqn. 3.19 is reduced to a residue term and a real integral which needs to be evaluated numerically. The result is plotted for  $n = 11$  in Fig. 3.8 along with the bound that came from Eqn. 3.14. Thus we see the trade off between taking large steps that potentially can explore the space quickly but have a higher chance of being rejected and taking small steps which will have a high acceptance probability but will be unable to sample the space quickly. As we saw when doing the full variational calculation for the one dimensional problems, the best step scale to use is not what we may have guessed; the natural choice  $l_n = k_n = 1$  here does not appear to minimize the second eigenvalue. We believe this kind of ‘‘approximate’’ variational approach may be a useful way to deal with problems which are difficult

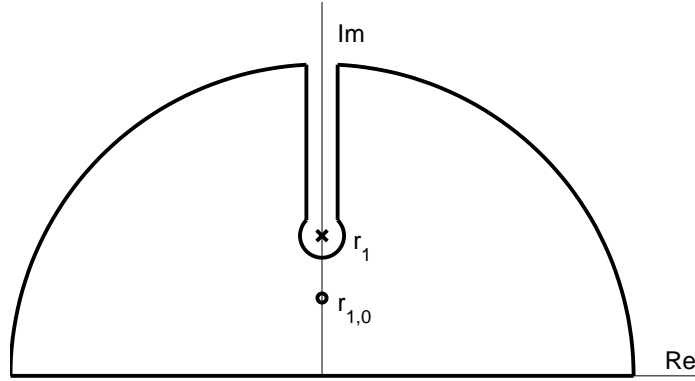


Figure 3.7: Contour used to evaluate Eqn. 3.19 when  $\Delta E < 0$ .  $r_1$  is a branch point and  $r_{1,0}$  is a pole of order  $(n - 1)/2$ . The contour is the same for  $\Delta E < 0$  except restricted to the negative imaginary plane.

to analyze otherwise.

### 3.5 Conclusion

By applying a variational method, it is possible to obtain an accurate (lower bound) estimate for the second eigenvalue of an MCMC operator and thus the asymptotic convergence rate of the chain to the target distribution. Given such an estimate we can optimally tune the parameters in the proposal distribution to improve the performance of the algorithm. The procedure has a role to play between the various numerical algorithms that perform convergence diagnostics before the full simulations are run, to allow the user to manually tune parameters, and the adaptive schemes [24, 1] that require no preliminary exploration.

In addition, the variational method allows us to discover weaknesses in variants of the basic Metropolis-Hastings algorithm which on the surface appear to be reasonable prescriptions for sampling the target density. This is most dramati-

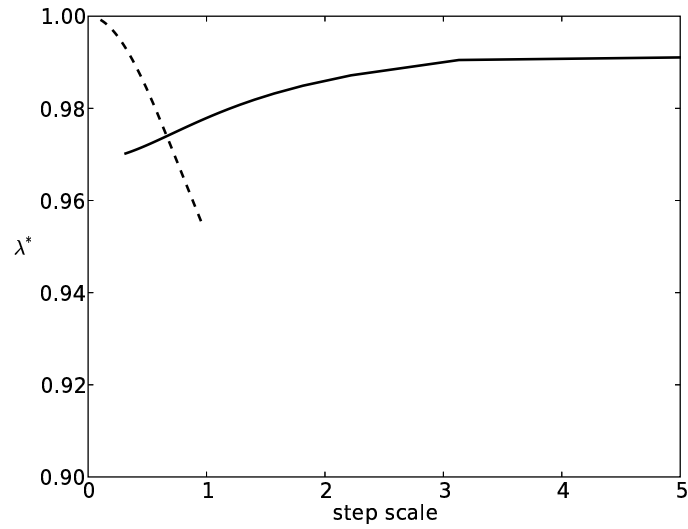


Figure 3.8: Lower bound on second eigenvalue for the multivariate Gaussian problem, Eqn. 3.11, with  $n = 11$ . Step scale =  $\sqrt{1/l_n}$ .  $k_n = 1$  sets the scale of the target density in the last direction. The test function is chosen as the negative of the target density perturbed by a delta function (solid line) or as the target density itself in all directions but the last (dashed line). The estimate for the lower bound is a maximum of the two curves.

cally seen in the smart Monte Carlo method discussed above which apparently has serious flaws for even the simplest of one dimensional target densities. Although the smart MC method has been widely used in molecular dynamics [34, 42, 37] and quantum Monte-Carlo [52], the scales are often chosen by physical considerations (for example, to not exceed significantly the step sizes needed to accurately describe the dynamical evolution of the system) and furthermore, the diagnostics of convergence are not as rigorous as ours; typically a physical quantity is monitored till it appears to reach an equilibrium value. Perhaps the rare events which correspond to the tails of the target distribution are of lesser importance in those studies, but users should be warned that convergence may be logarithmically slow in potentially interesting regions.

It would be interesting to apply the same technique to the more broadly used gradient based hybrid MC algorithms [17] and other non-adaptive accelerated methods (e.g. parallel tempering [18]). More generally, the variational analysis could be a useful tool in making comparisons between the convergence properties of the latest MCMC algorithms without extensive numerical simulation.

# Chapter 4

## Averaging for fast stochastic perturbations of differential equations <sup>1</sup>

### 4.1 Introduction

In modeling signaling networks and other cellular processes, differential equations are the most commonly used framework for describing the protein-protein or even protein-DNA interactions. There is a host of numerical methods for their solution and they are fast at tracking the dynamics of a large number of different species. However, it has been recognized that to accurately describe the reaction events at a molecular level, one needs to simulate the system stochastically [47]. In cases that some species in the system only exist in low numbers in a single cell, the deterministic and stochastic trajectories will be very different. In fact experimental

---

<sup>1</sup>This chapter is an outgrowth of work by Colin Hill and James Sethna, which built on earlier work with Jeff Tomasi.

observations [46] in bacteria suggest that stochastic dynamics play an important part of deciding single cell fate.

However, in a typical cell biology experiment to measure relative protein level or activity, for example, only the *average* of the stochastic trajectories will be measured since large numbers of cells need to be lysed to provide a good signal to noise ratio. Interestingly, the average of the stochastic trajectories can also differ from the deterministic dynamics, but can be described by a modified set of differential equations even when the noise amplitude is large, in some limits.

There are two main categories of approximations that can be made on the stochastic equations describing the evolution of the joint probability density of the species in the system: a time scale separation approximation and a large system size approximation.

The large system size approximation assumes that the stochastic sample path can be well described by a mean trajectory with a Gaussian noise component that has a small standard deviation compared to the mean. Under that assumption, an effective set of differential equations can be derived for the evolution of the mean and the covariances, by systematic expansion of the master equation [69]. The equations for the mean will have correction terms involving the covariances.

The time scale separation approximation, applied to the stochastic description of the system, involves partitioning reactions into fast and slow subsets [10, 11] or partitioning the species in the system into fast and slow subsets [54] in a chemical master equation framework. The assumption is then made that in between two slow reactions in the system, many fast reactions will fire. Equivalently, it is assumed that the time-dependent joint probability density describing the dynamics of the fast reactions or species will come to equilibrium instantaneously between

slow reaction events. Thus it is a stochastic version of the quasi-steady state approximation in deterministic dynamics. The fast species and reactions in the system can then be factored out and we are left with a reduced system involving the (corrected) dynamics for the slow species. The methods currently available based on the master equation deal only with the asymptotic limit (as the ratio of time scales becomes infinite), and do not attempt to make first order corrections.

The approach we take here is to take the infinite system size limit for some components of the system while simultaneously looking for corrections to the fast time scale limit for the other components. In other words we have species that are in very large numbers, but are slow, and species that are in small numbers, but participate in fast reactions. In that case we can start with a mixed deterministic/stochastic description of the system (rather than starting from a full stochastic description in terms of a master equation), given by  $\dot{c} = f(c(t), p(c(t), t))$  where the vector field,  $f$ , has a stochastic time-dependent modulation given by  $p(c(t), t)$ . We can think of  $p$  as time-dependent parameters of the vector field. They remain constant until events fire and then the vector field changes form; in what follows we show an example of the switching vector field for a two state stochastic variable. The complication is that the transition rates for the process  $p$  will in general depend on the continuous variables  $c(t)$ . We will outline a numerical scheme for solving such a system below.

Then we attempt to derive an approximation to the stochastic dynamics in the limit that the switching rates for the stochastic variables are fast. This is the averaging approximation, which aims to provide a corrected deterministic set of equations to describe the expectation of the trajectory. Our averaging method, however, mainly fails to capture the correction to the dynamics for the parameter

regimes we have examined.

## 4.2 Mixed dynamics simulation

We start with a time-dependent vector field that changes stochastically

$$\frac{dc}{dt} = f(c(t), p(c(t), t)) \quad (4.1)$$

$p(c(t), t)$  is a sample path of a continuous time Markov Chain with discrete state space,  $\{p_1, p_2, \dots\}$ , and has an associated time dependent transition rate matrix,  $\Gamma_{nm}(c(t)) = \text{Prob}(p_n \rightarrow p_m; c(t))$ . Therefore the rate of leaving state  $n$  is  $\Gamma_n(t) = \sum_m \Gamma_{nm}(c(t))$ . Over a suitably small interval  $\Delta t$ , the probability of leaving state  $n$  is approximately  $\Gamma_n(t)\Delta t$ . This means that the probability of still being in state  $n$  in a finite interval of time,  $(t, T)$ , where  $T = t + N\Delta t$  is given by

$$\lim_{\Delta t \rightarrow 0} \prod_{i=1}^N (1 - \Gamma_n(t + i\Delta t)\Delta t) = e^{-\int_t^T \Gamma_n(t') dt'} \quad (4.2)$$

(To see this, take the log of the first expression and Taylor expand to linear order in  $\Delta t$ .) To generate a firing time for the stochastic event, we then need to increase  $T$  until Eqn. 4.2 exceeds a simulated uniform random variable on  $[0, 1]$ . Simultaneously, we integrate forward the equations for the time evolution of  $c(t)$ . The algorithm for mixed dynamics proceeds as follows:

1. At time  $t$ , the stochastic variables are in state  $p_n$ , say. We generate a uniform random number  $R$  in  $[0, 1]$ .
2. We integrate both  $\Gamma_n(t)$  and  $c(t)$  forward in time until  $T$ , when  $e^{-\int_t^T \Gamma_n(t') dt'} = R$ . Then a stochastic event must take place.

3. We choose the new state  $p_m$  with a probability given by

$\Gamma_{nm}(c(T))/(\sum_m \Gamma_{nm}(c(T)))$  as is standard in simulating continuous time Markov Chains.

4. We repeat from step 1, until we have simulated the entire time interval of interest.

In practice, we do not catch the crossing of  $R$  in step 2 using an event trapping technique, but rather use the fact that  $R(T) = e^{-\int_t^T \Gamma_n(t') dt'}$  is monotonic to reparametrize time using  $R$  itself. That is, we append an equation

$$dT/dR = (-e^{-\int_t^T \Gamma_n(t') dt'} \Gamma_n(T))^{-1} = -1/(R\Gamma_n(T))$$

to the system of differential equations and rewrite  $dc/dT$  as  $dc/dR = (dc/dt)/(dR/dT)$ .

Note that this method has features in common with the recently developed *hybrid algorithms* [30, 10] which dynamically partition species into small and large numbers, simulating the evolution of the former with a fully stochastic algorithm, and the latter with a Poisson, Langevin or deterministic approximation algorithm. It is the averaged trajectories that come from a simulation using this algorithm which we wish to approximate using the averaging technique introduced in the next section. In particular, we examine a system where the transition rates for the process  $p$  are large compared to the time scale of the slow (deterministic) variables in the system.

### 4.3 Auto-inhibitory gene dynamics

To illustrate the method, we consider a simple genetic network of one gene that is repressing for its own transcription, see Fig. 4.1. The operator site  $P$  is a

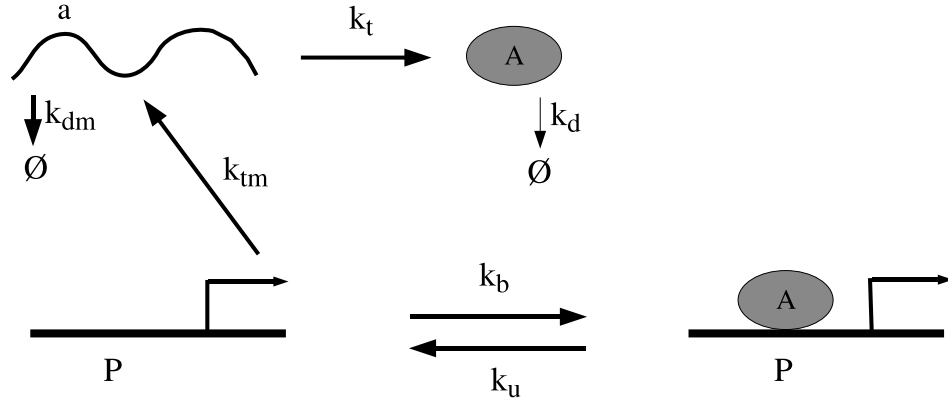


Figure 4.1: Auto-inhibitory one gene network. When the operator site  $P$  is cleared mRNA transcripts can be made at a rate  $k_t$  and translation occurs at a rate  $k_{tr}$  to make protein  $A$ . However  $A$  binds to its own operator site and represses transcription. The mRNA is degraded at rate  $k_d m$  and the protein is degraded at rate  $k_d$ .

random variable that can only be  $\{0, 1\}$  and so breaks the assumption of large molecule number that would warrant a deterministic description. Nevertheless, the deterministic equations for the system are

$$\frac{dP}{dt} = -k_b P A + k_u P : A \quad (4.3)$$

$$\frac{dP : A}{dt} = k_b P A - k_u P : A \quad (4.4)$$

$$\frac{da}{dt} = k_{tm} P - k_{dm} a \quad (4.5)$$

$$\frac{dA}{dt} = k_t a - k_d A - k_b P A + k_u P : A \quad (4.6)$$

$$(4.7)$$

Now we replace the first two equations by a stochastic process (telegraph noise) that represents the flipping between the  $P = 0$  (operator occupied, transcriptionally inactive) and  $P = 1$  (operator unoccupied, transcriptionally active) states,

with rates given by  $\Gamma_{10} = k_b A$  and  $\Gamma_{01} = k_u$ . (We get this from looking at the RHS of Eqn. 4.3 with  $P = 1, P : A = 0$  and  $P = 0, P : A = 1$ .) The remaining two equations is the vector field for  $a$  and  $A$  which randomly changes as  $P$  changes ( $P : A = 1 - P$ ). As we would like to uncouple fast/slow components of the trajectory, it is convenient to define a new variable  $B = P : A + A$ , i.e. total protein level, which remains constant during the fast binding/unbinding reactions on the operator site. It also is useful to set the RNA and protein degradation rates equal,  $k_{dm} = k_d$ , and rescale time by the degradation rate ( $t \rightarrow k_d t$ ). Then define the constants  $\alpha = k_{tm}/k_{dm}$ ,  $\beta = k_t/k_d$ , to yield the equations we simulated using the mixed dynamics algorithm:

$$\frac{da}{dt} = \alpha P(B(t), t) - a \quad (4.8)$$

$$\frac{dB}{dt} = \beta a - B + 1 - P(B(t), t) \quad (4.9)$$

An example of a sample path generated by the mixed dynamics algorithm is shown in Fig. 4.2. Shown in Fig. 4.3 are the phase portraits and isoclines for the  $P = 0$  and the  $P = 1$  vector fields.

Note that although the level of total protein,  $B$ , is not directly affected by the binding/unbinding events, and therefore does not change on the time scale of  $P$  (as  $A$  does), it is affected by the *integral* of the process  $P$ . In the asymptotic limit that the binding/unbinding rate of the repressor protein to the repressor site is infinitely fast compared to the dynamics of  $a$  and  $B$  we can make the zero order approximation and assume that the noise process assumes its average value with respect to the slow variables. We denote the average by  $\langle P(B(t), t) \rangle$  and can identify it with an ensemble average or expectation over the distribution of bound and unbound states:  $\langle P(B(t), t) \rangle = 1 \cdot k_u / (k_b B + k_u) + 0 \cdot k_b B / (k_b B + k_u) = k_u / (k_b B + k_u)$  (The probability of  $P = 1$  (in equilibrium) is  $k_u / (k_b B + k_u)$  and

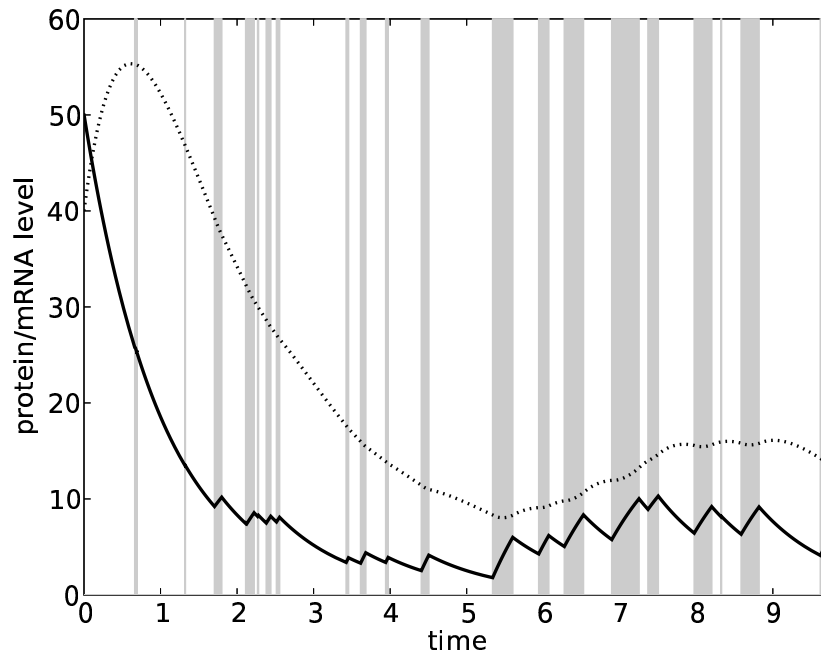


Figure 4.2: The stochastic trajectories for the mRNA level (solid line) and protein level (dotted line). The telegraph noise,  $P$ , alternates between 1 (gray filled) and 0 (white). Parameters are  $\alpha = 20.0$ ,  $\beta = 2.0$ ,  $k_b = .5$  and  $k_u = 2.5$  (the  $k_b$ ,  $k_u$ , values do not correspond to the fast noise regime, but are chosen to show the stochastic transitions).

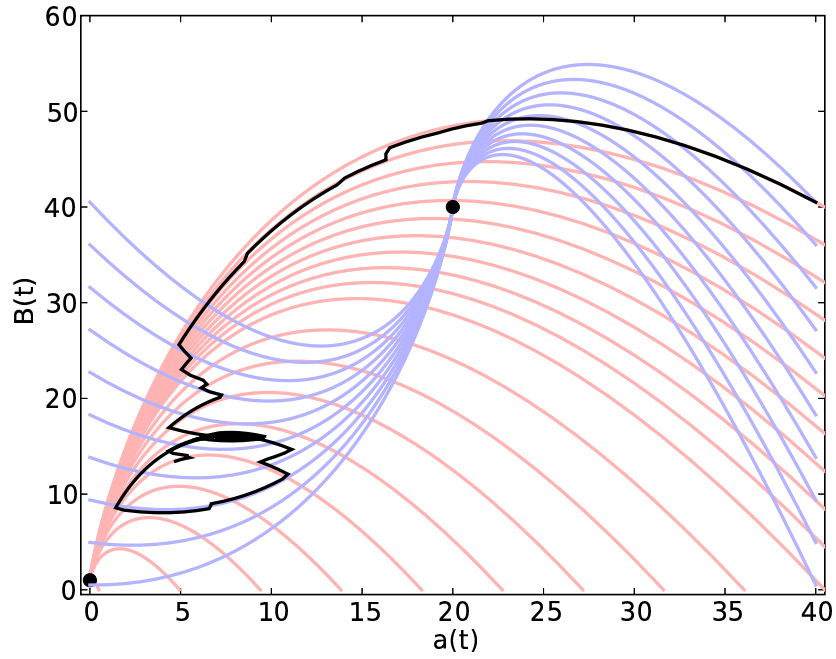


Figure 4.3: Phase portraits for the  $P = 0$  system (pink curves) and the  $P = 1$  system (light blue curves) for the same parameters as in Fig. 4.2. Stable fixed point for each system shown by the black dot. A sample trajectory including the stochastic transitions is shown by the black curve—alternating along trajectories of both vector fields.

$k_b B / (k_b B + k_u)$  is the probability of  $P = 0$ . Note that  $\Gamma_{10} = k_b A = k_b(B - P : A) = k_b B$  because  $P : A$  must be zero for binding to occur.) This expression for the average effect of the fast binding/unbinding is then used in Eqn. 4.9 to give the zero order modified deterministic equations. Note that a major benefit of the equilibrium approximation is that the numerical solution of the equations is now greatly expedited, compared to the mixed dynamics simulation method.

The next order approximation incorporates the (small) effect of the change in the trajectory of  $B$ , when the state  $P$  is zero or one, on the transition rate  $\Gamma_{10} = k_b B$ . The picture is that even though the switching from  $P = 1$  to  $P = 0$  is fast, the effect on  $B$ 's trajectory will in turn feed back into the switching rate. Formally, we will write the variables in the system as a decomposition of a slow large term and a fast small term.  $B(t) = B_0(t) + \zeta(t)$  and  $a(t) = a_0(t) + \eta(t)$ , where  $\zeta$  and  $\eta$  are the fast small perturbations. Then from Eqns. 4.9,

$$\frac{da_0}{dt} + \frac{d\eta}{dt} = \alpha P(B_0 + \zeta, t) - a_0 - \eta \quad (4.10)$$

$$\frac{dB_0}{dt} + \frac{d\zeta}{dt} = \beta a_0 + \beta \eta - B_0 - \zeta + 1 - P(B_0 + \zeta, t) \quad (4.11)$$

We now assume there is a separation of time scales that allows us to consider a short term average noise level  $\langle P \rangle(B_0(t)) = k_u / (k_b B_0(t) + k_u)$  which is on a time scale long enough such that many binding/unbinding events have occurred but short compared to the evolution of  $B_0(t)$ . Then we can decompose  $P(B_0(t), t) = \langle P \rangle(B_0(t)) + \tilde{P}(B_0(t))$ , so  $\tilde{P}$  is two state noise (states  $1 - \langle P \rangle$  and  $-\langle P \rangle$ ) with the same rates as  $P$  but with mean zero. Thus, by equating the fast terms on the LHS and RHS of Eqn. 4.10 and Eqn. 4.11, we get,

$$\frac{d\zeta}{dt} \approx -\tilde{P}(B_0, t) \text{ and } \zeta(t) = - \int_{-\infty}^t \tilde{P}(B_0, t') dt' \quad (4.12)$$

and

$$\frac{d\eta}{dt} \approx \alpha \tilde{P}(B_0, t) \text{ and } \eta(t) = \alpha \int_{-\infty}^t \tilde{P}(B_0, t') dt'. \quad (4.13)$$

Using  $\tilde{P}$  here ensures that both  $\zeta$  and  $\eta$  have mean zero. (Their variance increases linearly in  $t$  however.) We have not included the fast decay terms for  $\eta$  and  $\zeta$  from Eqns. 4.10 and 4.11 as the corresponding decay rate is of order 1. We will see later that the correlation function defining the correction has decay rate  $1/(k_b B_0) + 1/k_u \gg 1$ . Alternatively, one can argue that the fast terms  $\eta$  and  $\zeta$  on the RHS of Eqns. 4.10 and 4.11 are small compared to the  $P$  term and so can be ignored.

Ultimately we are interested in the first order corrected average to  $\langle P(B(t), t) \rangle = \langle P(B_0 + \zeta, t) \rangle$  which incorporates the zero order approximation of  $\zeta$  given above. Therefore we define the functional  $F(B(t), t) = \langle P(B(t), t) \rangle$ . The functional derivative of  $F$  with respect to the path  $B$  is well defined and is given by

$$\frac{\delta F}{\delta B(r)}(B, t) = \lim_{h \rightarrow 0} \frac{1}{h} (F(B(t') + h\delta(t' - r), t) - F(B(t'), t))$$

where the effect on  $F$  due to a vanishing delta function perturbation at  $t' = r$  is being evaluated. Then the change in  $F$  due to a perturbing function  $\zeta(t)$  is given by  $F(B_0(t) + \zeta(t)) = F(B_0(t)) + \langle \zeta(r) | \frac{\delta F}{\delta B(r)}(B_0, t) \rangle$  where the round brackets denote a scalar product (in this case an integral over the appropriate range of  $r$ ). Applying this to Eqn. 4.11 and after averaging (recalling that  $\langle \zeta \rangle = 0$  and  $\langle \eta \rangle = 0$ ) we have

$$\frac{dB_0}{dt} = \beta a_0 - B_0 + 1 - \langle P \rangle - \langle \langle \zeta(r) | \frac{\delta \langle \tilde{P} \rangle}{\delta B(r)}(B_0(t), t) \rangle \rangle$$

where the last term is the next order correction to the dynamics. We define  $\sigma = 1/(k_b B_0)$  and  $\tau = 1/k_u$  as the *mean time* bound or unbound. Then  $\delta \tilde{P} / \delta B =$

$(\delta\tilde{P}/\delta\sigma)(d\sigma/dB) = -1/(k_b B_0^2)(\delta\tilde{P}/\delta\sigma)$ , and we can write

$$\begin{aligned} \langle (\zeta(r) | \frac{\delta\langle\tilde{P}\rangle}{\delta B(r)}(B_0, t)) \rangle &= -\frac{1}{k_b B_0^2} \langle (\zeta(r) | \frac{\delta\langle\tilde{P}\rangle}{\delta\sigma(r)}(\sigma, t)) \rangle \\ &= -\frac{1}{k_b B_0^2} \langle \int_{-\infty}^{\infty} \zeta(r) \frac{\delta\langle\tilde{P}\rangle}{\delta\sigma(r)}(\sigma, t) dr \rangle \\ &= -\frac{1}{k_b B_0^2} \lim_{h \rightarrow 0} \frac{1}{h} \int_{-\infty}^t \langle \zeta(r) (\tilde{P}(\sigma(t') + h\delta(t' - r), t) - \tilde{P}(\sigma(t'), t)) \rangle dr \end{aligned}$$

where we have used the fact that contributions to the functional at a time  $t$  can only come from a time  $r < t$  and the angled brackets is a linear operator. The picture we associate with the *difference path*,  $(\tilde{P}(\sigma(t') + h\delta(t' - r), t) - \tilde{P}(\sigma(t'), t))$  is shown in Fig. 4.4. The difference path is the shaded region that occurs when the perturbed path (with longer waiting time in the up state) splits from the unperturbed path. It is the correlation of this difference path with the unperturbed path that we will want to compute.

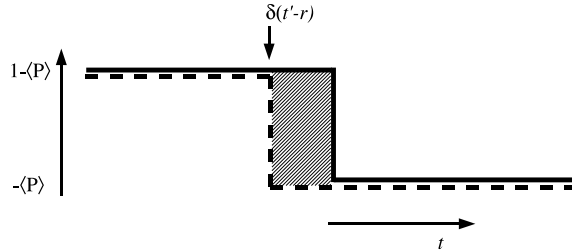


Figure 4.4: The sample paths for the perturbed telegraph noise (solid line) and the unperturbed telegraph noise (dotted line). The perturbation occurs at a time  $r$  in the past and we evaluate its effect at time  $t$ . The difference path is how we interpret the functional derivative of the telegraph signal with respect to its transition rate to the lower state. (The upper state has value  $1 - \langle P \rangle$  and the lower state has value  $-\langle P \rangle$  for  $\tilde{P}$ .)

Next we change variables  $u = t - r$  and flip the integral to get

$$\begin{aligned}
& -\frac{1}{k_b B_0^2} \lim_{h \rightarrow 0} \frac{1}{h} \int_0^\infty \langle \zeta(t-u)(\tilde{P}(\sigma(t') + h\delta(t' + u - t), t) - \tilde{P}(\sigma(t'), t)) \rangle du \\
&= -\frac{1}{k_b B_0^2} \lim_{h \rightarrow 0} \frac{1}{h} \int_0^\infty \langle \zeta(t)(\tilde{P}(\sigma(t') + h\delta(t' - t), t+u) - \tilde{P}(\sigma(t'), t+u)) \rangle du \\
&= \frac{1}{k_b B_0^2} \lim_{h \rightarrow 0} \frac{1}{h} \\
&\quad \int_0^\infty \langle (\int_{-\infty}^t \tilde{P}(\sigma, t'') dt'') (\tilde{P}(\sigma(t') + h\delta(t' - t), t+u) - \tilde{P}(\sigma(t'), t+u)) \rangle du
\end{aligned}$$

since  $\langle \dots \rangle$  is invariant under time translation  $t \mapsto t+u$  and we have substituted for  $\zeta(t)$ , from Eqn. 4.12. Another change of variables  $s = t - t''$  and bringing the integrals outside the angled brackets gives finally:

$$\begin{aligned}
& \frac{1}{k_b B_0^2} \lim_{h \rightarrow 0} \frac{1}{h} \\
& \int_0^\infty \int_0^\infty \langle \tilde{P}(\sigma, t-s)(\tilde{P}(\sigma(t') + h\delta(t' - t), t+u) - \tilde{P}(\sigma(t'), t+u)) \rangle duds \\
&= \frac{1}{k_b B_0^2} \lim_{h \rightarrow 0} \frac{1}{h} \\
& \int_0^\infty \int_0^\infty \langle \tilde{P}(\sigma, t)(\tilde{P}(\sigma(t') + h\delta(t' - t - s), t+u+s) - \tilde{P}(\sigma(t'), t+u+s)) \rangle duds \\
& \quad \text{letting } t \mapsto t+s
\end{aligned}$$

Focusing attention on the integrand we define a correlation function

$$A(u, s) = \langle \tilde{P}(\sigma, t)(\tilde{P}(\sigma(t') + h\delta(t' - t - s), t+u+s) - \tilde{P}(\sigma(t'), t+u+s)) \rangle$$

which represents the correlation of the process  $P$  at a time point  $t$  with the difference path at  $t+u+s$  given that the signal produced an effect at  $t' = t+s$  (when  $u = 0$ ). The way to approach computing the correlation function is to fix  $s$  and then look at how the function evolves in the  $u$  direction by deriving a differential equation for  $u$ . The initial condition to the differential equation will be the function  $A(u = 0, s)$ . For shorthand let  $\{10\}$  represent a state of the difference

path where the perturbed path is up ( $\tilde{P} = 1 - \langle P \rangle$ ) and the unperturbed path is down ( $\tilde{P} = -\langle P \rangle$ ). Only this state will contribute to the correlation  $A(u, s)$ . ( $\{01\}$  cannot occur as the path with a longer waiting time in the up state cannot make a transition to the down state without the unperturbed path doing the same.) Write  $A(u, s)$  in terms of conditional probabilities as follows

$$\begin{aligned} A(u, s) &= \mathbb{P}[\{10\} \text{ at } t+u+s \mid 1 \text{ at } t] (1 - \langle P \rangle) \left( \frac{\sigma}{\sigma + \tau} \right) \\ &\quad + \mathbb{P}[\{10\} \text{ at } t+u+s \mid 0 \text{ at } t] (-\langle P \rangle) \left( \frac{\tau}{\sigma + \tau} \right) \\ &= p_{1,\{10\}}(u, s) (1 - \langle P \rangle) \left( \frac{\sigma}{\sigma + \tau} \right) - p_{0,\{10\}}(u, s) (1 - \langle P \rangle) \left( \frac{\sigma}{\sigma + \tau} \right) \end{aligned}$$

Here, we have used here the fact that the difference path states  $\{11\}$  and  $\{00\}$  do not contribute anything to the correlation,  $\tau/(\sigma + \tau) = 1 - \langle P \rangle$ , and we use  $p_{1,\{10\}}$ ,  $p_{0,\{10\}}$  as a short hand for conditional probabilities. As outlined above we derive an equation for  $p_{1,\{10\}}(u; s)$  and  $p_{0,\{10\}}(u; s)$ , for fixed  $s$ , by noting

$$\begin{aligned} p_{1,\{10\}}(u + du; s) &= p_{1,\{00\}}(u; s).0 + p_{1,\{10\}}(u; s). \left( 1 - \frac{du}{\sigma} - \frac{du}{\tau} \right) + \\ &\quad p_{1,\{11\}}(u; s).0 + p_{1,\{01\}}(u; s).0 \end{aligned}$$

where, for example,  $(1 - \frac{du}{\sigma} - \frac{du}{\tau})$  is the probability of staying in the state  $\{10\}$  during the interval  $(u, u + du)$ , given that the state at time  $u$  is  $\{10\}$ . Therefore,

$$\dot{p}_{1,\{10\}} = -\left( \frac{1}{\sigma} + \frac{1}{\tau} \right) p_{1,\{10\}}$$

Similarly

$$\dot{p}_{0,\{10\}} = -\left( \frac{1}{\sigma} + \frac{1}{\tau} \right) p_{0,\{10\}}$$

giving

$$p_{1,\{10\}}(u, s) = p_{1,\{10\}}(0, s) \exp\left(-\left(\frac{1}{\sigma} + \frac{1}{\tau}\right)u\right)$$

and similarly for  $p_{0,\{10\}}$ . Now note that

$$\begin{aligned}
p_{1,\{10\}}(0, s) &= \mathbb{P}[\tilde{P}(\sigma(t') + h\delta(t' - t - s), t + s) = 1 - \langle P \rangle, \tilde{P}(\sigma(t'), t + s) = -\langle P \rangle \\
&\quad | \tilde{P}(\sigma, t) = 1 - \langle P \rangle] \\
&= \frac{h}{\sigma^2} p_{11}(s) \\
&= \frac{h}{\sigma^2} \frac{1}{\sigma + \tau} \left( \tau \exp(-(\frac{1}{\sigma} + \frac{1}{\tau})s) + \sigma \right)
\end{aligned}$$

where  $p_{11}(s) = \mathbb{P}[\tilde{P}(\sigma, t + s) = 1 - \langle P \rangle | \tilde{P}(\sigma, t) = 1 - \langle P \rangle]$  is the probability of an even number of flips in time  $s$  given that the noise starts in the up state. ( $p_{11}(s)$  can be found by solving Kolmogorov's equations for the two state system.)  $h/\sigma^2$  is the probability of a split between the perturbed and unperturbed paths, given that they are in the up state. Given a delta function perturbation on one of the paths, the probability of a split over a time interval  $\Delta t$  is  $\Delta t/\sigma - \Delta t/(\sigma + h/(\Delta t))$  where the delta function is has height  $h/(\Delta t)$ . Taking  $h \ll \Delta t$  and dropping terms of order  $h^2$  we get  $h/\sigma^2$ . A similar derivation gives

$$\begin{aligned}
p_{0,\{10\}}(0, s) &= \mathbb{P}[\tilde{P}(\sigma(t') + h\delta(t' - t - s), t + s) = 1 - \langle P \rangle, \tilde{P}(\sigma(t'), t + s) = -\langle P \rangle \\
&\quad | \tilde{P}(\sigma, t) = 1 - \langle P \rangle] \\
&= \frac{h}{\sigma^2} p_{01}(s) \\
&= \frac{h}{\sigma^2} \frac{\sigma}{\sigma + \tau} (1 - \exp(-(\frac{1}{\sigma} + \frac{1}{\tau})s))
\end{aligned}$$

Inserting these conditional probabilities into the formula for  $A(u, s)$  we arrive at

$$A(u, s) = \frac{h\tau}{\sigma(\sigma + \tau)^2} \exp(-(\frac{1}{\sigma} + \frac{1}{\tau})u) \exp(-(\frac{1}{\sigma} + \frac{1}{\tau})s)$$

After integration of this correlation function over  $u$  and  $s$ , we get a correction given by

$$\frac{1}{k_b B_0^2} \frac{\sigma \tau^3}{(\sigma + \tau)^4} = \frac{1}{k_b} \frac{B_0}{(B_0 + 1)^4} \text{ when } k_b = k_u \quad (4.14)$$

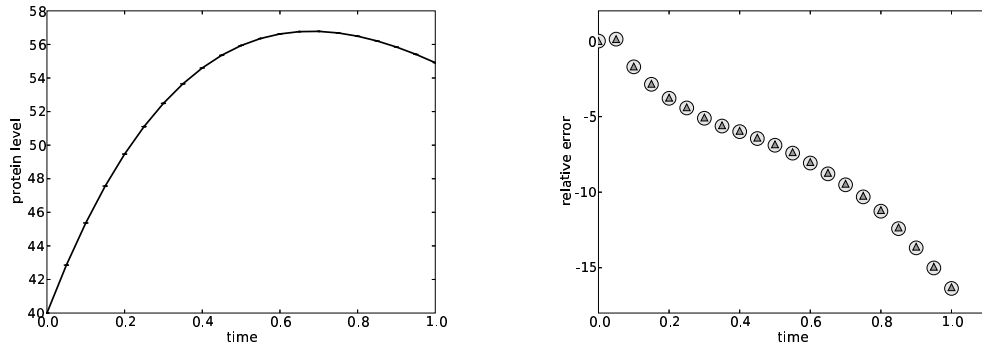
Therefore the new averaged deterministic equations have the asymptotic form for  $\langle P \rangle = \sigma / (\sigma + \tau)$  in addition to the correction of Eqn. 4.14.

## 4.4 Conclusion

Using this correction term does not appear to give significantly better agreement to the mean trajectory of the numerical solution, compared to using the asymptotic equations alone, for the parameter regimes we are interested in. We have found slightly closer agreement for the correction to the fixed point of the system but we feel that either there is another correction of larger size being neglected or there are subtle errors in the numerical implementation.

Shown in Fig. 4.5 is the mean trajectory for the protein level and the relative differences to the corrected trajectories, where the correction is either given by  $\langle P \rangle$  only or  $\langle P \rangle$  and Eqn. 4.14. As can be seen the correction in this regime (where the average time in the up state is approximately .01 and the average time in the down state is .02) is very small compared to the deviation of both the asymptotic and first order corrected solutions from the mean trajectory. This suggests that there is a much larger correction from the asymptotic formulas that has not been taken into account. One observation from Fig. 4.2 is that the noticeable fluctuations in the the protein trajectory appear to be due primarily to the integral of the fluctuations in the mRNA trajectory rather than directly from the stochastic term,  $P$ . If this is indeed the case, then the perturbation we compute using the functional derivative should consider this indirect effect also.

Part of the reason for the very small difference between asymptotic and corrected trajectories in Fig. 4.5 is the presence of the term of order  $1/B_0^3$  in Eqn. 4.14.

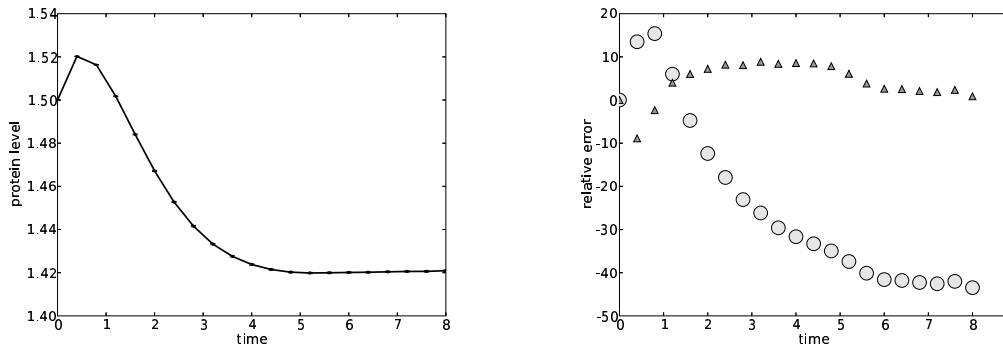


(a) Mean protein trajectory

(b) Relative differences for asymptotic and corrected equations.

Figure 4.5: (a) Mean protein trajectory when  $k_b = 2.5$ ,  $k_u = 50$ ,  $\alpha = 20$ ,  $\beta = 2.0$ . Averaged over 800000 sample paths. Error bars are too small to be seen. (b) Relative differences for the asymptotic and corrected equations. Relative differences are defined as numerical mean trajectory minus theoretical mean trajectory (asymptotic (light circles) or with correction (dark triangles)) divided by the error bars for the numerical mean trajectory.

We can modify the equilibrium such that  $B_0$  tends towards small values, but then we are not in the regime that we set out to describe, i.e. large numbers of slow species, small numbers of fast species. However, if we do this and also set parameters such that the transition rates are an order of magnitude slower than in Fig. 4.5 (to produce a large correction term), we get a mean protein trajectory and relative differences from theory as shown in Fig. 4.6(a) and Fig. 4.6(b). In this regime,



(a) Mean protein trajectory

(b) Relative differences for asymptotic and corrected equations.

Figure 4.6: (a) Mean protein trajectory when  $k_b = 5.0$ ,  $k_u = 5.0$ ,  $\alpha = 20$ ,  $\beta = .1$ . The mean times in the up and down states are approximately .2. Averaged over 850000 sample paths. Error bars are too small to be seen. (b) Relative differences for the asymptotic and corrected equations. Relative differences are defined as numerical mean trajectory minus theoretical mean trajectory (asymptotic (light circles) or with correction (dark triangles)) divided by the error bars for the numerical mean trajectory.

the correction appears to describe the numerical mean better than the asymptotic form for most of the trajectory, and in particular the steady state mean dynamics (from 5 to 8 time units approximately) are quite accurately captured.

Clearly, more numerical tests are needed to determine if the correction we have computed is accurately describing the behavior in the small protein number regime, for different values of  $k_u$ ,  $k_b$ ; if this is the case, the source of the  $1.0/B_0^3$  scaling in Eqn. 4.14 needs to be examined more carefully.

# Appendix A

## A.1 Supplementary information for Chapter 2

### A.1.1 Experimental data

The experimental data are drawn from literature sources [31, 13, 73] and collected in the lab of the co-authors (D.B., Q.F. and R.A.C.) [22]. All measurements were performed using Western blots assays on NIH-3T3 cells and were quantified using densitometry. Within the simulation all species were represented in numbers of molecules per cell. As many of the reactions are restricted to the cell membrane, the numbers quoted can be thought of as effective amounts associated with the membrane. As we are only interested in relative amounts and relative changes of protein level or activity, the absolute numbers used are of less importance and should not be interpreted literally. Approximate receptor numbers were either reported with the source of the experiment or were left as free parameters in the model. EGF molecule number per cell was estimated assuming one million cells per dish and an aliquot of EGF solution of volume 3nL.

All experimental conditions involved serum starvation followed by EGF stimulation of various levels. The Western blots were quantified by measuring average

pixel density in each lane. Error bars (when not available through replicates) were assigned typically as 20% of nominal value.

The full set of numbered experiments, corresponding to fits shown in Fig. A.1, are as follows :

1. Percentage of receptors remaining on cell surface (bound or free of ligand) as a function of incubation time with 100nM EGF. 100,000 receptors (transfected) reported initially [31].
2. Percentage of receptors remaining on cell surface as a function of incubation time with 100ng/ml EGF. 100,000 receptors (transfected) reported initially [13].
3. Percentage of receptors remaining on cell surface as a function of incubation time with 100ng/ml EGF. 275,000 receptors (transfected) reported initially [13].
4. Percentage of surface, internal and degraded EGF after pre-loading the receptors with EGF in conditions that prevent internalization and then allowing internalization at time zero. There is no EGF exposure apart from preloaded amounts. 100,000 receptors (transfected) reported initially [31].
5. Total level of EGFR as a function of incubation time with 100ng/ml EGF. 3 experimental conditions: endogenous levels of Cdc42, transfection of the Cdc42F28L fast cycler, transfection of the Cdc42( $\Delta$ L8/F28L) fast cycler which is Cool-1 binding defective. 8000 receptors (endogenous) reported initially [73].
6. Phosphorylation of Cool-1 (endogenous levels) after incubation with 100ng/ml

EGF for the given times. Number of EGFR receptors (transfected) is a free parameter [22].

7. Phosphorylation of Cool-1 (transfected) after incubation with 100ng/ml EGF for the given times. Number of Cool-1 molecules taken as 10 fold over normal. Number of EGFR receptors (transfected) is a free parameter [22].
8. Phosphorylation of Erk after incubation with 100ng/ml EGF for the given times. 2 experimental conditions: endogenous levels of Cdc42 or an siRNA knockdown of Cdc42. The knockdown was estimated to reduce the Cdc42 levels to 18 percent of normal [22]. EGFR was at endogenous levels (assumed to be 8000 receptors as in [73]).
9. Phosphorylation of Erk after incubation with 100ng/ml EGF for the given times. 2 experimental conditions: endogenous levels of Cool-1 or an siRNA knockdown of Cool-1. The knockdown was estimated to reduce the Cool-1 levels to 26 percent [22]. EGFR was at endogenous levels (assumed to be 8000 receptors as in [73]).
10. Phosphorylation of Cool-1 after incubation with 100ng/ml EGF for a range of times. EGFR number (transfected) is a free parameter. This experiment differs from the previous endogenous Cool-1 activation assay in that early time points are measured [22].
11. Activation of Cdc42 (total level of Cdc42 GTP-bound) after incubation with 100ng/ml EGF [22]. EGFR was at endogenous levels (assumed to be 8000 receptors as in [73]).

### A.1.2 Model details

The model as shown in Fig. 2.1 of the main text involves 41 distinct dynamical variables and 53 unknown rate and Michaelis-Menten constants. Additionally, it was found useful to include the total number of Cool, Cbl and Cdc42 molecules as fitted variables. Thus the optimization problem of minimizing the least squares cost function involves 56 free parameters. Optimization was primarily carried out using a Levenberg-Marquardt method [14], working in the natural logarithm of the biochemical constants to enforce the positivity constraint. The fits to the experimental data are shown in Fig. A.1, including the last experiment performed on active Cdc42 which needed no re-optimization.

The system was modeled using SloppyCell, available at <http://sloppycell.sourceforge.net>. SloppyCell is a Python-based modeling environment which facilitates the development, simulation and optimization of biochemical networks. The Systems Biology Markup Language (SBML) format file [36] for the model (interpretable by SloppyCell and many other biochemical network simulators) and best fit parameter sets can be obtained from the first author.

### A.1.3 Parameter sensitivities

A common technique in model exploration is sensitivity analysis — determining which directions in parameter space are dominant in controlling the system behavior (as measured by the fit to the data in this case). Fig. A.2 shows the first three eigenvectors of the FIM which show the directions in parameter space that are most constrained by the experimental data. Note that the most sensitive components of the pathway appear to be related to the action of the phosphatases: a

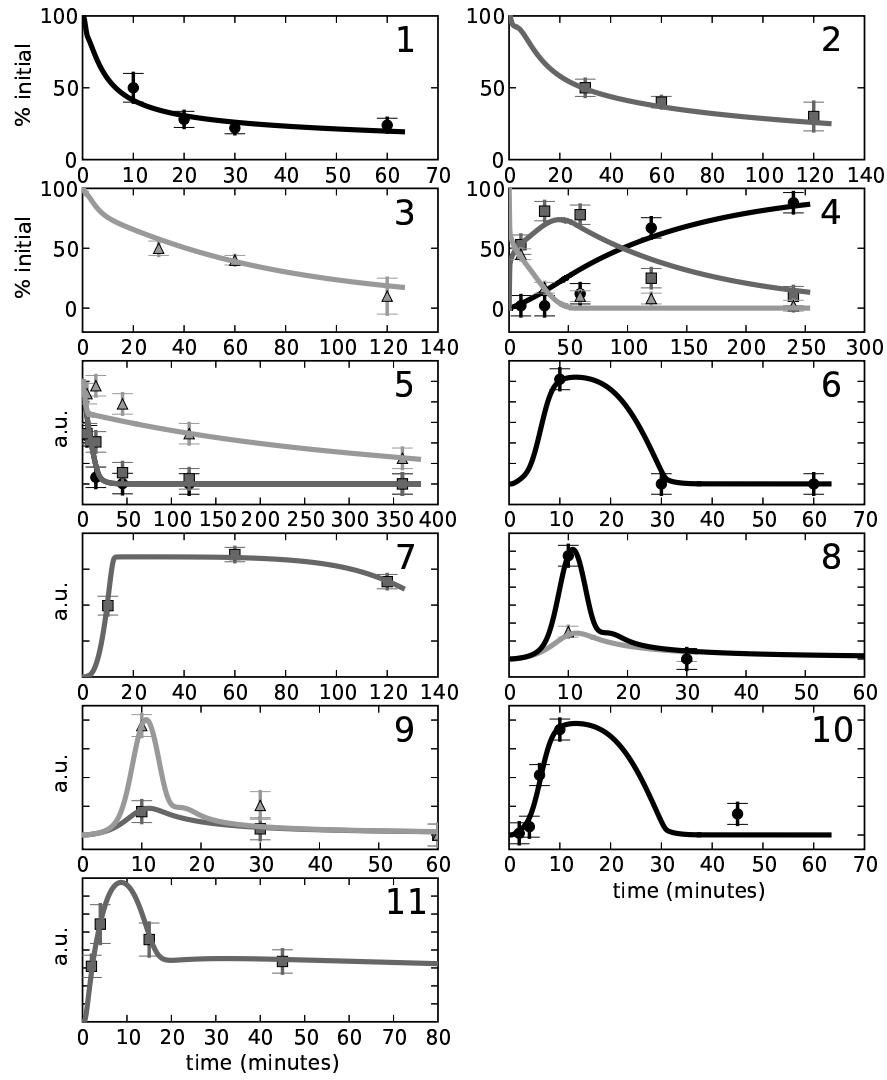


Figure A.1: Experimental data and fits for all the experiments described in the text. Experiment 4: surface EGF (light triangles), internal EGF (gray squares), degraded EGF (dark circles). Experiment 5: Cdc42(F28L) overexpression (light triangles), Cdc42(F28L/DL8) (gray squares), control (black circles). Experiment 8: Cdc42 siRNA (light triangles), control (black circles). Experiment 9: Cool-1 siRNA (gray squares), control (light triangles). All other experiments measure a single species for a single experimental condition described in text.

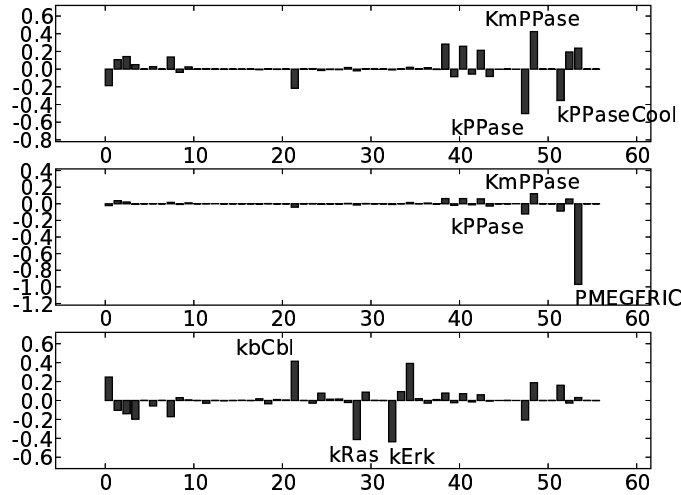


Figure A.2: Components of the first three eigenvectors of the FIM evaluated at the best fit for the EGFR model

generic phosphatase for Cbl, FAK, Erk and the EGFR and a specific phosphatase for Cool-1 (SH-2). Furthermore, the activation pathway of Cool-1 (through FAK and Src) appears to be quite constrained by the experimental data. Whether this is just a function of this particular set of experimental data, or a feature of the model behavior we can test by simulating data on *all* species in the system. Thus we are not biasing the sensitivity analysis towards species that have the most data available. The principal 3 eigenvectors for the system with data simulated for all species at 2 minute timepoints is shown in Fig. A.3. The largest component in the first eigenvector is still the rate constant for the Cool phosphatase and the rate constants of the generic phosphatase are large components in the second eigenvector (the first eigenvector for the simulated data has a dot product of .76 with that for the real data).

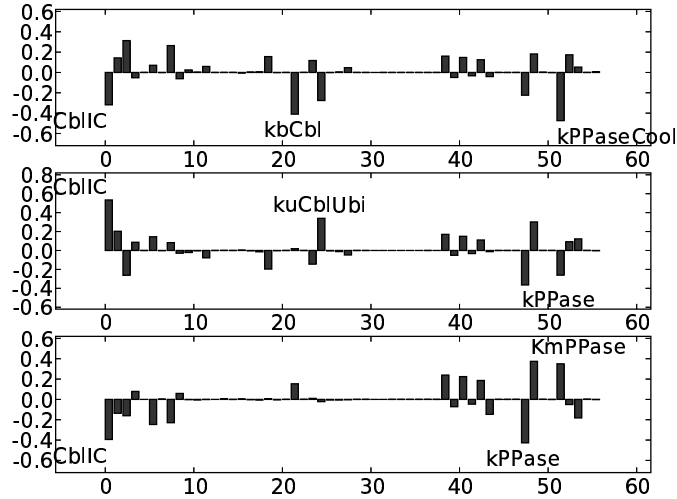


Figure A.3: Components of the first three eigenvectors of the FIM evaluated at the best fit for the EGFR model with simulated data on all species at 2 minute intervals

#### A.1.4 Posterior parameter distribution

Another technique to measure the influence of parameter directions on the behavior of the system is to take a Bayesian approach and directly sample the likelihood function for the data [50, 8]. By applying a Markov Chain Monte Carlo (MCMC) algorithm we can build up a sample of parameter sets from the posterior distribution. We have used the Metropolis Hastings method and run eight MCMC chains for approximately 170 hours on the model with all the experimental data (including the last experiment on total active Cdc42). From the resulting parameter set sample, we removed correlated filtered out correlated members, leaving approximately 5000 parameter sets as a independent draws from the posterior distribution. The posterior sample will be more constrained in some directions than in others. The most tightly constrained directions (as determined by doing a Principal Com-

ponent Analysis (PCA) on the cloud of parameter sets) are directions that most affect the behavior of the model. The 3 PCA axes corresponding to the most constrained directions are shown in Fig. A.4. The last principal component axis has

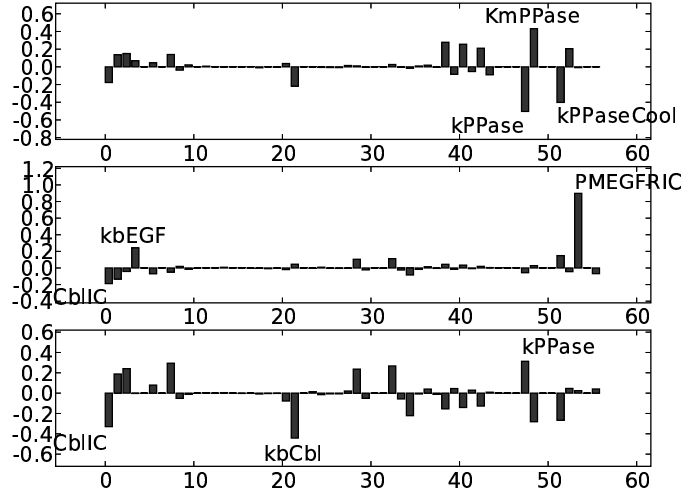


Figure A.4: The last three principal component axes, in reverse order, (most tightly constrained directions) for a sample of approximately 5000 parameter sets sampled from the posterior distribution.

a dot product of .96 with the first eigenvector of the FIM, demonstrating that the linear approximation underlying the FIM is quite accurate, at least in determining the most constrained direction.

The Bayesian approach also provides us with a tool for generating a distribution of predictions from the posterior distribution of parameter sets. As these predictions are derived from a sampling of the full likelihood function (compared to the Gaussian approximation assumed in the Fisher Information Matrix approach) we would expect it to give a more accurate estimate of the true uncertainties. For comparison we show in Fig. A.5 and Fig. A.6 the predictions on total surface

EGFR in v-Src cells and triple complex levels in wild type cells, using the Bayesian error estimates.

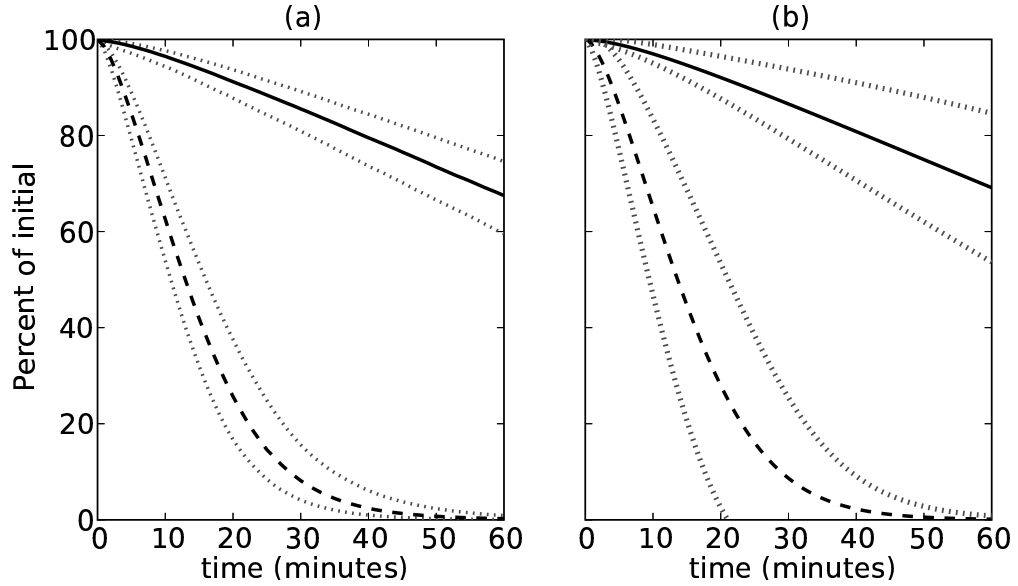


Figure A.5: The total surface receptor numbers after EGF stimulation in stably transfected v-Src cells. The two experimental conditions are endogenous levels of Cool-1 (dashed curve) or overexpressed Cool-1 (solid curve). (a) The total surface receptor trajectory is a median of all the trajectories in the posterior distribution. The uncertainties are the boundaries of the 68% credible regions (dotted lines) to correspond with the one standard deviation errors shown in the main text. (b) The linearized estimates, shown for comparison.

The uncertainties are sufficiently similar between the two approaches that we can justify the methods used in the main text and can confirm the conclusions made there.

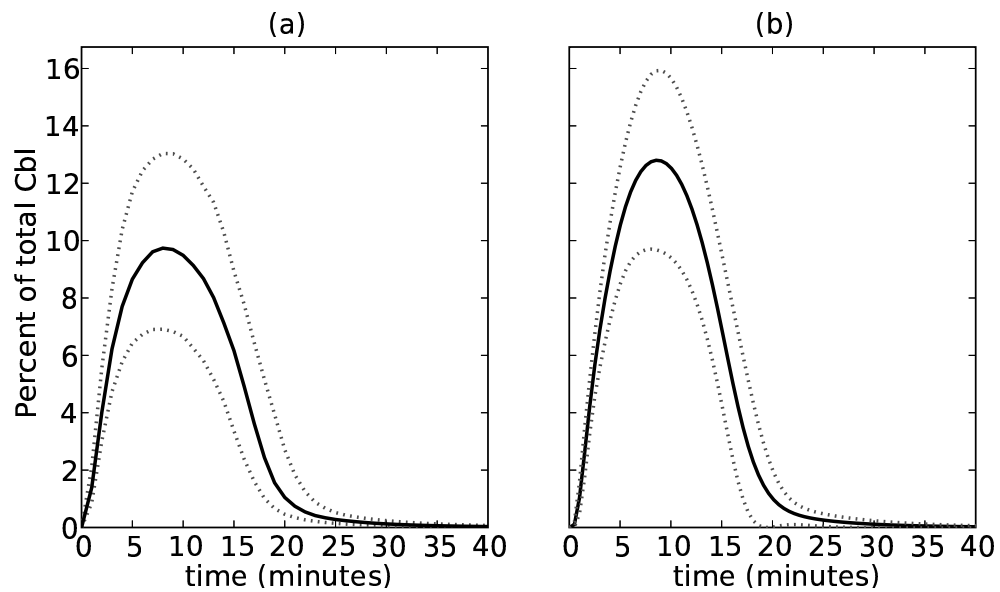


Figure A.6: The level of the triple complex in wild type cells with endogenous EGFR. (a) Median trajectory (solid curve) and the uncertainties given by the boundaries of the 68% credible region (dotted lines). (b) The linearized estimates, shown for comparison. Note that the best fit trajectory in (b) is noticeably different from the median trajectory shown in (a)

### A.1.5 Parameter information and prediction uncertainty

As mentioned in the main text, the addition of the new data had little effect on the parameter uncertainty in the system but significantly reduces the uncertainty in the prediction of the time course for the triple complex. Conversely, assuming precise values for the rate constants involved in the formation and dissociation of the triple complex (binding and unbinding rate constants) does little to change the uncertainty in the prediction. This is shown in Fig. A.7. The reason for the

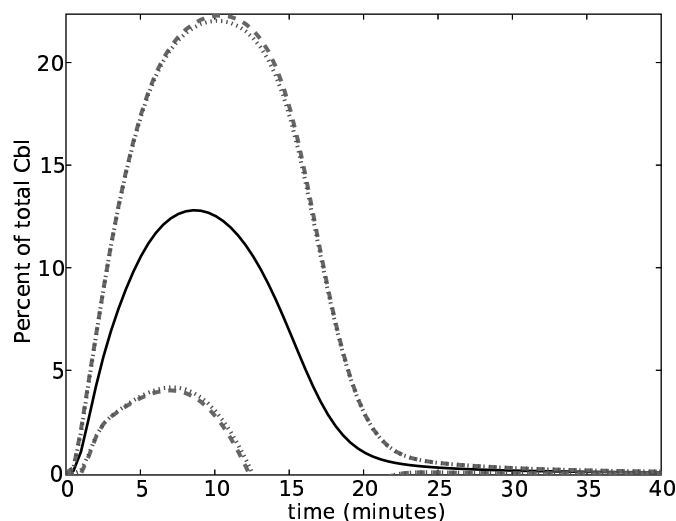


Figure A.7: The uncertainties on the prediction of the triple complex with no formation/dissociation rate constant information (dashed line) and assuming the relevant rate constants are known to within 5% (dotted line).

apparent insignificance of the rate constant information is that the underlying uncertainty in the trajectory of the triple complex derives from the uncertainty in the *components* from which it is comprised, rather than from the uncertainty in the rate constants for formation and dissociation.

# Appendix B

## B.1 Parameter and residual sensitivity matrices

As a diagnostic tool for interpreting how the data and parameters influence each other, we decided to compute various sensitivity matrices relating parameters and data. We considered the following linear response matrices : derivative of residuals of the data with respect to parameters, the derivative of parameters with respect to residuals and the derivative of residuals with respect to residuals. By analyzing these types of matrices, one can determine whether difficulties in obtaining good fits are due to a few data points which are “pulling” parameter values one way while other data points pull in a different direction or whether data points themselves are forcing two contradictory behaviors of the model. Even if a model is fitting satisfactorily, they provide information on which parameters are most influenced by particular data sets. For completeness, we also examine the correlation matrix for parameters, which can be thought of as a parameter response to parameter matrix. We have already come across it in Chapter 2, as it is the (scaled) inverse Fisher Information Matrix (FIM).

The least squares cost function we use is  $C(\theta) = 1/2 \sum_i^m r_i(\theta)^2$  where  $r_i(\theta)$  is the  $i^{th}$  residual with respect to the data. That is,  $r_i(\theta) = (y(t_i, \theta) - d_i)/\sigma_i$

is the discrepancy of the model output,  $y$ , to data point,  $d_i$ , scaled by the data error,  $\sigma_i$ . In what follows, the parameter vector,  $\theta \in \mathbf{R}^n$ , and the residual vector,  $r(\theta) \in \mathbf{R}^m$ . We also write  $y$  to mean the vector  $(y(t_1, \theta) \dots y(t_m, \theta))$ , referred to as the *response vector* and  $\text{diag}(\sigma)$  is the diagonal matrix with elements  $(\sigma_1 \dots \sigma_m)$ . With this notation, the residual vector  $r = \text{diag}(\sigma)^{-1}(y - d)$ . (For notational simplicity, we are treating the model output  $y(t, \theta)$  as a scalar variable but in practice, it has as many components as there are measured species.)

### B.1.1 Residual response with respect to parameters

To describe the residual response with respect to parameters, we can use the  $J$  matrix discussed in the previous section,  $J = \partial r(\theta) / \partial \theta|_{\theta^*}$ , where  $\theta^*$  is the optimized parameter set. This is useful to determine which parameters have the most influence on particular data sets and can also be used to form the approximate inverse covariance matrix  $J^t J$ . Regarding  $J$  as the Jacobian for the residual function  $\theta \rightarrow r(\theta)$ , we can think of  $J^t J$  as providing a local metric on the parameter space through  $\|\Delta p\| = \Delta p^t (J^t J) \Delta p$ .

Examining this matrix can therefore be useful in determining which parameters are controlling the model output with respect to individual data sets. Of course, as it only gives local information, it will be unlikely to help when the current set of parameters is in a flat region far from an optimum where the direction to the minimum is not pronounced.

### B.1.2 Parameter response with respect to residuals

To determine which parameters are most affected by changes in individual residuals (occurring through changes in the data), we can consider what happens to

parameters after a shift in a data point. We assume for simplicity that the model already fits the data and therefore the Hessian of the cost function is positive definite. Consider an infinitesimal change in residuals,  $r(\theta^*) \rightarrow r(\theta^*) + \Delta r$ . The change in the parameters can be determined through the Gauss-Newton step,  $\Delta\theta = -H^{-1}\nabla C = -H^{-1}J^t(r(\theta^*) + \Delta r)$ , such that the new minimum is exactly at  $\theta^* + \Delta\theta$ . However,  $\nabla C(\theta^*) = -H^{-1}(\theta^*)J^t(\theta^*)r(\theta^*) = 0$ , since  $\theta^*$  is the minimizer. Therefore,  $\Delta\theta/\Delta r = \partial\theta/\partial r = -H^{-1}J^t$ , evaluated at  $\theta^*$ . If we also assume that  $r \approx 0$ , i.e. we have a noiseless perfect fit, then  $H \approx J^t J$  and  $\partial\theta/\partial r = -(J^t J)^{-1}J^t$ . Given a singular value decomposition,  $J = U\Sigma V^t$ , where  $\Sigma$  is an  $m$  by  $n$  diagonal matrix, we find (assuming  $m > n$ ) that  $\partial\theta/\partial r = \sum_{i=1}^n (1/\sigma_i)v_i u_i^t$ . This allows us to avoid explicit matrix inversion of  $J^t J$  which is close to singular. (In practice a cutoff will be needed on the singular values  $\sigma_i$  to avoid a “blow-up” of errors in the computation of  $\partial\theta/\partial r$ .) Alternatively, the form for  $\partial\theta/\partial r$  can be recognized as the the negative of the pseudoinverse of the  $J$  matrix, so it naturally describes the linear mapping from residuals to parameters.

### B.1.3 Residual response with respect to residuals

If a residual is disturbed by moving a data point, the system will respond by moving parameters, but that will lead to a change in the residuals as the model output has changed. This is how we define a residual response to residual matrix. Proceeding as shown above, where parameter responses are determined through the effect of a Gauss-Newton step, we note first  $\partial y/\partial r = \partial y/\partial\theta \partial\theta/\partial r$ . We already have an expression for  $\partial\theta/\partial r$  from above, and clearly if  $y$  is the vector of model outputs of the species and at the times of the experiments, then  $\partial y/\partial\theta = \text{diag}(\sigma)J$ . Thus

since  $r = \text{diag}(1/\sigma)(y - d)$  we can write

$$R = \frac{\partial r^*}{\partial r} = I - JH^{-1}J^t \quad (\text{B.1})$$

where  $r^*$  is the residual vector regarded as a function of parameters only and  $r$  is the residual vector regarded as a function of data only. If again we assume that  $r \approx 0$  at the best fit,  $H = J^tJ$  and  $R = I - J(J^tJ)^{-1}J^t$ . Given a singular value decomposition,  $J = U\Sigma V^t$ , where  $\Sigma$  is an  $m$  by  $n$  diagonal matrix, we find  $R = I - \sum_{i=1}^n u_i u_i^t = I - P_J$ . The set  $\{u_i\}$  is an orthogonal basis for  $\text{col}(J)$  (assuming  $m < n$ , i.e. more data points than parameters), and thus  $P_J$  is the orthogonal projector onto  $\text{col}(J)$ .

#### B.1.4 Parameter response with respect to parameters

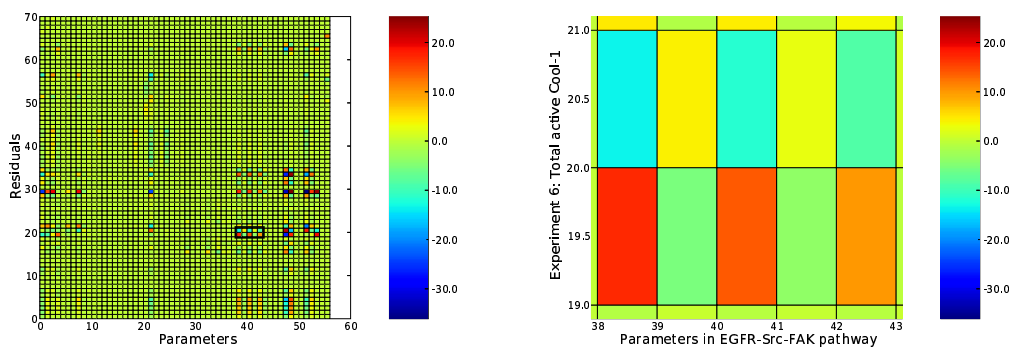
Finally, we may wish to look at interactions between parameters. If one parameter moves, we want to define a matrix which gives the coordinated changes in the other parameters be to maintain the fit. We have already come across this matrix as it is simply the inverse of the Fisher Information Matrix (FIM),  $(J^tJ)^{-1}$ . In Appendix A.1, we examine the eigenvectors of the FIM to determine which are the most constrained directions in parameter space. If we want to identify subsets of connected parameters it is more convenient to examine the *correlation matrix*, which is  $(J^tJ)^{-1}$  with column  $i$  and row  $i$  divided by the square root of the  $i^{\text{th}}$  diagonal element.

We would expect that highly negatively correlated parameters can “compensate” for each other; decreasing one and increasing the other has no effect on the fit. Similarly, highly positively correlated parameters are often binding/unbinding constants, where the product of non-logarithmic parameters is unconstrained whereas

the ratio (corresponding to the equilibrium constant) is constrained. The former situation, where certain parameters have similar effect on the model output, should also be apparent from the similarity of the corresponding columns of the  $J$  matrix.

### B.1.5 Response matrices for the EGFR model

We refer to the EGF receptor model of Chapter. 2 and compute the various sensitivity matrices discussed above. First, we look at the  $J$  matrix or residual to parameter responses in Fig. B.1. Notice that the matrix shows certain patterns or



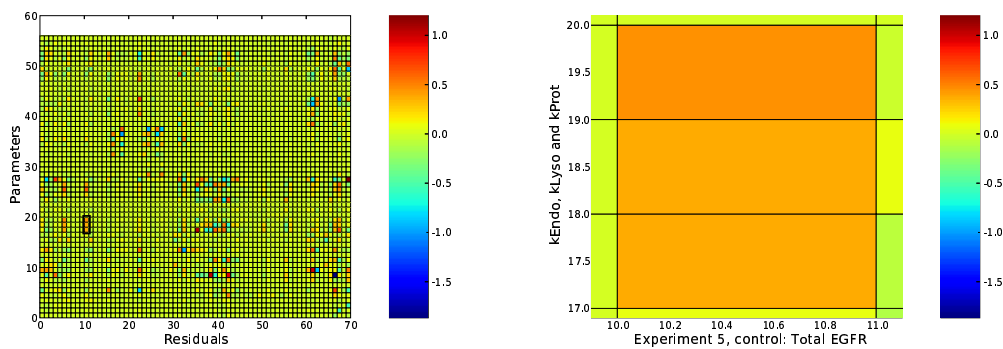
(a) Full 70 residual by 56 parameter sensitivity matrix      (b) Total active Cool-1 residuals, Src-FAK parameters

Figure B.1: (a) The  $J$  matrix, showing residual sensitivities to parameters. (b) Residuals of the total Cool-1 active measurements and dominant parameters

clustering of high/low entries, primarily because the residuals are ordered within experiments and the parameters are ordered approximately in subsets of connected reactions in the network. Notice that the signaling parameters involved in the EGFR to Src to FAK pathway which ultimately leads to Cool-1 activation strongly affect the residuals for that experiment B.1(b). Also, the strong influence of the phosphatases shows up again (they were important components of the eigenvectors

of the FIM, see Chapter 2 supplementary information), but now we can see more specifically that they regulate the active Cool-1 behavior.

Next, in Fig. B.2, we look at the parameter sensitivity to residuals. Again,



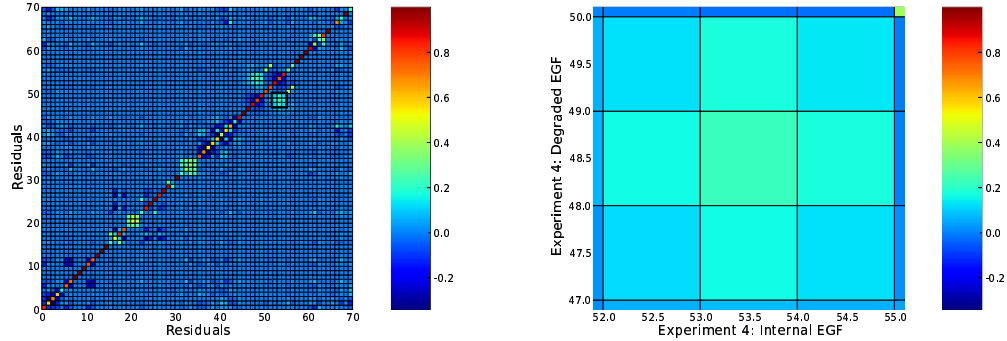
(a) Full 56 parameter by 70 residual sensitivity matrix      (b) Endocytosis, transfer to lysosome and proteolysis rates sensitivities to total EGFR residual at 5 minute time point

Figure B.2: (a) The  $\partial\theta/\partial r$  matrix, showing parameter sensitivities to residuals. (b) Residuals of the total EGFR measurements and dominant parameters

there is some clustering of co-regulated elements in the matrix, due to the ordering of residuals. An example of such a cluster is shown in Fig B.1(b). The experiment (experiment 5) measures total EGFR levels in wild type cells. Unlike the other experiments measuring receptor levels, EGFR is not overexpressed and the time scale for endocytosis and degradation of the receptor is very fast (most of the receptor is gone at the 5 minute time point). By increasing the residual at the earliest 5 minute time point (i.e. *decreasing* the total EGFR datum), we see that all the rate constants involved in the down regulation—endocytosis, transfer to the lysosome and proteolysis rates—have to be increased simultaneously to

accommodate the change.

Next, in Fig. B.3, we consider the residual sensitivities to residuals. Notice



(a) Full 70 residual by 70 residual sensitivity matrix      (b) Sensitivity of residuals for internalized EGF at 3 time points to residuals for degraded EGF

Figure B.3: (a) The  $\partial\theta/\partial r$  matrix, showing parameter sensitivities to residuals.

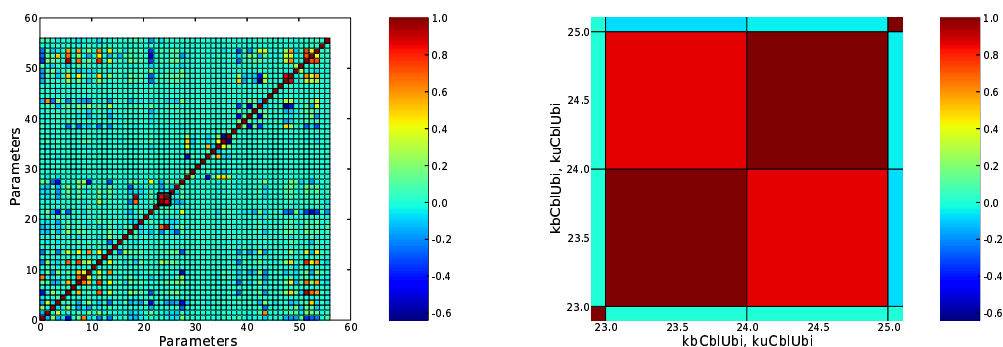
(b) Residuals of the total EGFR measurements and dominant parameters

that most of the large elements are in diagonal blocks; this corresponds to the interactions of residuals within a given experimental time course. That the off-diagonal elements are generally small is a sign that different experiments are not “competing” with each other. The notable exception is shown in Fig B.3(b): here we see that the movements of residuals in one data set strongly affect the residuals in the other data set. A closer inspection reveals that the two time courses are in fact part of the same experiment; an experiment measuring the surface, internal and degraded EGF levels over time (experiment 4 in 2). Because of the conservation of total EGF in all three states we would expect strong dependencies between the data as we see between internal and degraded EGF. There is a similar dependency between surface associated EGF and internal EGF/degraded EGF in

the same experiment.

The main use of this residual with respect to residual response matrix is therefore in determining whether particular data sets are “fighting” with each other; that is, the parameter moves needed to accommodate one data set drastically worsens the fit for another data set.

Finally, we look at the correlation matrix for parameters in Fig. B.4. We see



(a) Full 56 by 56 correlation matrix (b) 2 by 2 block with high positive correlation between binding/unbinding constants

Figure B.4: (a) The correlation matrix. (b) Binding and unbinding constant correlations for Cbl binding to ubiquitinated receptor.

an example in Fig. B.4(b) of a binding/unbinding rate constant pair which are highly positively correlated. Thus, a single multiplicative change to both the non-logarithmic parameters has no significant effect on the fit. In Fig. B.4(a), we also see a cluster of negatively correlated elements in a block on the diagonal (parameters 38 to 43). These elements correspond to the parameters in the EGFR-Src-FAK-Cool activation pathway, which show a positively correlated residual response in Fig. B.1. Taken together, this information suggests that if model reduction is

a priority, then little would be lost by subsuming the Cool activation pathway into just one reaction. Likewise, Fig. B.4(b) suggests that the binding/unbinding reactions involved could be put in equilibrium without significantly worsening the fit to the data.

## B.2 Optimization and data fitting

One of the major obstacles to rapid model development in systems biology is the time taken to optimize models to match with experimental observations. Faced with a lack of fit, the decision to continue searching parameter space with the existing model rather than incorporating new interactions in the network to improve the fit is not clear cut. The existence of many local minima is certainly of concern but the distributions produced by our Markov Chain Monte Carlo sampling methods tend not to be multimodal, suggesting that the cost surface is better described by a single connected region in parameter space that has a wide range of curvatures in different directions — quantified by the typical *sloppy* spectrum of eigenvalues [70]. Combined with the large range of scales, there are also many directions that are nearly degenerate with respect to the cost; certain parameter combinations can change by large amounts without significant change to the data fit. (This also means that looking for a *unique* minimizing parameter set is irrelevant).

Given these difficulties, some care must be taken in applying commonly used local optimization methods. We discuss some of these issues below.

### B.2.1 Large range of scales

The typical scales for the allowed moves in parameter space, while maintaining a good fit, vary enormously from the most constrained parameter direction (stiff) to the least constrained (sloppy). One way to quantify this is through the Fisher Information Matrix (FIM) (introduced in Chapter. 2). Shown in Fig. B.5(a) are the eigenvalues of the FIM for the EGF receptor model (assuming prior information on parameters). There is also a wide range of scales in individual parameter

directions, quantified by the diagonal elements of the FIM, shown in Fig. B.5(b). Together this suggests that optimization algorithms which produce moves that are invariant under scale changes should be preferred on these types of problems. As an example, consider the standard Gauss-Newton step without a trust region:

$$\Delta\theta = -H^{-1}(\theta)\nabla C(\theta)$$

Now, under a linear transformation of coordinates,  $\phi = P\theta$ , and defining  $F(\phi) = C(P\phi)$  we find the Hessian transforms as  $H_\phi = P^tHP$  and the gradient  $\nabla C_\phi = P^t\nabla C$ . Then the optimization move with respect to  $\phi$  coordinates is

$$\Delta\phi = -H_\phi^{-1}\nabla C_\phi = P^{-1}H^{-1}\nabla C$$

i.e.  $\Delta\phi = P^{-1}\Delta\theta$  and the moves with respect to the new or old coordinates are equivalent.

Scale invariance is also a property of the Levenberg-Marquardt (LM) method without a trust region:

$$\Delta\theta = -(J^tJ)^{-1}J^tr \tag{B.2}$$

where  $r$  is the residual vector. Once we introduce a trust region we break the scale invariance,

$$\Delta\theta = -(J^tJ + \lambda I)^{-1}J^tr \tag{B.3}$$

as this becomes  $\Delta\theta = -(1/\lambda)J^tr$  in the limit of  $\lambda \rightarrow \infty$ , which is clearly not scale invariant. There are two options to make the LM method scale invariant. The first is to use the non-trust region method, Eqn. B.2 and cut steps back (almost always necessary as  $J^tJ$  is often close to singular) either by a simple overall scaling or by performing a line minimization in the  $\Delta\theta$  direction. The second is to use a multiplicative Lagrangian trust region parameter:  $\Delta\theta = -(J^tJ + \lambda\text{diag}(J^tJ))^{-1}J^tr$  which is recommended in [53].

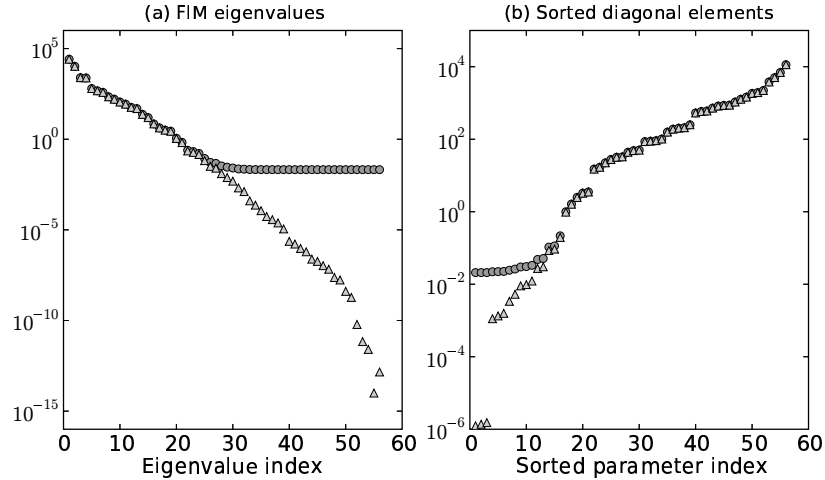


Figure B.5: (a) Eigenvalues for the FIM and (b) Sorted diagonal elements, giving the (approximate) second derivative of the cost with respect to each parameter. The values are plotted assuming a prior distribution on parameters (dark circles), or assuming no prior distribution (light triangles). We impose the same prior distribution on parameters as in Chapter 2, which constrains the fluctuations to within a 1000-fold increase or decrease in the non-logarithmic parameters. The prior is responsible for the “flattening off” of the eigenvalue spectrum and of the sorted diagonal elements. Note that the largest eigenvalues correspond to an allowed fluctuation of less than 1% in the non-logarithmic parameters, the lowest eigenvalues with priors give the 1000-fold fluctuations, but *without priors* the lowest eigenvalues correspond to fluctuations with fold changes of  $\exp(\pm 3^6)$ , which are clearly unphysical.

The standard conjugate gradient (Polak-Ribiere) step can also be made scale invariant by computing inner products with respect to the inverse Fisher Information matrix. Under the standard algorithm, the search direction at the  $k^{\text{th}}$  iterate,  $s_k$ , is given by:

$$s_0 = -\nabla C(\theta_0) \text{ and } s_k = -\nabla C(\theta_k) + \frac{\nabla C_k^t (\nabla C_k - \nabla C_{k-1})}{\nabla C_{k-1}^t \nabla C_{k-1}} s_{k-1}.$$

Under our scale invariant version, we use  $M^{-1} = (J^t J)^{-1}$  as a scalar product and write:

$$s_0 = -M^{-1} \nabla C(\theta_0) \text{ and } s_k = -M^{-1} \nabla C(\theta_k) + \frac{\nabla C_k^t M^{-1} (\nabla C_k - \nabla C_{k-1})}{\nabla C_{k-1}^t M^{-1} \nabla C_{k-1}} s_{k-1}$$

Note that if  $\nabla C$  is computed by finite differencing, then  $J$  can be obtained simultaneously, at almost no extra computational cost.

A comparison of these methods on (artificially) badly scaled problems is shown in Fig. B.6. (The test functions are drawn from [49], and we have selected three that cause the most difficulties when they are modified to have a wide range of parameter scales.) At least on these test problems, the simpler non-trust region LM method with cutoff appears to perform better than the LM method with multiplicative trust region parameter,  $\lambda$ . However, the method does not appear to provide significant improvement in larger biological network problems. The difficulty is that a completely scale invariant method on a sloppy biological problem would use the unmodified FIM or Hessian to compute steps. As we see in Fig. B.5, the smallest eigenvalues are exceptionally small. If we perform just an overall scaling of the step, without disproportionately reducing the size in these sloppy directions (as a trust region algorithm would do), we will have an unwanted situation in which the step size in the stiff directions will be cut back excessively.

The issue of needing finer control over the size of the optimization step is common in complex biological models. Often flat regions in parameter space cor-

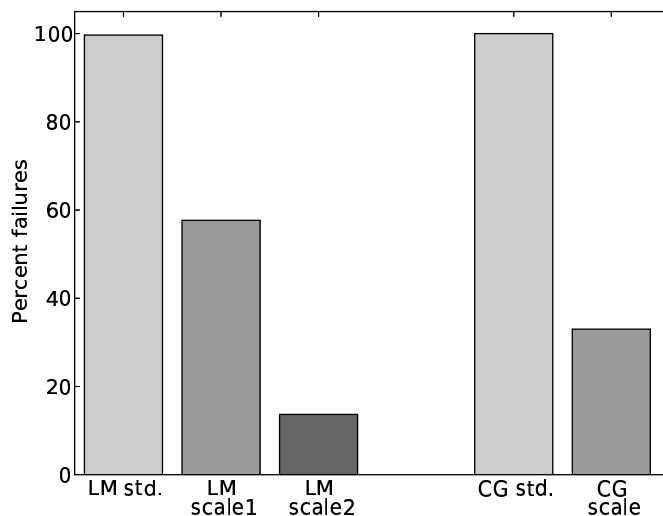


Figure B.6: Bar chart showing the average percentage of failures for 3 badly scaled test functions in the test suite [49] over 100 randomized initial conditions. Each test function is 16 dimensional and failure is defined as a cost greater than 1 after the maximum number of iterations has been exceeded (the minimum possible cost is zero). LM std. and CG std. are the non-scale invariant Levenberg-Marquardt (LM) and conjugate gradient (CG) methods. LM scale1 is the Numerical Recipes scale invariant method [53]. LM scale2 and CG scale are our scale invariant methods discussed in text.

respond to directions which control fast transient reactions in the biochemical network, but for which there is no data. Therefore moving in these directions causes no significant improvement in fit, but significantly slows the integration of the differential equations. Therefore, within our trust region LM algorithm, we set a maximum allowed step size in parameter space and then solve for the appropriate  $\lambda$  to achieve this step size or less. This is easily accomplished by performing the matrix inversion of Eqn. B.3 using a singular value decomposition  $J = U\Sigma V^t$ , where  $U$  is  $m$  by  $m$ ,  $\Sigma$  is  $m$  by  $n$  and  $V$  is  $n$  by  $n$ . Then,

$$\begin{aligned}\Delta\theta &= (J^t J + \lambda I)^{-1} J^t r \\ &= (V\Sigma^t \Sigma V^t + \lambda I)^{-1} V\Sigma^t U^t r \\ &= V(\Sigma^2 + \lambda I)^{-1} \Sigma^t U^t r \\ &= V(\Sigma^2 + \lambda I)^{-1} d\end{aligned}$$

where  $d = \Sigma^t U^t r$  and  $\Sigma^2 = \Sigma^t \Sigma$  is a diagonal  $n$  by  $n$  matrix. Therefore,  $V^t \Delta\theta = (\Sigma^2 + \lambda I)^{-1} d$  and  $\|\Delta\theta\| = \sqrt{\sum_{i=1}^n d_i^2 / (\sigma_i^2 + \lambda)^2} \leq \max_i |d_i| / (\sigma_i^2 + \lambda)$ , and we can directly solve for  $\lambda$  to control the norm of the step.

### B.2.2 Ill-conditioned curvature matrices

Another numerical difficulty for optimization methods on moderate to large size biology models is the high condition number of the curvature matrices, either the Hessian of the cost or  $J^t J$  (of course this is closely related to the problem of a large range of scales). This makes the inversion step needed in Eqn. B.2 more inaccurate. The regularization brought about by applying a trust region, while it prevents a “blow-up” of errors in the computed step, will not change the condition number of  $J^t J$ . One approach we found was useful to more reliably compute the

inverse of  $J^t J$  is to use the SVD algorithm on  $J$  instead of on  $J^t J$  directly. (In a sense,  $J^t J$  has a condition number which is the *square* of  $J$ .) Alternatively, in the Levenberg-Marquardt algorithm, the proposed step can be computed by solving the linear least squares problem  $J\Delta\theta = r$  at every step using a QR factorization, rather than having to work with  $J^t J$ .

### B.2.3 Linearly dependent search directions

Gradient based (eg. conjugate gradient) and pattern search (eg. Powell's method) optimization algorithms generally compute search directions based on previous moves. One pitfall of these methods is that in problems where the local cost surface has a range of curvatures from very small to large is that the search directions can collapse onto subspaces, and in some cases there is close to an exact linear dependence between subsequent search directions. Then the line minimization step along the search directions will land in approximately the same place every iterate, and we will get premature convergence. A quantification of this is shown in the table below, where we have tested the conjugate gradient method on the same three test problems as for Fig. B.6 without the artificial distortion of scales. We show the number of times the last 4 search directions showed an average correlation of more than .999 as a percentage of successful optimizations and as a percentage of failed optimizations. The statistics are collected from 300 runs in total. There is a significant increase in the linear dependency of search directions for the failed runs. (Surprisingly, the linear dependency is also very frequent in successfully completed optimization runs).

Standard CG	Linear dependence
Failures (32.3% of total)	97.9%
Successes (67.7% of total)	80.8%

In an effort to circumvent this, we propose a conjugate gradient method which not only has the desired properties of a conjugate directions method, i.e. converges to the minimum of an  $n$ -dimensional quadratic form in exactly  $n$  steps, but also generates an *orthogonal* set of conjugate directions. Therefore, we expect this method not to have the weakness of the standard conjugate gradient methods. The downside is that the method requires more than one gradient evaluation at every step. The algorithm proceeds as follows:

1. Start at  $\theta_0$ , an initial guess at the optimum.
2. Assume at iterate  $k$  we have computed  $k$  (orthogonal) search directions,  $s_1 \dots s_k$ , which we store rowwise in a matrix  $V_k$ . From these directions we have updated our initial parameter set to  $\theta_k$ . Note:  $k \leq n$  where  $n$  is the number of parameters.
3. Compute the next search direction as an eigendirection of the local Hessian, kept orthogonal to the previous search directions in  $V_k$ . The eigendirection is computed using a power iteration, noting that  $Hv = \nabla C(\theta_k + v) - \nabla C(\theta_k)$  for a pure quadratic cost  $C$ , and for any direction,  $v$ . For a general cost function, we compute the eigendirection by iterating:

$$\epsilon \lambda_{m+1} v_{m+1} = \epsilon H(\theta_k) v_m = \nabla C(\theta_k + \epsilon v_m) - \nabla C(\theta_k) \text{ for } m = 1 \dots S$$

$$v_{m+1} = v_{m+1} - V_k^t V_k v_{m+1}$$

where  $H(\theta_k)$  is the local Hessian, and the number of iterates  $S$  is decided based on accuracy requirements. The second step maintains orthogonality

to the previous search directions during the power iteration stage. The final iterate yields  $v_S$ , which we use as the new search direction. The new search direction is appended to  $V_k$ . If  $k = 0$ ,  $V_0$  is empty, and the first search direction is merely the dominant eigenvector of  $H(\theta_0)$ . Note also that  $\lambda_S$  is an approximation to the second derivative in the search direction.

4. We minimize the cost along the new search direction by choosing a step  $\Delta\theta_k = -(1/\lambda_S)s_k^t \nabla C(\theta_k)$  (i.e. the negative of the derivative of the cost along the search direction divided by the second derivative along that direction).
5. We repeat from step 2 until  $k = n$ . This is one cycle of the algorithm.
6. To perform more cycles we simply empty the matrix of search directions from the last cycle,  $V_n$ , so that the next search direction is again along the dominant eigenvector of  $H(\theta_n)$ .

Note that if the gradient of the cost is available cheaply, from the adjoint method for example, this algorithm becomes more appealing. In step 4, having the second derivative information along the search direction prevents the need to do a line search (as in standard conjugate gradient), but in implementation requires a cutoff step size to be set.

This method is clearly a method of conjugate directions; with a purely quadratic cost function the search directions will exactly be the eigendirections of the quadratic form. However the search directions are also orthogonal. This suggests that the method may do better on problems where the standard CG fails due to linear dependence among the search directions. Numerical tests have shown that this method has a percentage of failures on the test problems of 28%, compared to 32% for standard CG (based on 300 runs), a modest improvement. However, no

attempt has been made to fine tune the algorithm for optimal performance.

### **B.2.4 Fake data**

A heuristic we have found to be useful in the fitting process is the addition of fake data to the existing data sets. The data for the model of Chapter 2 only consists of 3 or 4 time points and generally does not capture the early time dynamics.

Therefore, to guide the fitting process it was often found necessary to add fake data at early times to force the time scale for the transient dynamics to be consistent with the later time measurements. It was also particularly useful in the process of separating the trajectories for active Erk for each of the 2 experimental conditions of experiments 8 and 9 in Chapter 2.

Whether the addition of fake data actually distorts the cost surface sufficiently to reduce barriers between local minima and allows the optimizer to slide from one local minimum to another needs to be investigated. It may also be the case that the fake data just helps to increase the curvature in some directions; before it is added the parameters may be in a relatively flat region of the cost surface and cannot effectively “see” the direction to the minimum.

Of course, once a satisfactory fit is obtained, the fake data is removed. The Markov Chain Monte Carlo methods will then explore the low cost regions around the best fit and so the final distribution of parameter sets are not influenced by the fake data used to find the minimum of the cost basin.

## BIBLIOGRAPHY

- [1] Yves F. Atchade. An adaptive version for the metropolis adjusted langevin algorithm with a truncated drift. Technical report, University of Ottawa, March 2005.
- [2] A. C. Atkinson and A. N. Donev. *Optimum Experimental Design*. Oxford University Press, New York, first edition, 1992.
- [3] Mylene Bedard. Optimal acceptance rates for metropolis algorithms: Moving beyond 0.234. Technical report, University of Toronto, January 2006.
- [4] Ehrhard Behrends. *Introduction to Markov Chains with special emphasis on rapid mixing*. Vieweg, Wiesbaden, first edition, 2000.
- [5] M. L. Blinov, J. R. Faeder, B. Goldstein, and W. S. Hlavacek. A network model of early events in epidermal growth factor receptor signaling that accounts for combinatorial complexity. *BioSystems*, 83:136–151, 2006.
- [6] E. P. J. Boer and E. M. T. Hendrix. Global optimization problems in optimal design experiments in regression models. *Journal of Global Optimization*, 18:385–398, 2000.
- [7] K.S. Brown, C.C. Hill, G.A. Calero, C.R. Myers, K.H. Lee, J.P. Sethna, and R.A. Cerione. The statistical mechanics of complex signaling networks: nerve growth factor signaling. *Phys Biol.*, 1:184–95, 2004.
- [8] K.S. Brown and J.P. Sethna. Statistical mechanics approaches to models with many poorly known parameters. *Phys. Rev. E.*, 68:021904, 2003.
- [9] P. Burke, K. Schooler, and H. S. Wiley. Regulation of epidermal growth factor receptor signaling by endocytosis and intracellular trafficking. *Molecular Biology of the Cell*, 12:1897–1910, 2001.
- [10] Y. Cao, D. Gillespie, and L. Petzold. Multiscale stochastic simulation algorithm with stochastic partial equilibrium assumption for chemically reacting systems. *Journal of Computational Physics*, 206:395–411, 2005.
- [11] Y. Cao, D. T. Gillespie, and L. R. Petzold. The slow-scale stochastic simulation algorithm. *J. Chem. Phys.*, 122:014116, 2005.
- [12] G. Carpenter. The egf receptor : a nexus for trafficking and signaling. *BioEssays*, 22:697–707, 2000.
- [13] R. E. Carter and A. Sorokin. Endocytosis of functional epidermal growth factor receptor-green fluorescent protein chimera. *J. Biol. Chem.*, 273:35000–35007, 1998.

- [14] J.E. Dennis and R.B. Schnabel. *Numerical methods for unconstrained optimization and nonlinear equations*. Prentice Hall, Englewood Cliffs, New Jersey, 1983.
- [15] M. P. DiGiovanna, D. F. Stern, S. M. Edgerton, S. G. Whalen, D. Moore II, and A. D. Thor. Relationship of epidermal growth factor receptor expression to erbB-2 signaling activity and prognosis in breast cancer patients. *Journal of Clinical Oncology*, 23:1152–1160, 2005.
- [16] L. Duan, Y. Miura, M. Dimri, B. Majumder, I. L. Dodge, A. L. Reddi, A. Ghosh, N. Fernandes, P. Zhou, K. Mullane-Robinson, N. Rao, S. Donoghue, R. A. Rogers, D. Bowtell, M. Naramura, H. Gu, V. Band, and H. Band. Cbl-mediated ubiquitinylation is required for lysosomal sorting of epidermal growth factor receptor but is dispensable for endocytosis. *J. Biol. Chem.*, 278:28950–28960, 2003.
- [17] S. Duane, A.D. Kennedy, B.J. Pendleton, and D. Roweth. Hybrid monte carlo. *Physics Letters B*, 195:216–222, 1987.
- [18] D.J. Earl and M. W. Deem. Parallel tempering: Theory, applications, and new perspectives. *Phys. Chem. Chem. Phys.*, 7:3910–3916, 2005.
- [19] Carl Eckart. The theory and calculation of screening constants. *Physical Review*, 36:878–892, 1930.
- [20] S. A. Ettenberg, A. Magnifico, M. Cuello, M. M. Nau, Y. R. Rubinstein, Y. Yarden, A. M. Weissman, and S. Lipkowitz. Cbl-b-dependent coordinated degradation of the epidermal growth factor receptor signaling complex. *J. Biol. Chem.*, 276:27677–27684, 2001.
- [21] D. Faller, U. Klingmuller, and J. Timmer. Optimal experimental design in systems biology. *Simulation*, 79:717, 2003.
- [22] Q. Feng, D. Baird, X. Peng, J. Wang, T. Ly, J-L. Guan, and R. A. Cerione. Cool-1 functions as an essential regulatory node for egf receptor- and src-mediated cell growth. *Nature Cell Biology*, DOI: 10.1038/ncb1453, 2006.
- [23] S.L. Frederiksen, K.W. Jacobsen, K.S. Brown, and J.P. Sethna. Bayesian ensemble approach to error estimation of interatomic potentials. *Phys. Rev. Lett.*, 93:165501, 2004.
- [24] R. Gilks, G.O. Roberts, and S.K. Sahu. Adaptive markov chain monte carlo through regeneration. *Journal of the American Statistical Association*, 93:1045–1054, 1998.
- [25] W.R. Gilks, S. Richardson, and D.J. Spiegelhalter (eds.). *Markov Chain Monte Carlo in Practice*. Chapman and Hall, London, first edition, 1996.

- [26] G.H. Golub and C.F. Van Loan. *Matrix Computations*. The Johns Hopkins University Press, Baltimore, third edition, 1996.
- [27] L. M. Grovdal, E. Stang, A. Sorkin, and I. H. Madshus. Direct interaction of cbl with ptyr 1045 of the egf receptor (egfr) is required to sort the egfr to lysosomes for degradation. *Experimental Cell Research*, 300:388–395, 2004.
- [28] R.N. Gutenkunst, J.J. Waterfall, F.P. Casey, K.S. Brown, C.R. Myers, and J.P. Sethna. Sloppy systems biology: tight predictions without tight parameters, 2006. Submitted.
- [29] H. Hanafusa, S. Torii, T. Yasunaga, K. Matsumoto, and E. Nishida. Shp2, an sh2-containing protein-tyrosine phosphatase, positively regulates receptor tyrosine kinase signaling by dephosphorylating and inactivating the inhibitor sprouty. *J. Biol. Chem.*, 279:22992–22995, 2004.
- [30] L.A. Harris and P. Clancy. A “partitioned leaping” approach for multiscale modeling of chemical reaction dynamics, 2006. Submitted.
- [31] K. Helin and L. Beguinot. Internalization and down-regulation of the human epidermal growth factor receptor are regulated by the carboxyl-terminal tyrosines. *J. Biol. Chem.*, 266:8363–8368, 1991.
- [32] B. S. Hendriks, J. Cook, J. M. Burke, J. M. Beusmans, D. A. Lauffenburger, and D. de Graaf. Computational modelling of erbb family phosphorylation dynamics in response to transforming growth factor alpha and heregulin indicates spatial compartmentation of phosphatase activity. *IEE Proc.-Syst. Biol.*, 1:22–33, 2006.
- [33] F. R. Hirsch, M. Varella-Garcia, P. A. Bunn Jr., M. V. Di Maria, R. Veve, R. M. Bremmes, A. E. Baron, C. Zeng, and W. A. Franklin. Epidermal growth factor receptor in non-small-cell lung carcinomas: correlation between gene copy number and protein expression and impact on prognosis. *J. Clin. Oncol.*, 20:3798–3807, 2003.
- [34] Jie Hu, Ao Ma, and Aaron R. Dinner. Monte carlo simulations of biomolecules: The mc module in charmm. *Journal of Computational Chemistry*, 27:203–216, 2006.
- [35] F. Huang and A. Sorkin. Growth factor receptor binding protein 2-mediated recruitment of the ring domain of cbl to the epidermal growth factor receptor is essential and sufficient to support receptor endocytosis. *Molecular Biology of the Cell*, 16:1268–1281, 2005.
- [36] M. Hucka, A. Finney, H. M. Sauro, H. Bolouri, J. C. Doyle, H. Kitano, A. P. Arkin, B. J. Bornstein, D. Bray, A. Cornish-Bowden, A. A. Cuellar, S. Dronov,

- E. D. Gilles, M. Ginkel, V. Gor, I. I. Goryanin, W. J. Hedley, T. C. Hodgman, J-H. Hofmeyr, P. J. Hunter, N. S. Juty, J. L. Kasberger, A. Kremling, U. Kummer, N. Le Novre, L. M. Loew, D. Lucio, P. Mendes, E. Minch, E. D. Mjolsness, Y. Nakayama, M. R. Nelson, P. F. Nielsen, T. Sakurada, J. C. Schaff, B. E. Shapiro, T. S. Shimizu, H. D. Spence, J. Stelling, K. Takahashi, M. Tomita, J. Wagner, J. Wang, and S. B. M. L. Forum. The systems biology markup language (SBML): a medium for representation and exchange of biochemical network models. *Bioinformatics*, 19(4):524–531, Mar 2003.
- [37] M. Jardat, O. Bernard, P. Turq, and G.R. Kneller. Transport coefficients of electrolyte solutions from smart brownian dynamics simulations. *J. Chem. Phys.*, 110:7993–7999, 1999.
- [38] X. Jiang and A. Sorkin. Epidermal growth factor receptor internalization through clathrin-coated pits requires cbl ring finger and proline-rich domains but not receptor polyubiquitylation. *Traffic*, 4, 2003.
- [39] B. Jones and J. Wang. Constructing optimal designs for fitting pharmacokinetic models. *Statistics and Computing*, 9:209–218, 1999.
- [40] G.L. Jones and J.P. Hobert. Honest exploration of intractable probability distributions via markov chain monte carlo. *Statistical Science*, 16:312–334, 2001.
- [41] B. N. Kholodenko, O. V. Demin, G. Moehren, and J. B. Hoek. Quantification of short term signaling by the epidermal growth factor receptor. *J. Biol. Chem.*, 274:30169–30181, 1999.
- [42] P.V. Kumar, J. S. Raut, and S. J. Warakomski. Smart monte carlo for accurate simulation of rare-event dynamics : Diffusion of adsorbed species on solid surfaces. *J. Chem. Phys.*, 105:686–695, 1996.
- [43] Z. Kutalik, K-H. Cho, and O. Wolkenhauer. Optimal sampling time selection for parameter estimation in dynamic pathway modelling. *BioSystems*, 75:43–55, 2004.
- [44] G. F. Lawler and A. D. Sokal. Bounds on the  $L^2$  spectrum for markov chains and markov processes: A generalization of cheeger’s inequality. *Transactions of the American Mathematical Society*, 309:557–580, 1988.
- [45] G. Levkowitz, H. Waterman, S. A. Ettenberg, M. Katz, A. Y. Tsygankov, I. Alroy, S. Lavi, K. Iwai, Y. Reiss, A. Ciechanover, S. Lipkowitz, and Y. Yarden. Ubiquitin ligase activity and tyrosine phosphorylation underlie suppression of growth factor signaling by c-cbl/sli-1. *Molecular Cell*, 4:1029–1040, 1999.

- [46] H. Maughan and W. L. Nicholson. Stochastic processes influence stationary-phase decisions in bacillus subtilis. *Journal of Bacteriology*, 186:2212–2214, 2004.
- [47] H. H. McAdams and A. Arkin. Stochastic mechanisms in gene expression. *Proc. Natl. Acad. Sci.*, 94:814–819, 1997.
- [48] N. Metropolis, A.W. Rosenbluth, M.N. Rosenbluth, A. H. Teller, and E. Teller. Equations of state calculations by fast computing machines. *J. Chem. Phys.*, 21:1087–1092, 1953.
- [49] J.J More, B.S. Garbow, and K.E. Hillstrom. Testing unconstrained optimization software. *ACM Transactions on Mathematical Software*, 7:17–41, 1981.
- [50] K. Mosegaard and A. Tarantola. Monte carlo sampling of solutions to inverse problems. *Journal of Geophysical Research*, 100:12431–12447, 1995.
- [51] Y. Mosesson, K. Shtiegman, M. Katz, Y. Zwang, G. Vereb, J. Szollosi, and Y. Yarden. Endocytosis of receptor tyrosine kinases is driven by monoubiquitylation, not polyubiquitylation. *J. Biol. Chem.*, 278:21323–21326, 2003.
- [52] F. Pederiva, G.V. Chester, S. Fantoni, and L. Reatto. Variational study of vacancies in solid 4-he with shadow wave fuctions. *Physical Review B*, 56:5909–5917, 1997.
- [53] William H. Press, Saul A. Teukolsky, William T. Vetterling, and Brian P. Flannery. *Numerical Recipes in C*. Cambridge University Press, New York, second edition, 1996.
- [54] C. V. Rao and A. P. Arkin. Stochastic chemical kinetics and the quasi-steady-state assumption: Application to the gillespie algorithm. *J. Chem. Phys.*, 118:4999–5010, 2003.
- [55] H. Resat, J. A. Ewald, D. A. Dixon, and H. S. Wiley. An integrated model of epidermal growth factor receptor trafficking and signal transduction. *Biophys. J.*, 85:730–743, 2003.
- [56] C.P. Robert and G. Casella. *Monte Carlo Statistical Methods*. Springer-Verlag, New York, first edition, 1999.
- [57] G.O. Roberts. Markov chain concepts related to sampling algorithms. In W.R. Gilks, S. Richardson, and D.J. Spiegelhalter, editors, *Markov Chain Monte Carlo in Practice*, pages 45–57. Chapman and Hall, London, first edition, 1996.
- [58] G.O. Roberts and R.L. Tweedie. Geometric convergence and central limit theorems for multidimensional hastings and metropolis algorithms. *Biometrika*, 83:95–110, 1996.

- [59] M. Rodriguez-Fernandez, P. Mendes, and J. R. Banga. A hybrid approach for efficient and robust parameter estimation in biochemical pathways. *BioSystems*, 83:248–265, 2006.
- [60] J.S. Rosenthal. Minorization conditions and convergence rates for markov chain monte carlo. *Journal of the American Statistical Association*, 90:558–566, 1995.
- [61] P. J. Rossky, J.D. Doll, and H.L. Friedman. Brownian dynamics as smart monte carlo simulation. *J. Chem. Phys.*, 69:4628–4633, 1978.
- [62] B. Schoeberl, C. Eichler-Jonsson, E. D. Gilles, and G. Muller. Computational modeling of the dynamics of the map kinase cascade activated by surface and internalized egf receptors. *Nature Biotechnology*, 20:370–375, 2002.
- [63] R. Serban and A. C. Hindmarsh. Cvodes: An ode solver with sensitivity analysis capabilities. LLNL technical report UCRL-MA-148813, Lawrence Livermore National Labs, 2002.
- [64] S. Y. Shvartsman, M. P. Hagan, A. Yacoub, P. Dent, H. S. Wiley, and D. A. Lauffenburger. Autocrine loops with positive feedback enable context-dependent cell signaling. *Am J Physiol Cell Physiol*, 282:C545–C559, 2002.
- [65] S. Y. Shvartsman, H. S. Wiley, W. M. Deen, and D. A. Lauffenburger. Spatial range of autocrine signaling: Modeling and computational analysis. *Biophysical Journal*, 81:1854–1867, 2001.
- [66] S. Sigismund, T. Woelk, C. Puri, E. Maspero, C. Tacchetti, P. Transidico, P. P Di Fiore, and S. Polo. Clathrin-independent endocytosis of ubiquitinated cargos. *PNAS*, 102:2760–2765, 2005.
- [67] S. D. Silvey. *Optimal Design: an introduction to the theory for parameter estimation*. Chapman and Hall, London, first edition, 1980.
- [68] I. Szymkiewicz, K. Kowanetz, P. Soubeyran, A. Dinarina, S. Lipkowitz, and I. Dikic. Cin85 participates in cbl-b-mediated downregulation of receptor tyrosine kinases. *J. Biol. Chem.*, 277:39666–39672, 2002.
- [69] N.G. van Kampen. *Stochastic Processes in Physics and Chemistry*. Elsevier North-Holland, New York, first edition, 1981.
- [70] J.J. Waterfall, F.P. Casey, R.N. Gutenkunst, K.S. Brown, C.R. Myers, P.W. Brouwer, V.Elser, and J.P. Sethna. The sloppy model universality class and the vandermonde matrix, 2006. Submitted.
- [71] A. Wells, J. B. Welsh, C. S. Lazar, H. S. Wiley, G. N. Gill, and M. G. Rosenfeld. Ligand-induced transformation by a non-internalizing epidermal growth factor receptor. *Science*, 247:962–964, 1990.

- [72] E. S. M. Wong, C. W. Fong, J. Lim, P. Y, B. C. Low, W. Y. Langdon, and G. R. Guy. Sprouty2 attenuates epidermal growth factor receptor ubiquitylation and endocytosis, and consequently enhances ras/erk signalling. *The EMBO Journal*, 21:4796–4808, 2002.
- [73] W. J. Wu, S. Tu, and R. A. Cerione. Activated cdc42 sequesters c-cbl and prevents egf receptor degradation. *Cell*, 114:715–725, 2003.